Experimental Studies of Electronic Correlations in Quantum Materials

Nathaniel Robert Davies

Lincoln College

University of Oxford

A thesis submitted for the degree of

Doctor of Philosophy

June 2018

Experimental Studies of Electronic Correlations in Quantum Materials

Nathaniel Robert Davies, Lincoln College, University of Oxford

Trinity Term 2018

Abstract of thesis submitted for the degree of Doctor of Philosophy

In this thesis I present experimental studies of three quantum materials, resolving an important unanswered question about the novel microscopic physics in each case.

I first present inelastic neutron scattering measurements on a powder sample of the unconventional, high-temperature superconductor lithium iron selenide hydroxide, $Li_{1-x}Fe_xODFe_{1-y}Se$ ($x \simeq 0.16, y \simeq 0.02$, $T_c = 41\,K$). The spectrum shows an enhanced intensity below T_c at energy transfers below the superconducting pair breaking energy, with broad maxima at two different wavevectors. The behavior of this feature is consistent with the spin resonance mode found in other unconventional superconductors, and strongly resembles the spin resonance observed in the spectrum of the molecular-intercalated iron selenide, $Li_{0.6}(ND_2)_{0.2}(ND_3)_{0.8}Fe_2Se_2$. The signal can be described with a characteristic two-dimensional wave vector which is consistent with the nesting vector between electron Fermi sheets. These results place a strong constraint on the pairing symmetry in this unconventional superconductor and may have relevance to the high temperature superconductor monolayer FeSe due to structural and electronic similarities between the two systems.

In $Na_2Ti_2Pn_2O$ (Pn = As, Sb), two important members of the titanium oxypnictide family of superconductors, I then present single crystal x-ray diffraction data which reveal a charge superstructure that appears below density wave transitions previously observed in bulk data. From symmetry-constrained structure refinements I am able to completely determine the symmetry and all atomic positions in the distorted phase. I also analyse angle resolved photoemission spectroscopy (ARPES) data, which show band folding and back bending consistent with a density wave with the same symmetry as the lattice distortion as well as evidence for Fermi surface nesting which may help drive the density wave transition. The results provide direct evidence for phonon-assisted charge density wave order in $Na_2Ti_2Pn_2O$. This represents the first complete characterisation of the density wave phase in a titanium oxypnictide, information which is crucial in microscopic modelling of the superconductivity in this family.

Finally I present a detailed study of the pyrochlore osmate $Y_2Os_2O_7$ via a wide variety of experimental techniques. I observe a small, non-zero paramagnetic moment and spin freezing at temperature $T_f \simeq 5\,K$, consistent with previous results, and show based on high-field magnetisation measurements that the paramagnetic moment is very likely to be due to large effective moments located on a small fraction $\sim 2\%$ of Os sites. Comparison of single-ion energy level calculations with resonant inelastic x-ray scattering (RIXS) data yields a non-magnetic $J_{eff} = 0$ ground state on the majority Os^{4+} sites with the spin-orbit interaction, Hund's coupling and trigonal distortion of OsO_6 octahedra all important in modelling the experimentally observed spectra. These results fully explain the unexpected magnetism in $Y_2Os_2O_7$, and the single-ion spectrum may prove useful to inform the search for novel excitonic magnetism in other, related $5d$ materials.

Acknowledgements

Firstly and most importantly, I am hugely grateful to my supervisor Andrew Boothroyd for his guidance and support and for being there for me at all times during my PhD. His ideas and advice are behind every element of the research presented in this thesis and I firmly believe I could not have asked for a better supervisor.

I am also indebted to my many collaborators both within Oxford and at the ISIS, ILL and ESRF facilities where a large proportion of my experiments were performed. In particular, I am very thankful to the other members of the Boothroyd group Marein Rahn, Andrew Princep, Jian Rui Soh and Henrik Jacobsen, who have been through many beamtimes with me and taught me much of what I know.

I am similarly grateful to the many beamline scientists I have worked with including Ivan da Silva, Peter Baker and Helen Walker at ISIS, Cristoph Sahle at ESRF and Lucile Mangin-Thro at ILL, whose work was instrumental in taking the data presented here, and to our extremely dedicated sample growers including Dharmalingam Prabhakaran and Danny Woodruff who deserve far more credit than they get.

A very special thanks has to go to the many other people I know in the Clarendon Laboratory, and particularly to my office mates in 106 Craig Topping and Franz Lang who have spent a significant proportion of the the past four years answering my questions. There are too many others of you to name everyone here, but you know who you are and I could never have got through it without your support, advice and friendship. I don't know how I'll cope without tea time at 11(:20)am and 4(:20)pm!

Outside of physics I am extremely grateful to all of my friends in Oxford, both old and new, for their support, and especially to my long-time friend and flatmate Haden Spence who has been through the whole 8 years with me.

The final word of thanks must go to my family, for their unfailing love, support and advice.

And if I don't know the answer, how do I know what I don't know?
- Justin, STOP the Musical

Contents

Chapter 1

Introduction

1.1 Quantum Materials

In popular science discussions quantum mechanics, along with its seemingly strange and counter-intuitive effects, is often described as 'the science of the very small'. In some sense this statement is true - if you look at any isolated atom or particle on a small enough length scale, the laws of quantum mechanics will be crucial in governing its behaviour. When we put atoms together in certain, ordered ways, however, it is possible for the 'small-scale' effects of quantum mechanics to act co-operatively across the whole material and fundamentally alter the behaviour on a macroscopic scale.

'Quantum Materials' is the term used to describe the remarkably broad group of materials in which such co-operative, macroscopic quantum effects occur. They have been and continue to be the subject of intense research with a huge variety of fascinating and useful states of matter being discovered, many of which are vital to technology we use every day.

In this thesis I shall describe in detail my research into three novel quantum materials which together exhibit ordered and disordered magnetism, density waves, and unconventional, high-temperature superconductivity, beginning with a brief theoretical overview of these effects. There are a large number of other fascinating phenomena seen in related quantum materials including topological materials, multiferroics, semiconductors,

molecular magnets and thin films to name a few, which I do not touch on in this work. Good texts for the interested reader on these and other topics within quantum materials can be found in Refs. [1–5].

1.2 Magnetism

Magnetic effects are very widespread amongst quantum materials and the materials discussed in this thesis are no exception. In this section I shall present some of the key ideas in the physics of magnetism, beginning with isolated atoms before moving onto the cooperative effects seen when atoms are brought together in condensed matter. It should be noted that magnetism is a very broad field, extending well beyond the scope of this thesis. Some useful books for the interested reader can be found in Refs. [5, 6].

1.2.1 Basic Definitions

Before we begin it is necessary to establish some basic definitions of important concepts in magnetism. The basic object is the magnetic dipole moment, which is analogous to an electric dipole, and for which I shall use the symbol $\boldsymbol{\mu}$. In classical mechanics, magnetic dipoles are caused by small current loops, with the relationship

$$\mathrm{d}\boldsymbol{\mu} = I\mathrm{d}\mathbf{S} \tag{1.1}$$

where $\mathrm{d}\mathbf{S}$ is the area of an infinitesimal loop around which a current I flows. For larger current loops we can integrate this relationship across the area enclosed by the loop to find the total moment $\boldsymbol{\mu}$. This indicates that the magnetic moment has SI unit $\mathrm{A\,m^2}$ ($= \mathrm{J\,T^{-1}}$), although at various points in this thesis I shall also quote magnetic moments in their 'CGS' unit emu, where $1\,\mathrm{emu} = 10^{-3}\,\mathrm{A\,m^2}$.

A current loop represents orbital motion of electric charge, so a magnetic dipole is always associated with an angular momentum, $\mathbf{L}$. The proportionality constant γ such that $\boldsymbol{\mu} = \gamma\mathbf{L}$ is known as the gyromagnetic ratio.

These definitions can be extended to the orbital motion of electrons in atoms, since

these are essentially charges moving around a small loop. Some care is required in taking into account the effects of quantum mechanics however it can be shown that, for an electron with orbital angular momentum $\mathbf{L}$,

$$\boldsymbol{\mu} = -\mu_{\mathrm{B}}\mathbf{L} \tag{1.2}$$

where the Bohr magneton

$$\mu_{\mathrm{B}} = \frac{e\hbar}{2m_e} \tag{1.3}$$

is a convenient unit determining the order of magnitude of atomic magnetic moments and the minus sign in equation 1.2 is due to the negative charge of the electron.

In addition to orbital angular momentum, quantum mechanics dictates that the electron has a spin, $\mathbf{S}$, which also contributes to the angular momentum, so the complete relationship is actually

$$\boldsymbol{\mu} = -\mu_{\mathrm{B}}(\mathbf{L} + g_S\mathbf{S}) \tag{1.4}$$

where the constant g_S is known as the 'g-factor' of the electron, with $g_S = 2.002319$ (which is approximated as 2 for most experimental purposes). By analogy, equation 1.4 is commonly written with an additional factor g_L in the first term, where $g_L = 1$.

With these definitions established we can also define the magnetisation $\mathbf{M}$ as the magnetic moment per unit volume, which we often treat on macroscopic length scales, i.e. averaged over a macroscopic sample so that only the cumulative effect of a large number of atomic dipoles is relevant.

Magnetic fields are described by two, related vector fields $\mathbf{B}$ and $\mathbf{H}$ where

$$\mathbf{B} = \mu_0(\mathbf{H} + \mathbf{M}) \tag{1.5}$$

and $\mu_0 = 4\pi \times 10^{-7}\,\mathrm{H\,m^{-1}}$ is the permeability of free space. In free space we can set $M = 0$, so for external fields applied to condensed matter systems we shall often use the

relationship

$$\mathbf{B}_{\text{ext}} = \mu_0 \mathbf{H}_{\text{ext}}. \tag{1.6}$$

For small enough external fields, a condensed matter system will always show a linear response such that

$$\mathbf{M} = \chi \mathbf{H} \tag{1.7}$$

where χ is the magnetic susceptibility, defined as

$$\chi = \lim_{H \to 0} \frac{M}{H}. \tag{1.8}$$

If the applied field is oscillatory ($H_{\text{ext}} = H_0 \exp(i\omega t)$), the magnetisation will show an oscillatory response which may have both in-phase and out-of-phase components, meaning χ may be complex. It is therefore common to write

$$\chi(\omega) = \chi'(\omega) - i\chi''(\omega). \tag{1.9}$$

In this thesis we shall also be interested in the strength and character of magnetic *fluctuations* in quantum materials. Since these will have some length scale governed by their wavevector $\mathbf{q}$, it is common to define the generalised susceptibility via

$$\chi(\omega, \mathbf{q}) = \chi'(\omega, \mathbf{q}) - i\chi''(\omega, \mathbf{q}) \tag{1.10}$$

implying that the response to a spatially homogeneous external magnetic field is governed by the $\mathbf{q} = 0$ fluctuations. This makes sense since a perfectly homogeneous external magnetic field only has one Fourier component at $\mathbf{q} = 0$, and we can expect that if a material shows stronger inherent fluctuations in the $\mathbf{q} = 0$ channel it will therefore show a stronger response to an external magnetic field with the same periodicity.

1.2.2 Magnetism of Isolated Ions

We shall first consider the magnetic response of a single, isolated ion. The basic Hamiltonian for electron i with spin $\boldsymbol{\sigma}_i = \hbar \mathbf{s}_i$ which is attached to such an ion in external magnetic field $\mathbf{B} = B\hat{\mathbf{z}}$ is

$$\mathcal{H}_i = \mathcal{H}_i^0 + \mu_{\mathrm{B}} \mathbf{B} \cdot (\mathbf{l}_i + g_s \mathbf{s}_i) + \frac{e^2}{2m_e} \frac{1}{4} |\mathbf{B} \times \mathbf{r}_i|^2 \tag{1.11}$$

where $\mathcal{H}_i^0$ is the Hamiltonian in zero external field due to the Coulomb interaction with the nucleus and other electrons, $\hbar \mathbf{l}_i = \mathbf{r}_i \times \mathbf{p}_i$ is the electron's orbital angular momentum and $g_s \simeq 2$ is the spin g-factor of the electron [5]. The overall Hamiltonian for all of the electrons is then

$$\mathcal{H} = \sum_i \mathcal{H}_i. \tag{1.12}$$

The magnetism of the electrons given by these expressions dominates over any magnetic behaviour of the atomic nucleus; this is because the nuclear magneton μ_{N} is proportional to $1/m_{\mathrm{p}}$, as opposed to $1/m_{\mathrm{e}}$ for the Bohr magneton μ_{B}, meaning the magnetic response of the nucleus is smaller than that of the electrons by a factor of approximately $m_{\mathrm{e}}/m_{\mathrm{p}} \sim 10^{-4}$ and can normally be neglected.

Initially we shall be interested in the low-field behaviour of this Hamiltonian. For $B = 0$ there will be some set of eigenstates $\{|n\rangle\}$ which satisfy $\mathcal{H}_0 = \sum_i \mathcal{H}_i^0 |n\rangle = E_n |n\rangle$, where $|0\rangle$ is the ground state. We then have under standard perturbation theory the change in energy when a small magnetic field is applied to second order in $B = |\mathbf{B}|$,

$$\begin{aligned} \Delta E_n = \mu_{\mathrm{B}} \mathbf{B} \cdot \langle n | \sum_i (\mathbf{l}_i + g_s \mathbf{s}_i) |n\rangle + \frac{e^2}{8m_e} B^2 \langle n | \sum_i (x_i^2 + y_i^2) |n\rangle \\ + \sum_{n \neq n'} \frac{| \langle n | \mu_{\mathrm{B}} \mathbf{B} \cdot \sum_i (\mathbf{l}_i + g_s \mathbf{s}_i) |n'\rangle |^2}{E_n - E_{n'}}. \end{aligned} \tag{1.13}$$

In evaluating the matrix elements in this expression, it will be useful to define the total angular momentum $\mathbf{J} = \sum_i (\mathbf{l}_i + \mathbf{s}_i)$ and the Landé g-factor g_J such that

$$g_J \mathbf{J} \cdot \mathbf{B} = \sum_i (\mathbf{l}_i + g_S \mathbf{s}_i) \cdot \mathbf{B}. \tag{1.14}$$

The three terms in equation 1.13 all lead to distinct types of magnetic behaviour, and we shall consider them in turn.

Paramagnetism

The first term in equation 1.13 is the only one 1st order in B and will dominate for small B, provided the term is non-zero. In order to evaluate it we need to establish how the individual orbital and spin angular momenta $\mathbf{l}_i$ and $\mathbf{s}_i$ couple together so that we can find the expectation value $\langle n| \sum_i (\mathbf{l}_i + g_s \mathbf{s}_i) |n\rangle$ among the eigenstates $\{|n\rangle\}$ of the zero-field Hamiltonian $\mathcal{H}_0$. For the purposes of this section, we shall restrict ourselves to states $\{|n_{\mathrm{GS}}\rangle\}$ which are part of the ground state multiplet, since these will govern the low-temperature behaviour.

$\mathcal{H}_0$ will in general contain contributions from the Coulomb interaction with the nucleus, the inter-electron Coulomb repulsion and the spin-orbit interaction

$$\mathcal{H}_0 = \mathcal{H}_{\mathrm{nuc}} + \mathcal{H}_{\mathrm{e-e}} + \mathcal{H}_{\mathrm{SO}}. \tag{1.15}$$

We will make the approximation that electrons in different shells do not interact with each other (e.g. the $3d$ electrons are not significantly affected by the $4s$ electrons) so that we can treat a single electron shell in isolation. Under this approximation the two parts of the Coulomb interaction can be parametrised in terms of three 'Racah parameters' A, B and C [7], or equivalently by the intra- and inter-orbital Coulomb interactions U and U' and the Hund's Coupling J_{H}, with the relationship [7]

$$\begin{aligned} J_{\mathrm{H}} &= 3B + C \\ U &= A + 4B + 3C \\ U' &= A - 2B + C. \end{aligned} \tag{1.16}$$

Physically, U is the Coulomb repulsion between two electrons in the same orbital

(necessarily, therefore, with different spin), U' is the Coulomb repulsion between two electrons in different orbitals and J_{H} is the exchange integral between electrons in two orbitals which favours alignment of electron spins. Matrix elements of the Coulomb interaction as a function of the Racah parameters for different electron shells and configurations have been tabulated for example in Ref. [8], allowing exact diagonalisation calculations to be performed.

The spin-orbit interaction coupling spin and orbital angular momenta can be expressed as a function of a single parameter ζ_{SO}

$$\mathcal{H}_{\mathrm{SO}} = \sum_i \zeta_{\mathrm{SO}} \mathbf{l}_i \cdot \mathbf{s}_i \tag{1.17}$$

with $\zeta_{\mathrm{SO}} \sim Z^4$, where Z is the ion's nuclear charge [9]. The spin-orbit interaction is therefore significantly stronger near the bottom of the periodic table.

In determining how the spin and orbital degrees of freedom couple together, we will be interested in two possible limits.

In the 'LS-coupling' limit, we assume the spin-orbit coupling is weak compared to the Coulomb interaction ($\zeta_{\mathrm{SO}} << J_{\mathrm{H}}$). This means that the Coulomb interaction first couples together the spatial parts of the wavefunction forming some total orbital angular momentum $\mathbf{L} = \sum_i \mathbf{l}_i$ and, via the Hund's exchange, couples the spins to form a total spin $\mathbf{S} = \sum_i \mathbf{s}_i$. The spin-orbit interaction then couples $\mathbf{L}$ and $\mathbf{S}$ to form a total angular momentum $\mathbf{J} = \mathbf{L} + \mathbf{S}$. The famous Hund's rules provide a method to find the ground state eigenvalues L, S and J in this limit [6]:

1. The individual electron spins $\mathbf{s}_i$ align as much as possible, maximising $S = \sum_i m_{s,i}$.

2. Electrons are distributed amongst different orbitals in the way which maximises the total orbital angular momentum $L = \sum_i m_{l,i}$.

3. L and S either align or anti-align to give $J = |L \pm S|$, with $+$ for a shell which is more than half filled and $-$ for one which is less than half filled.

The first two of these rules maximise the energy gain due to the Coulomb attraction to the nucleus and ensure the overall wavefunction is antisymmetric under exchange of any two electrons, while the last minimises the spin-orbit coupling. In this limit basis states of the zero-field Hamiltonian are labelled by the good quantum numbers $\{L, S, J, m_J\}$. More detailed justifications for these rules can be found in Ref. [5].

Hund's rules allow us to calculate the angular momenta L, S and J, however in order to find the magnetic moment of the ion we also need to know the magnetic g-factor. Noting that $g_S = 2$ and $g_L = 1$, it can be shown that [6]

$$g_J = \frac{3}{2} + \frac{S(S+1) - L(L+1)}{2J(J+1)}. \tag{1.18}$$

The opposite limit is the 'jj-coupling' limit in which the spin orbit coupling is stronger than Coulomb effects, meaning that $\mathbf{l}_i$ and $\mathbf{s}_i$ are first coupled together to form an overall angular momentum $\mathbf{j}_i$ for each electron, before the $\mathbf{j}_i$ are coupled together under the Coulomb interaction to from the overall J. In this limit, basis states of the zero-field Hamiltonian are labelled by the good quantum numbers $\{j_i, J, m_J\}$.

Whichever limit we are in, we can now calculate the expectation value of interest $\mathbf{B} \cdot \langle n_{\mathrm{GS}}| \sum_i (\mathbf{l}_i + g_s \mathbf{s}_i) |n_{\mathrm{GS}}\rangle = \mathbf{B} \cdot \langle n_{\mathrm{GS}}| g_J \mathbf{J} |n_{\mathrm{GS}}\rangle = B \langle n_{\mathrm{GS}}| g_J J_z |n_{\mathrm{GS}}\rangle = B g_J m_J$ where $m_J = -J, -J+1, ..., J-1, J$ labels the ground state multiplet.

We would like to calculate the moment per atom μ of this state, which can be done via the partition function Z

$$Z = \sum_{m_J} \exp\{\beta \mu_{\mathrm{B}} g_J m_J B\}, \tag{1.19}$$

$$\mu = -\frac{\partial k_{\mathrm{B}} T \ln Z}{\partial B} \tag{1.20}$$

where $\beta = k_{\mathrm{B}} T$ and T is the temperature. The result is the Brillouin function [5]

$$\mu = g_J \mu_{\mathrm{B}} J \left\{ \frac{2J+1}{2J} \coth\left(\frac{2J+1}{2J} \frac{g_J \mu_{\mathrm{B}} J B}{k_{\mathrm{B}} T} \right) - \frac{1}{2J} \coth\left(\frac{1}{2J} \frac{g_J \mu_{\mathrm{B}} J B}{k_{\mathrm{B}} T} \right) \right\} \tag{1.21}$$

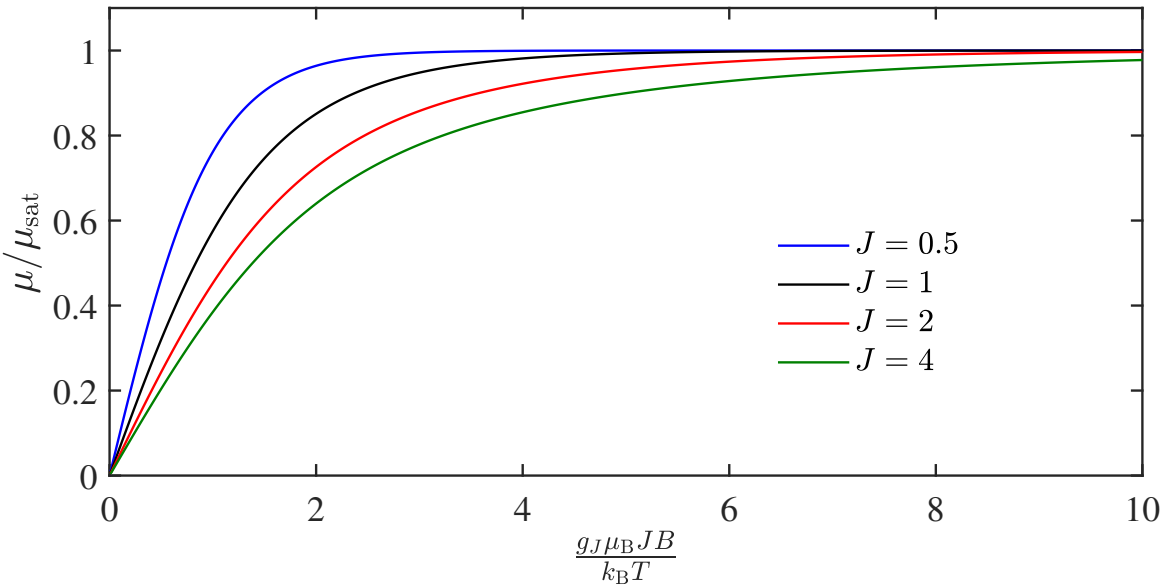

Figure 1.1: The Brillouin function expressed in equation 1.21 for some different values of J, where $\mu_{\rm sat} = g_J\mu_{\rm B}J$.

which is plotted in Fig. 1.1. The moment is positive for positive B, so this represents a paramagnetic contribution. The low-field susceptibility per site is given by

$$\chi = \lim_{H\to 0}\frac{\partial\mu}{\partial H} = \frac{\mu_0\mu_{\rm B}^2 g_J^2 J(J+1)}{3k_{\rm B}T} \tag{1.22}$$

which is the famous Curie law, while in the high-field limit $g_J\mu_{\rm B}JB \gg k_{\rm B}T$ the moment saturates to a constant value $\mu_{\rm sat} = g_J\mu_{\rm B}J$ per site.

Non-interacting ions with spin $J \neq 0$ will display magnetic behaviour as discussed here. This is most often realised in ions with unpaired, localised electrons, for example among the $3d$ and $4f$ elements. In real systems, however, the precise value of J can be different to that predicted by Hund's rules due to a variety of non-local effects which will be discussed in later sections, for example the crystal field and superexchange interactions.

Larmor Diamagnetism

If $J \neq 0$, the first term in equation 1.13 will dominate the magnetic behaviour. If $J = 0$, however, we must consider second order terms. We shall now examine the second term, which, for a rotationally symmetric atom ($x_i^2 = y_i^2 = z_i^2 = r_i^2/3$), is

$$\delta E_n = \frac{e^2}{12m_e} B^2 \langle n| \sum_i r_i^2 |n\rangle . \tag{1.23}$$

Electron wavefunctions will have radii of order the atomic radius $\bar{r}_{\text{atom}}$, so we make the approximation

$$\langle n| \sum_i r_i^2 |n\rangle \simeq N_e \bar{r}_{\text{atom}}^2 \tag{1.24}$$

where N_e is the number of electrons, yielding a moment

$$\mu = -\frac{e^2}{6m_e} N_e \bar{r}_{\text{atom}}^2 B \tag{1.25}$$

and susceptibility

$$\chi_{\text{Larmor}} = -\frac{e^2 \mu_0 N_e \bar{r}_{\text{atom}}^2}{6m_e}. \tag{1.26}$$

All the quantities in equation 1.26 are positive, so $\chi_{\text{Larmor}} < 0$ and this is a diamagnetic contribution. It is simply proportional to the number of electrons in the ion so all electrons including core electrons in filled shells contribute. This contribution ensures that all materials, even 'non-magnetic' materials with $J = 0$ like water and organic compounds, show at least a small diamagnetic response to an external field.

Van-Vleck Paramagnetism

It remains to consider the third term in 1.2

$$\delta E_{\text{vv}} = \sum_{n \neq n'} \frac{|\langle n| \mu_{\text{B}} \mathbf{B} \cdot \sum_i (\mathbf{l}_i + g_s \mathbf{s}_i) |n'\rangle|^2}{E_n - E_{n'}} \tag{1.27}$$

which gives rise to a 'Van-Vleck' contribution to the susceptibility

$$\chi_{\text{vv}} = 2\mu_0 \mu_{\text{B}}^2 \sum_{n \neq 0} \frac{|\langle 0| J_z |n\rangle|^2}{E_n - E_0} \tag{1.28}$$

which involves a sum over excited states $|n\rangle$. $E_n - E_0 > 0$, so this is a paramagnetic (positive) contribution to the susceptibility. In general it is weak since it contains the factor $1/(E_n - E_0)$ which is usually small. However, if there is a fairly low-lying excited state with non-zero J it can become comparable to or stronger than the Larmor contribution. Van-Vleck paramagnetism is commonly observed in ions with $L = S \neq 0$, such that they cancel out to give $J = 0$ for the ground state under Hund's Rules. In this situation there will be an excitation which involves re-orienting $\mathbf{L}$ and $\mathbf{S}$ so that they don't cancel out which will likely have a low energy cost ($\sim \zeta_{\mathrm{SO}}$) and non-zero J.

1.2.3 Magnetism of Ions in Crystals

In the materials discussed in this thesis, I shall be studying magnetic ions in a crystalline environment which are *not* isolated. This can give rise to a variety of co-operative effects beyond the single-ion case.

Crystal Electric Field Effects

We shall first consider the case where the electrons are still confined on the magnetic ions (i.e. no electron hopping), but the ions are in a crystal environment. An example is the MO_6 octahedra found in many transition metal oxides, in which we can often approximate the d electrons as being confined on the metal site M but feeling an external electric field of octahedral symmetry due repulsion from the electrons on the neighbouring O sites. The single-ion Hamiltonian is modified to

$$\mathcal{H}_0 = \mathcal{H}_{\mathrm{nuc}} + \mathcal{H}_{\mathrm{e-e}} + \mathcal{H}_{\mathrm{CF}} + \mathcal{H}_{\mathrm{SO}} \tag{1.29}$$

where $\mathcal{H}_{\mathrm{CF}}$ is the crystal field Hamiltonian and it is in general unclear which components in this Hamiltonian are the strongest because, for example, the strength of the crystal field depends on the bond lengths to nearby atoms. The crystal field will split some or all of the single-ion energy levels and L, S and J may or may not remain good quantum numbers depending on its rotational symmetry and strength. In the general case, a crystal field Hamiltonian of any symmetry can be expressed as a matrix in the basis

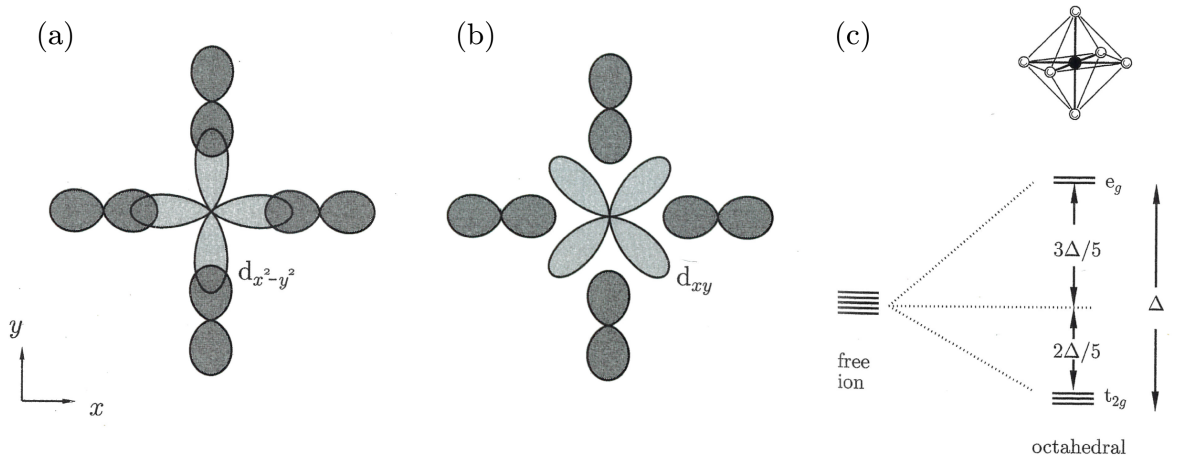

Figure 1.2: (a–b) Schematic of the angular part of electron wavefunctions for the oxygen p orbitals and metal $d_{x^2-y^2}$ and d_{xy} orbitals in a MO_6 octahedral complex. (c) The resulting energy level splitting of the metal d shell. Figure reproduced from Ref. [5].

of single ions states with some parameters which will depend e.g. on bond lengths or the magnitude of crystallographic distortions, then the total Hamiltonian in equation 1.29 can be numerically diagonalised in this basis. If the crystal field is of relatively high symmetry there will be relatively few free parameters in the matrix representation of $\mathcal{H}_{\mathrm{CF}}$ in this basis, which may allow the parameters to be refined against experimental data obtained for example by resonant inelastic x-ray scattering (RIXS, see Section 2.5.1).

One case of particular note is a strong crystal field ($\langle\mathcal{H}_{\mathrm{CF}}\rangle \gg J_H, \zeta_{\mathrm{SO}}$) of octahedral ($\mathrm{O_h}$) symmetry, which is the symmetry in e.g. a perfect MO_6 octahedron. The MO_6 octahedron is a very stable environment for transition metal ions and many oxide quantum materials of interest have this structure, or a small distortion away from it. In this case the metal d orbitals (which feel the strongest crystal field) are split into three t_{2g} states (d_{xy}, d_{xz}, d_{yz}) which are lower in energy, corresponding to orbitals with electron density concentrated in directions away from the neighbouring oxygen sites, and two e_g states ($d_{x^2-y^2}, d_{z^2}$) which are higher in energy and have maximum electron density in the directions towards the oxygen sites. This situation is illustrated in Fig. 1.2. In this type of ion the t_{2g} states form a triplet and the e_g a doublet, amongst which the electrons are distributed according to Hund's rules. The effective L, S and J values thus obtained can be very different from the free ion values - for example, the d^2 configuration yields $L = 3$, $S = 1$, $J = 2$ in the free-ion limit but $L_{\mathrm{eff}} = 1$, $S_{\mathrm{eff}} = 1$, $J_{\mathrm{eff}} = 0$ in a strong

octahedral crystal field.

1.2.4 Magnetism in Metals

Next, we introduce hopping between the different magnetic sites in a crystal. In many materials this results in metallic behaviour, and the delocalised conduction electrons in a metal will exhibit magnetism of their own. For example, the Fermi sea is polarisable and will split into spin-up and spin-down bands when exposed to an external field. The electron spins interact with the $\mathbf{B}$ field with an energy $+g_S\mu_\mathrm{B}\mathbf{B}\cdot\boldsymbol{\sigma}$, meaning states with spin anti-aligned with $\mathbf{B}$ move to lower energy while those with spin parallel to $\mathbf{B}$ move to higher energy. In the ground state there will therefore be more electrons with spin anti-aligned with $\mathbf{B}$, leading to a net spin polarisation $\langle\boldsymbol{\sigma}\rangle \propto -\mathbf{B}$. Since the electrons have negative charge, the resulting moment $\boldsymbol{\mu} \propto -\boldsymbol{\sigma} \propto \mathbf{B}$ will be parallel to the field, leading to a paramagnetic contribution to the susceptibility. A more precise derivation of this 'Pauli' contribution as presented e.g. in Ref. [6] yields

$$\chi_\mathrm{Pauli} = \mu_0\mu_\mathrm{B}^2 g(E_\mathrm{F}) \tag{1.30}$$

where $g(E_\mathrm{F})$ is the density of states at the Fermi surface.

It can be shown that $g(E_\mathrm{F}) \propto 1/T_\mathrm{F}$ [6], so the susceptibility due to the conduction electrons is smaller than that due to any localised (Curie-like) paramagnetic moments by a factor of $T/T_\mathrm{F} \sim 300/30,000 = 1/100$ for typical metals at room temperature. Given this suppression of the Pauli contribution, even for $J = 0$ ions it is unclear whether the Pauli contribution or the Larmor diamagnetism due to core electrons will be larger; for example, metallic copper is diamagnetic for this reason.

There is also a smaller, diamagnetic contribution due to the orbital motion of the conduction electrons which can be shown to be [5]

$$\chi_\mathrm{Landau} = -\frac{1}{3}\chi_\mathrm{Pauli}. \tag{1.31}$$

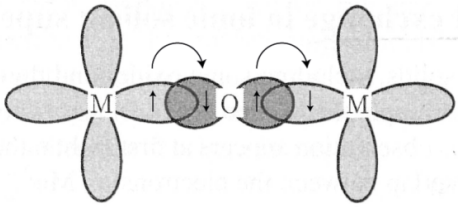

Figure 1.3: A simplified metal-oxygen-metal bond in a MO_6 complex, showing the spins of electrons in each orbital (small arrows) and some possible superexchange hopping pathways. Figure adapted from Ref. [5].

1.2.5 Magnetic Superexchange

If electrons are allowed to hop, moments on neighbouring magnetic ions can become coupled to one another. To take one simplified example shown in Fig. 1.3, in a situation where two metal ions are connected by an intermediate oxygen ion the spins on the metal ions become antiferromagnetically coupled to one another. If the spin of an electron in a d orbital on the metal site is anti-parallel with that of the electron in a p orbital on the O^{2-} site with which there is a significant overlap integral, the hopping amplitude is increased compared to the situation where these electrons have parallel spins as a result of the Pauli exclusion principle preventing the two electrons occupying the same orbital and having the same spin. If the hopping is increased the electrons become more spread out and their kinetic energy is decreased, meaning there is an energy saving for all of the electron spins to be anti-parallel, as shown in Fig. 1.3. The two moments on neighbouring metal sites are therefore antiferromagnetically coupled with some superexchange energy ΔE_{SE}.

In different bonding geometries and when many orbitals are considered determining the magnitude or even sign of superexchange can become a much more complex problem, however it is common to find some kind of coupling between neighbouring spins in a crystal.

If superexchange is present then, by analogy to the band structure of electrons in a metal, we can expect each of the single ion magnetic levels to broaden into k-dependent bands of magnetic modes, as illustrated in Fig. 1.4 [10]. This can lead to a variety of interesting cooperative effects.

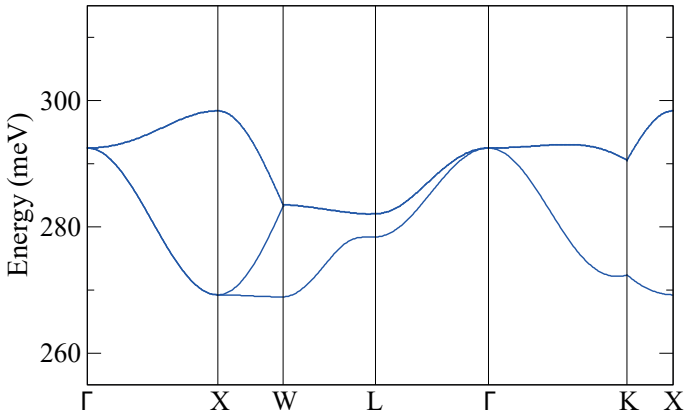

Figure 1.4: The calculated dispersion of a magnetic mode in one theory of the double perovskite iridates. Figure reproduced from Ref. [10].

1.2.6 Excitonic Magnetism

In materials where the ground state is non-magnetic ($J_{\text{eff}} = 0$) but there is a low lying excited state which is magnetic, for example in ions whose ground state has $L_{\text{eff}} = S_{\text{eff}} \neq 0$ and $J_{\text{eff}} = 0$ as discussed in Section 1.2.2, superexchange can broaden the excited state but will not affect the ground state. This is the situation represented in Fig. 1.4. The case shown in the figure is the calculated dispersion of an excited state in the double-perovskite iridate Sr_2YIrO_6, which has quite weak superexchange. The bandwidth of the excited mode can be shown to be proportional to the square of the superexchange strength [10], so in materials with stronger superexchange the minimum of the excitation will move to lower energies until at some critical value of the superexchange strength it will touch $E = 0$, i.e. the energy of the non-magnetic (and hence non-dispersive) ground state, at some $\mathbf{k}$. Beyond this point, the minimum energy of the system occurs when the modes at the bottom of the excitation band are spontaneously occupied in a process which is analogous to Bose-Einstein condensation. Since these modes have non-zero J, the system will spontaneously develop a ground state paramagnetic moment whose precise magnitude is dependent on the details of the crystal geometry and superexchange strength.

The mechanism discussed above is often called 'excitonic magnetism' and represents a novel way to obtain an emergent ground-state magnetic moment in ions which have

$J = 0$ in the single-ion limit. It requires a very specific set of circumstances including a low-lying excited state and strong superexchange to occur, however, and has only rarely been observed with one example in the $4d$ ruthenates [11]. My work searching for an experimental realisation of excitonic magnetism in $5d$ osmates forms a major part of this thesis, Chapter 5.

1.2.7 Magnetic Order

In the presence of inter-site interactions like superexchange between dipole magnetic moments it is common for the lowest energy state at zero temperature to be magnetically ordered, meaning that the moments are correlated with one another over long distances. Magnetic order is generally viewed from two complementary perspectives.

In insulating materials with localised spins S, the spins are thought of as small magnetic dipoles fixed to their respective sites in the crystal and allowed to rotate on that site. The interactions then add contributions to the Hamiltonian which give energy gains or penalties depending on the relative alignment of nearby spins. Additionally, there may be anisotropy terms which favour spins aligning in certain directions due, for example, to the local crystal field at the magnetic sites. All of these (often complicated) interactions are ultimately the result of the Coulomb interaction between the different electrons and between the electrons and the nuclei, however they can often be described more simply by an effective Hamiltonian which only contains spin operators. Which precise form of Hamiltonian best models a given system depends on details like the microscopic exchange mechanism and dimensionality, however one of the most common examples is the 3-dimensional Heisenberg model

$$\mathcal{H} = -\sum_{\langle i,j \rangle} \mathcal{J}_{ij} \mathbf{S}_i \cdot \mathbf{S}_j - D \sum_i (S_i^z)^2 \tag{1.32}$$

where $\langle i, j \rangle$ are usually chosen to be all pairs of neighbouring spins S_i and S_j. The exchange parameters $\mathcal{J}_{ij}$ can in general be bond-dependent but are usually chosen to be isotropic, with their sign determining whether the coupling is ferromagentic ($\mathcal{J}_{ij} > 0$,

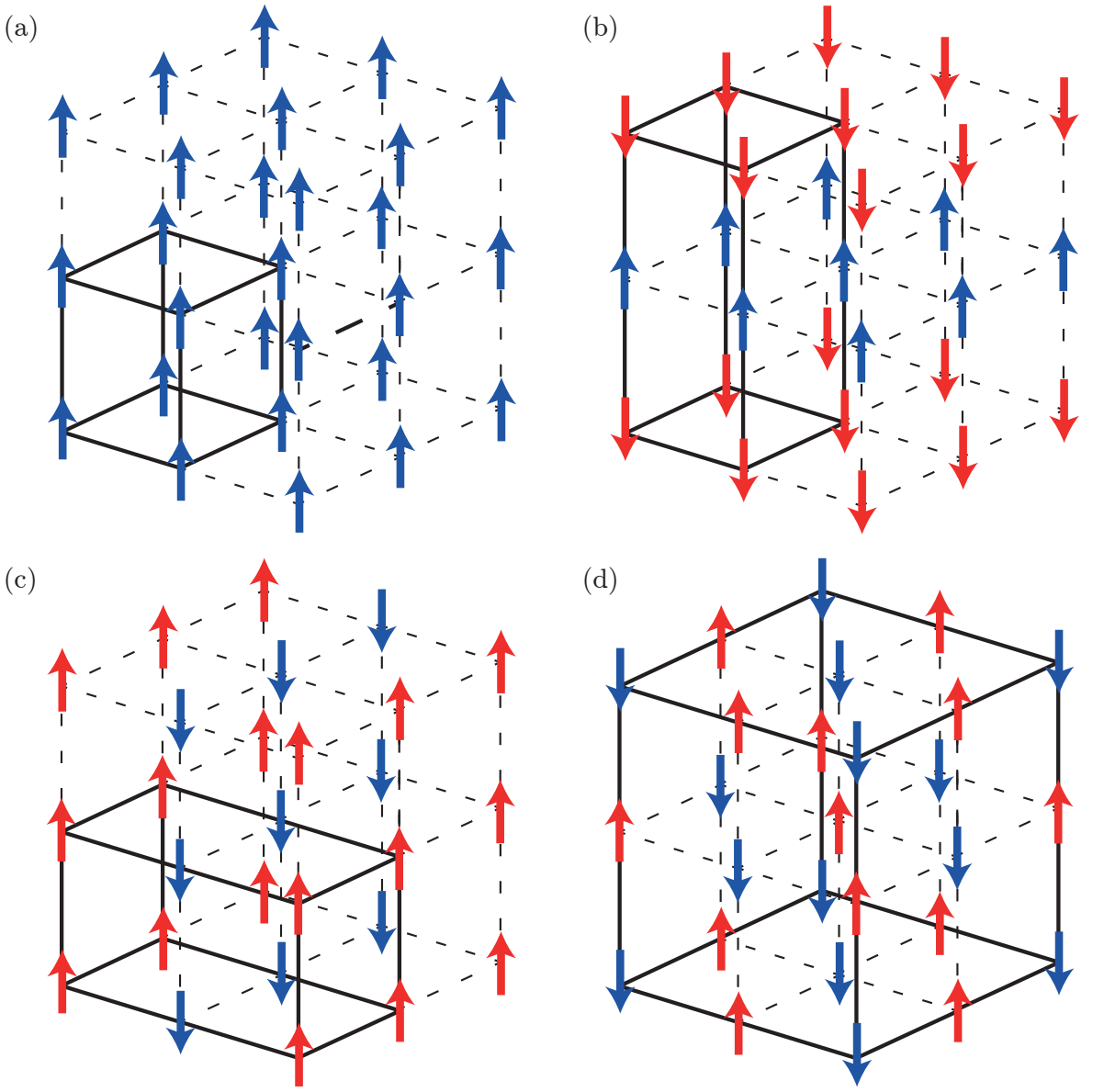

Figure 1.5: A selection of possible ordered states of spins on a tetragonal lattice. Solid lines mark a single magnetic unit cell in each case. (a) ferromagnetic (FM), $\mathbf{q} = (0, 0, 0)$ (b) Layered A-type antiferromagnetic (AFM), $\mathbf{q} = (0, 0, \pi/c)$ (c) single-stripe (C-type) AFM, $\mathbf{q} = (\pi/a, 0, 0)$ (d) Néel AFM, $\mathbf{q} = (\pi/a, \pi/a, \pi/c)$.

spins tend to align) or antiferromagnetic ($\mathcal{J}_{ij} < 0$, spins tend to anti-align). D is a uniaxial anisotropy which favours spins lying along z ($D > 0$) or in the xy-plane ($D < 0$).

This Hamiltonian can have a wide variety of ordered ground states. A selection of those relevant for later chapters in this thesis are shown schematically in Fig. 1.5, including the ferromagnetic state (all spins aligned) and several different antiferromagnetic ones (some or all neighbouring spins anti-aligned).

Fig. 1.5 makes it apparent that there are many different possible types of order in 3D systems, and the words 'ferromagnetic' and 'antiferromagnetic' are not enough to distinguish them. Instead, ordered states are usually classified by a propagation vector $\mathbf{k}$ which describes the full periodicity in all dimensions relative to the underlying crystal lattice along with a basis which give the moment direction on each site in the magnetic unit cell. Ferromagnetic states then have a propagation vector $\mathbf{k} = 0$ and the many possible antiferromagnetic states tend to have at least one component of $\mathbf{k}$ equal to π/a_i where a_i is the lattice constant in the relevant direction. Within this formalism we can also take into account other, more exotic types of order, for example helical magnetic structures with incommensurate propagation vectors where one or more component of $\mathbf{k}$ is not a simple fraction of π/a_i.

In all of these ordered states there will be some temperature above which thermal effects dominate and the magnetic order is destroyed. This means there will be a magnetic phase transition temperature, often labelled T_{N} or T_{c}, at which the thermal energy is roughly equal to the exchange energy per spin in the ordered state. The precise value of the transition temperature can be difficult to calculate accurately since it depends on the magnetic fluctuations in the system, however the 'Weiss mean-field theory' is a good first approximation which is often used. This theory assumes each magnetic ion experiences an effective, internal magnetic field $\mathbf{B}_{\mathrm{int}}$ due to all the other spins and develops a magnetic moment as a result. Since it is possible to write $\mathbf{B}_{\mathrm{int}}$ in terms of the moments on the other magnetic sites in the system and all sites are assumed to be crystallographically equivalent, the spontaneous magnetisation can be found self-consistently. If a term

for an external magnetic field is included, the susceptibility of this model can also be calculated. In both the ferromagnetic and Néel-antiferromagnetic cases the mean-field susceptibility takes the 'Curie-Weiss' form

$$\chi = \frac{C}{T - \theta} \tag{1.33}$$

where θ is the Weiss temperature and $C = \frac{\mu_0 \mu_B^2 g_J^2 J(J+1)}{3k_B}$ is the Curie constant as discussed in Section 1.2.2 [5]. $\theta > 0$ if the exchange coupling is ferromagnetic and $\theta < 0$ if it is antiferromagnetic, and $|\theta|$ is proportional to the strength of the coupling. The full expression is

$$\theta = \pm \frac{2z|\mathcal{J}|J(J+1)}{3k_B} \tag{1.34}$$

with the + for the ferromagnet and − for the antiferromagnet, where z is the coordination number (number of nearest neighbours at each site) and $\mathcal{J}$ is the nearest-neighbour exchange energy.

Although an analytical derivation showing Curie-Weiss-like susceptibility is only possible for a limited selection of simple microscopic models, it is common to see approximately Curie-Weiss-like behaviour in the magnetic susceptibility in real materials at high temperatures, including in many which show more exotic ordered or disordered ground states than those discussed here. In these cases the Curie constant still gives a rough estimate of the effective dipole moment on the magnetic sites and the Weiss temperature gives an estimate of the average spin-spin coupling, along with its ferromagnetic or antiferromagnetic nature. Fitting experimental magnetic susceptibility data to this relationship at high temperature is therefore a very common and useful first step in characterising a magnetic system.

In the discussion of ordered states so far I have discussed only local-moment magnetism, in which permanent dipole moments are confined to individual crystallographic sites. It is also possible for the itinerant electrons of the Fermi sea in a metal to show

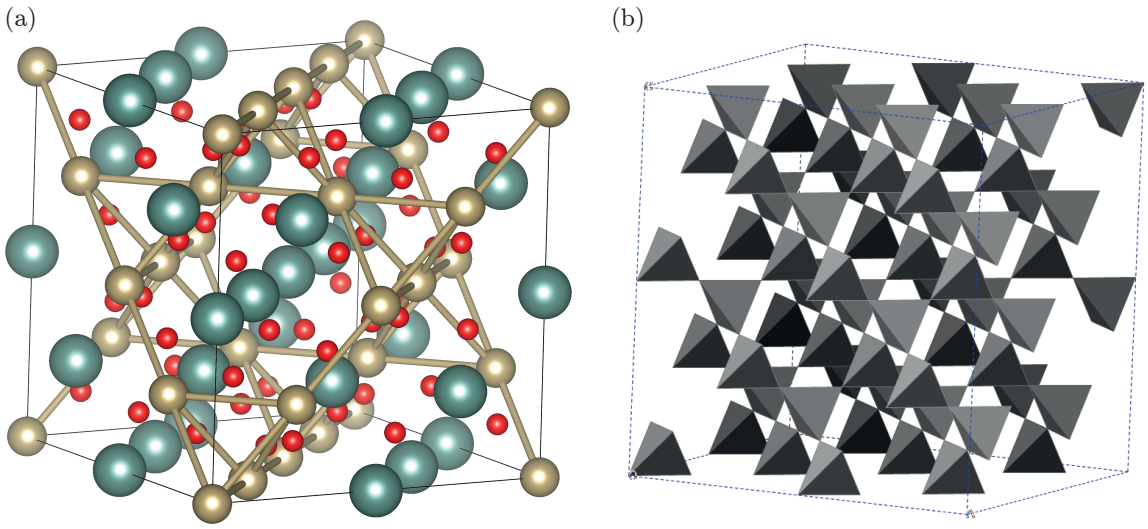

Figure 1.6: (a) One unit cell of the pyrochlore crystal structure, which contains corner-sharing tetrahedra with magnetic ions (gold) situated on the corners. (b) Representation of the corner-sharing tetrahedra over several unit cells.

magnetic order, for example in the form of spin-density waves (SDW), although the magnetism in such a state tends to be weaker than localised dipole moments since only a small fraction of the electrons participate, i.e. those near the Fermi surface. I shall examine the physics of such density waves in more detail in Section 1.3.

1.2.8 Magnetic Frustration

In the discussion of magnetic order so far we assumed that a unique ground state exists which minimises the exchange energy on each individual bond simultaneously. There are many real materials, however, in which this is not the case and we say that the moments are 'frustrated'. An example which has been central to my work is the pyrochlore crystal structure (Fig. 1.6), which contains a network of corner-sharing tetrahedra with magnetic sites situated on each corner. If the spins in this structure are coupled antiferromagnetically to their nearest neighbours along the sides of the tetrahedra, the geometry of the structure means that there is no possible arrangement of spins which simultaneously minimises the energy on all bonds. Instead, the ground state is *macroscopically degenerate*, i.e., there are a large number of ground states of order one per magnetic site which all have the same energy. To see why this is the case, let us consider for example an arrangement of spins on a tetrahedron where two spins point down and two up, and all

spins are confined along a single, common axis. This configuration then minimises the antiferromagnetic bond energy within the tetrahedron. There are, however, 6 different ways to choose the directions of the four spins which satisfy the conditions stated here, meaning there are 6 degenerate ground states of the individual tetrahedron. For any one of these 6 states there are then 3 possible arrangements of the remaining three spins on the tetrahedra which share a corner with the original one. If we continue in this way we obtain of order one ground state per magnetic site (i.e. $\sim 10^{23}$ for a macroscopic crystal), all of which are degenerate. This is of course a toy model of one very specific situation, however it illustrates the point that for a system with non-orthogonal magnetic bonds and antiferromagnetic coupling it is possible to have a macroscopically degenerate ground state.

In addition to geometrical frustration, it is also possible for frustration to be realised due to crystallographic disorder. For example in a non-magnetic material with a small concentration of magnetic impurities which are distributed randomly the bond lengths and directions between pairs of atoms will have some related, random distribution. It is possible for the magnitude and even sign of the magnetic exchange along such bonds to be bond-length-dependent [5]. In this situation the random nature of the bonding ensures a single, ordered ground state which minimises all bond energies does not exist, again leading to frustration and in many cases behaviours similar to those seen in geometrically frustrated systems.

Physical systems with a macroscopically degenerate ground state are often unstable, since any small perturbation (for example a small crystalline distortion) is likely to quench at least some of the frustration, reducing the number of ground states and lowering the energy of the system. This sensitivity to perturbations makes the physics of frustrated magnets incredibly rich with many exotic ground states being realised in real materials, for example the spin glass, spin ice, spin liquid and some helical magnetic structures. In this thesis I shall examine only one of these, the spin glass, since this is the one which features prominently in my research. Review papers for the interested reader

which go into detail on many of the other novel magnetic states realised in frustrated systems can be found in Refs. [12–15].

1.2.9 Spin Glasses

Spin glass behaviour occurs in inherently frustrated systems which, theoretically, are required to show some degree of disorder [15], for example in the locations of the magnetic sites ('site-randomness') or in the strength and sign of nearest-neighbour exchange ('bond-randomness'). Assuming the frustration is not lifted by any other instability, as the system is cooled down the spin fluctuations slow down gradually, often forming locally-correlated clusters which grow as the temperature drops. Spins within a cluster will fluctuate together, gradually slowing down as the temperature falls and the cluster grows, while spins not in clusters fluctuate independently and contribute to inter-cluster interactions. Eventually at some temperature T_{f} the clusters merge and all of the spins 'freeze' into a random arrangement, selecting one of the macroscopically degenerate ground states. The freezing process appears to be some kind of cooperative phase transition, however its precise nature is not fully understood [5]. There is some evidence that a few spins, or possibly some small clusters, can remain paramagnetic even below T_{f}, however the majority of spins must freeze so that the spin frozen state can spread cooperatively throughout the whole sample [15].

Originally, spin-glass behaviour was thought to be confined to strongly disordered systems, with notable examples being dilute metal alloys such as $\mathrm{Ag}_{1-x}\mathrm{Mn}_x$ [16] with x being a few % or less. These materials have an inherently random distribution of magnetic sites (site-randomness) and have the useful property that the concentration can be easily varied, allowing some tuning of the moment distribution. It was later observed experimentally, however, that spin-glass behaviour can also occur in geometrically frustrated systems seemingly with no disorder like the pyrochlore $\mathrm{Y_2Mn_2O_7}$, however a mechanism involving disordered microscopic strain has now been proposed which may explain this [17].

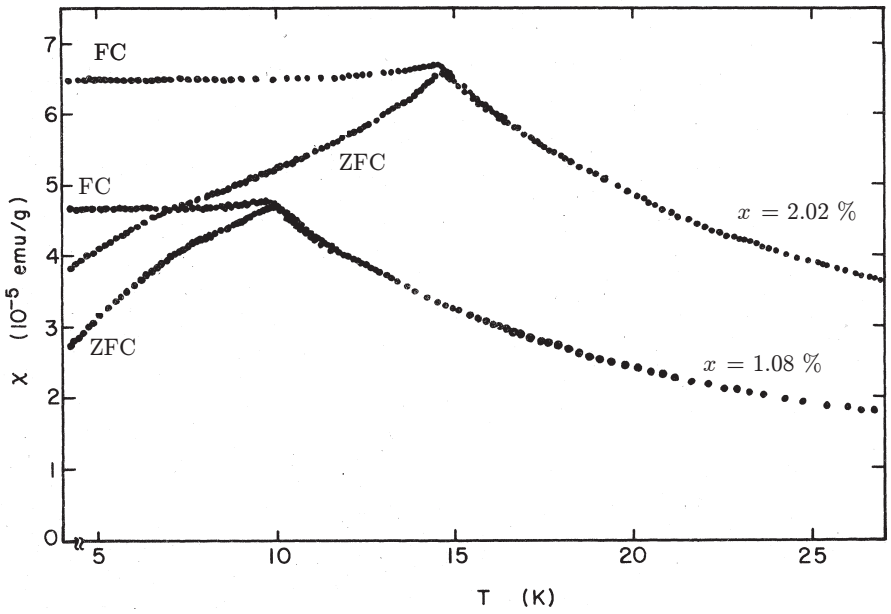

Figure 1.7: Magnetic susceptibility of the spin glass $Ag_{1-x}Mn_x$ at two values of x. Figure reproduced from Ref. [18].

Signatures of Spin Glass Behaviour

Below T_f the sample will show significant hysteresis since there is likely to be an energy barrier between the ground state it has frozen into and any of the other, degenerate ground states [15]. This hysteresis is the most easily detectable signature of a spin glass, appearing most clearly in DC magnetisation data. Upon cooling below T_f there is a splitting between the field cooled (FC) and zero field cooled (ZFC) magnetic susceptibilities, as shown in Fig. 1.7, which represents the fact that the sample takes longer than the measurement timescale of a DC magnetometer (between a few minutes and a few hours) to respond to the application of an external field. A more subtle signature is that the susceptibility gradually departs from Curie-Weiss behaviour at a much higher temperature $T \sim 10\,T_f$ due to the formation and growth of non-paramagnetic clusters. When measured in higher fields a hysteresis in the DC magnetisation is also usually observed along with a gradually-decaying remanent magnetisation when quenched from high field. The remanence shows that there are very slow magnetic fluctuations on timescales of minutes or hours present in the system.

Spin glasses also show clear signatures in AC magnetic susceptibility $\chi(\omega)$, with a peak in the real part whose temperature varies slightly with frequency ω, as well as the

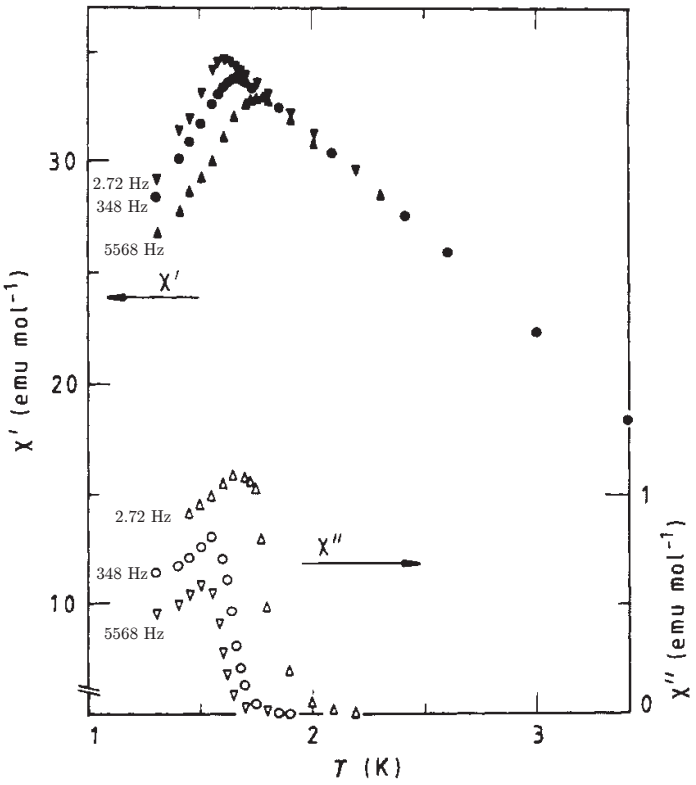

Figure 1.8: AC magnetic susceptibility of the spin glass $(Eu_{0.4}Sr_{0.6})S$. Figure reproduced from Ref. [19].

onset of a non-zero imaginary part near T_f which is related to dissipation in the system (Fig. 1.8).

Another important technique for characterising spin-glasses is muon spin relaxation (μSR), since the implanted muon measures the internal magnetic field and fluctuations in the sample directly and on a different timescale (μs) to those accessible via AC magnetisation measurements. When exposed to a static internal field (see below for the meaning of static in this context), the muon will precess around that field. If there is a random distribution of static fields the overall muon polarisation will show the well-studied 'Kubo-Toyabe' relaxation shown in Fig. 1.9 with an initial dip and characteristic '1/3-tail' [20] caused by the precession of muons at different sites gradually becoming out of phase with one another. It is worth noting that any field which varies on a timescale much greater than the muon decay time (a few μs) will appear static in μSR. If there are magnetic fluctuations on the muon timescale these will couple to the muon spin and gradually destroy the polarisation, leading to an exponential or stretched-exponential-

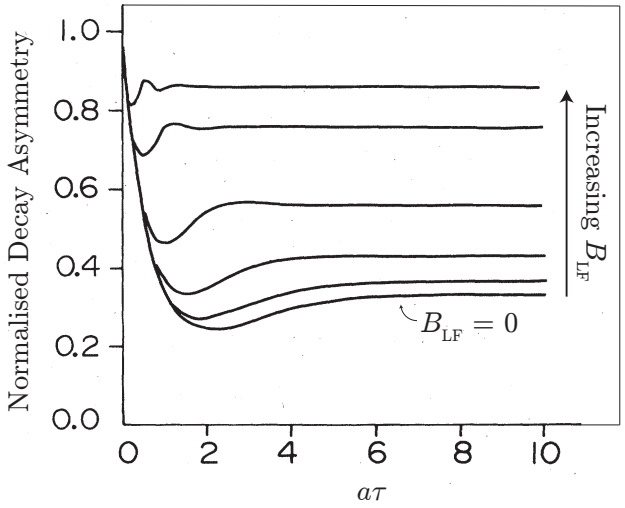

Figure 1.9: Calculated μSR response of a spin glass with a random distribution of static fields at the muon stopping sites as a function of applied longitudinal field B_{LF}. τ is the muon decay time and a is a parameter of the field distribution. Figure reproduced from Ref. [20].

like relaxation. A combination of static and fluctuating components will lead to some intermediate behaviour [20], with the exact shape of the spectrum being dependent on the relative strength of the different components. μSR spectra like that shown in Fig. 1.10 are typical of spin-glasses, with their precise shape yielding useful information about the internal fields and dynamics in the sample.

1.3 Density Waves

We shall now consider the response of the Fermi sea in a metal to a spatially-varying magnetic field, $\mathbf{H}(\mathbf{r}) = \sum_{\mathbf{q}} \mathbf{H}_{\mathbf{q}} \cos(\mathbf{q} \cdot \mathbf{r})$, where we have broken the field down in terms of Fourier components $\mathbf{H}_{\mathbf{q}}$. It can be shown that for a multi-band system, the static ($E = 0$) magnetic susceptibility is [21]

$$\chi_{\mathbf{H}}(\mathbf{q}, E = 0) = \frac{\chi^0_{\mathbf{H}}(\mathbf{q}, E = 0)}{1 - X_{\mathbf{H}}(\mathbf{q})\chi^0_{\mathbf{H}}(\mathbf{q}, E = 0)} \tag{1.35}$$

where $X_{\mathbf{H}}(\mathbf{q})$ is a function containing information about the strength of spin-spin interactions (i.e. the exchange strength) and $\chi^0_{\mathbf{H}}(\mathbf{q}, E = 0)$ is the 'bare' susceptibility per unit energy evaluated at zero energy.

The bare susceptibility is the generalised susceptibility if the electrons were non-

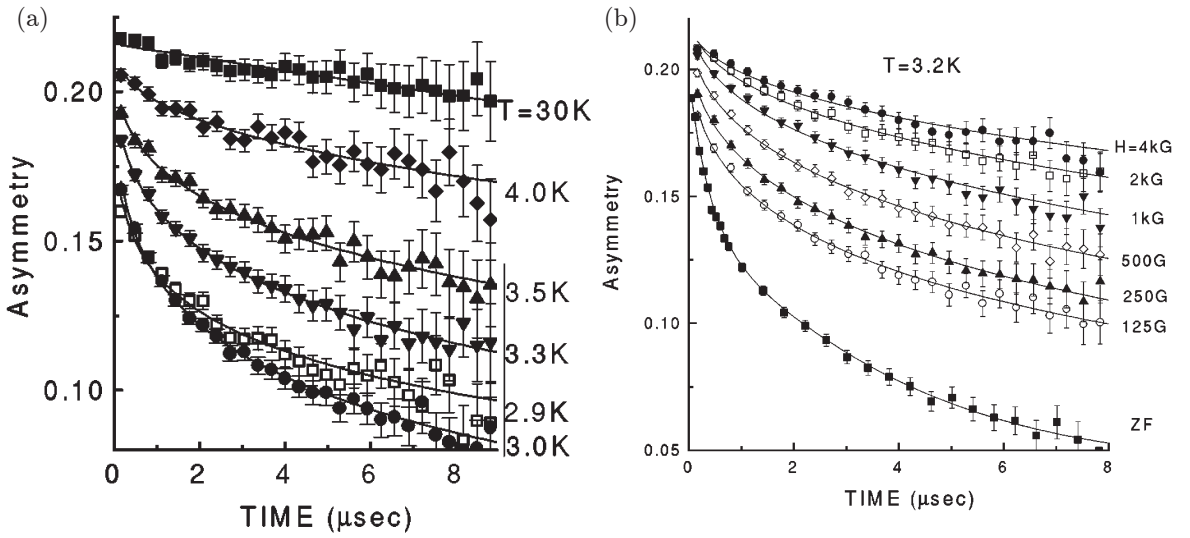

Figure 1.10: μSR response of a typical spin glass, $Ag_{1-x}Mn_x$ ($x = 0.5\%$), as a function of (a) temperature and (b) applied longitudinal field. Figure reproduced from Ref. [16].

interacting and contains details of the band structure. It is proportional to a factor

$$\chi^0_{\mathbf{H}}(\mathbf{q}) \propto \sum_{\mathbf{k},i,j} \frac{f(E^i_{\mathbf{k}+\mathbf{q}}) - f(E^j_{\mathbf{k}})}{E^i_{\mathbf{k}+\mathbf{q}} - E^j_{\mathbf{k}}} \tag{1.36}$$

where $f(E)$ is the Fermi occupation factor at energy E, $E^i_{\mathbf{k}}$ is the energy of band i at wavevector $\mathbf{k}$ and the sums are over the Brillouin zone ($\mathbf{k}$) and bands indexed by i and j [21].

Before examining this any further, it is instructive to consider the analogous derivation for a spatially-varying *electric* field, $\mathbf{E}(\mathbf{r}) = \sum_{\mathbf{q}} \mathbf{E}_{\mathbf{q}} \cos(\mathbf{q} \cdot \mathbf{r})$, which can be found in Ref. [22]. The result is remarkably similar

$$\chi_{\mathbf{E}}(\mathbf{q}, E = 0) = \frac{\chi^0_{\mathbf{E}}(\mathbf{q}, E = 0)}{1 - X_{\mathbf{E}}(\mathbf{q})\chi^0_{\mathbf{E}}(\mathbf{q}, E = 0)} \tag{1.37}$$

where the bare susceptibility $\chi^0_{\mathbf{E}}(\mathbf{q}, E = 0)$ differs from the magnetic case only by constant factors and $X_{\mathbf{E}}(\mathbf{q})$ similarly contains information about the interactions.

We are interested to look for points in $\mathbf{q}$ space where either of these susceptibilities diverge, since these will represent instabilities of the system. Such a divergence could either occur because the bare susceptibility diverges, or because $1 - X(\mathbf{q})\chi^0(\mathbf{q}, E = 0) = 0$. I shall examine these cases in order.

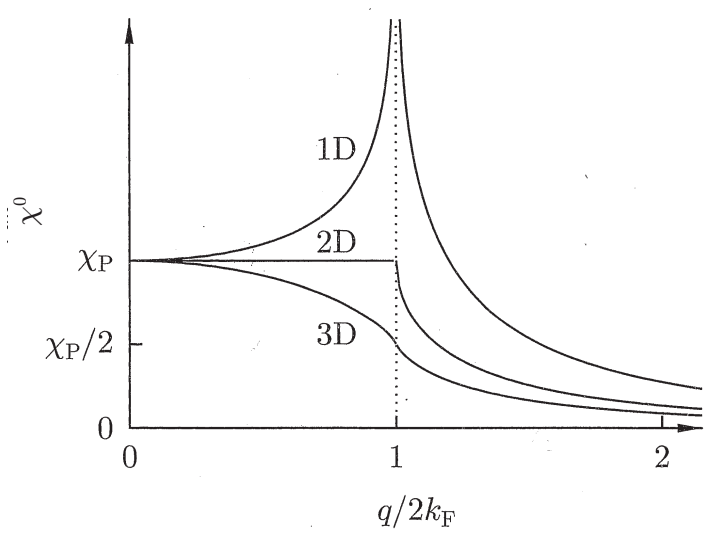

Figure 1.11: The bare magnetic susceptibility χ^0 for a single, isotropic band in different dimensions. χ_P is the Pauli susceptibility as discussed in Section 1.2.4. Figure reproduced from Ref. [5].

Calculation of the bare susceptibility is discussed in detail in Ref. [22]. For the simple case of a single, isotropic band the results are reproduced in Fig. 1.11. In 1D the bare susceptibility diverges at $2k_F$, while it is non-divergent and reduces in value as the dimensionality increases. The divergence is related to the factor $E^i_{\mathbf{k}+\mathbf{q}} - E^j_{\mathbf{k}}$ in the denominator of the bare susceptibility, which will be zero when there are states on the Fermi surface connected ('nested') by a wavevector $\mathbf{q}$ (more precise details of the mathematical derivations behind this can be found in Ref. [22]). The Fermi surface in 1D is perfectly nested by the wavevector $q = 2k_F$, which causes the divergence in χ^0. In 2D and 3D the nesting becomes only partial, with its strength decreasing as the dimensionality increases [21].

For the more complex, multiband Fermi surfaces found in real materials the calculation of χ^0 can become very complex. The general principles that χ^0 will be peaked at wavevectors which connect (nest) parallel sections of Fermi surface and that nesting is stronger as the effective dimensionality of the system is reduced are however still true, although it should be noted that a mathematical divergence in χ^0 is not possible in dimensions above 1D [22].

Since in real materials it is not possible for χ^0 to show a strict divergence, we now turn to the denominator of equation 1.37, which is interaction-dependent. The susceptibility

clearly diverges if $\chi^0(\mathbf{q}, E = 0)X(\mathbf{q}) = 1$ at any $\mathbf{q}$, although it can be shown that $\chi^0(\mathbf{q}, E = 0)X(\mathbf{q}) \geq 1$ at some $\mathbf{q}$ is a sufficient condition for instability [22].

The functions $X_{\mathbf{E}}(\mathbf{q})$ and $X_{\mathbf{H}}(\mathbf{q})$ have been calculated in Ref. [22] for the simplified case of zero electron-phonon and spin orbit couplings, with the results that SDW instability occurs if

$$\bar{V}_{\mathbf{q}} \gtrsim \frac{1}{\chi^0_{\mathbf{H}}(\mathbf{q}, E = 0)} \tag{1.38}$$

and that CDW instability occurs if

$$\bar{V}_{\mathbf{q}} - 2\bar{U}_{\mathbf{q}} \gtrsim \frac{1}{\chi^0_{\mathbf{E}}(\mathbf{q}, E = 0)} \tag{1.39}$$

where $\bar{V}_{\mathbf{q}}$ and $\bar{U}_{\mathbf{q}}$ are spatially-averaged Fourier components with wavevector $\mathbf{q}$ of the exchange and direct parts of the Coulomb (electron - electron) interaction respectively.

Considering magnetic instability first, we see that once the exchange parameter $\bar{V}_{\mathbf{q}}$ is large enough the system is likely to be most unstable at the value of $\mathbf{q}$ where the bare susceptibility is peaked, i.e. the wavevector at which Fermi surface nesting is strongest. When instability occurs at one particular value of $\mathbf{q} = \mathbf{q}_{\mathrm{SDW}}$, a wave will spontaneously appear in the magnetisation of the system with the same periodicity, $\mathbf{M} = \mathbf{M}_0 \cos(\mathbf{q}_{\mathrm{SDW}} \cdot \mathbf{r})$. Such a wave represents a periodic modulation of the density of each spin state (i.e. $\rho_\uparrow \sim \cos(\mathbf{q}_{\mathrm{SDW}} \cdot \mathbf{r})$, $\rho_\downarrow \sim \cos(\mathbf{q}_{\mathrm{SDW}} \cdot \mathbf{r} + \pi)$), and is therefore called a 'spin density wave' (SDW). Upon entering the SDW state the Fermi surface is altered drastically ('reconstructed'), usually removing any further nesting and preventing SDWs at other wavevectors or charge order from developing.

It can be shown that $\bar{V}_{\mathbf{q}} < 2\bar{U}_{\mathbf{q}}$ [22]. This means that, in the absence of electron-phonon coupling, the magnetic susceptibility will always diverge before the electric (charge) susceptibility and a CDW cannot occur. In the presence of electron-phonon coupling the situation changes, however, because the spatial charge modulation of a CDW can couple to phonons of the same periodicity, encouraging a CDW. In a simpli-

fied model with a single phonon band it can be shown that if

$$\frac{4\bar{\eta}_{\mathbf{q}}^2}{\hbar\omega(\mathbf{q})} - (2\bar{U}_{\mathbf{q}} - \bar{V}_{\mathbf{q}}) \gtrsim \frac{1}{\chi^0_{\mathbf{E}}(\mathbf{q}, E=0)} \tag{1.40}$$

a phonon mode becomes soft, corresponding to a coupled lattice distortion and commensurate CDW with the same periodicity, where $\bar{\eta}_{\mathbf{q}}$ is the matrix element of the electron-phonon interaction and $\omega(\mathbf{k})$ is the dispersion relation of the phonon mode in the absence of electron-phonon coupling [22].

By contrast, in the absence of spin-orbit coupling the SDW is *not* affected by electron-phonon coupling, since spatial charge distribution is uniform in a SDW. This means that interactions with the lattice can provide a route for CDW instability to form in preference to SDW.

The above arguments do break down in the presence of significant spin-orbit coupling, however it is still useful to note that in lighter elements where spin-orbit coupling is weak instability of the charge susceptibility $\chi_{\mathbf{E}}$ is favoured by electron-phonon coupling.

If the different couplings are such that the charge susceptibility diverges before the spin channel, a periodic charge modulation or charge density wave (CDW) will occur ($\rho_\uparrow = \rho_\downarrow \sim \cos(\mathbf{q}_{\mathrm{CDW}} \cdot \mathbf{r})$). Due to the important role of electron-phonon coupling in their formation it is common for CDWs to be commensurate and accompanied by a lattice distortion of the same periodicity (i.e. at the same $\mathbf{q}$) as the CDW. A material which shows such a commensurate CDW is the subject of one of the main chapters of this thesis (Chapter 4). SDWs are more likely to be incommensurate than CDWs since there is no particular reason why the strongest Fermi surface nesting should happen to fall at a wavevector $\mathbf{q}$ which is a simple fraction of a reciprocal lattice vector. However, in the presence of spin-orbit coupling the phonon degrees of freedom may favour commensurate SDW order along with a lattice distortion. Such order is important in the physics of unconventional superconductors, which are the subject of Section 1.4.

For both SDWs and CDWs, only the electrons close to the Fermi surface are involved in the ordering. This means that density wave (DW) states can be quite subtle and

difficult to detect; in particular, the magnetism from SDW order can be expected to be significantly weaker than that from local-moment magnetism. The strongest signatures of both types of density waves occur in the electrical resistivity and magnetic susceptibility, which for a metallic system depend strongly on the Fermi surface and will therefore show noticeable anomalies when Fermi surface reconstruction occurs. Anomalies seen with these techniques can also be caused by a large variety of other, non-DW phenomena however, so other techniques are required to confirm the presence of DW order.

In cases where a lattice distortion develops, this distortion may be observable via elastic x-ray and/or neutron scattering (Section 2.3). The positions and intensities of superstructure peaks in principle carry information about the periodicity and atomic displacements in the distorted structure, however these are sometimes quite weak relative to nearby Bragg peaks of the undistorted structure meaning high-intensity sources are required. A demonstration of this type of measurement is the subject of Chapter 4.

Direct measurements of the CDW charge modulation are difficult but can be achieved by resonant and non-resonant x-ray scattering and scanning tunnelling microscopy (STM), the latter of which also carries information about the energy gap associated with CDW formation. The spin modulation in a SDW can be probed directly via neutron scattering, especially polarised neutron scattering where the magnetic cross-section can be isolated from other contributions.

Angle resolved photoemission spectroscopy (ARPES) can also be used to probe the electronic band structure above and below the density wave transition temperature T_{DW}. This can allow observation of the energy gap as well as periodicity via band folding and give information about the precise bands and nested sections of Fermi surface involved in DW formation.

1.4 Superconductivity

Since its discovery in 1911 by Kamerlingh Onnes [23], superconductivity has been one of the most fascinating and useful effects in condensed matter, remaining the subject of

intense study over 100 years later. Superconductivity is a cooperative state of matter in which all of the conduction electrons form a single, macroscopic quantum state across the whole sample. As such, it is one of the most stark realisations of quantum mechanics on a macroscopic scale. Upon cooling below some critical temperature T_c a superconductor will exhibit zero resistance to the flow of electricity, as well as the 'Meissner' effect [24] in which the material excludes all magnetic flux from its interior when placed in a magnetic field, i.e. perfect diamagnetic behaviour.

The first microscopic theory of superconductivity was BCS (Bardeen-Cooper-Schreiffer) theory [25], which rose to prominence in the 1950s. In BCS theory, the electron-phonon interaction with a crystal lattice causes an attraction between pairs of electrons with opposite spins, leading to the formation of 'Cooper pairs' once $k_B T$ falls below the attractive pairing energy. A spin-0 singlet pair of electrons like this forms a boson, and bosons do not have to obey an exclusion principle like fermions. The Cooper pairs can therefore 'condense', all occupying the lowest-energy state even at finite temperature. Since the pairs all occupy the same state, all of the electrons involved form a single, macroscopic state across the whole material.

BCS theory explained all the known properties of superconductors at the time well including the zero electrical resistance and Meissner effect. It also made some predictions, including the 'isotope effect': since the pairing strength is determined by the electron-phonon coupling, T_c should be dependent on the isotopes used in the sample, since different isotopes have different nuclear masses which changes the phonon frequencies. The isotope effect is indeed observed in many superconductors, which we today term 'conventional' superconductors since they are explained by the conventional BCS theory.

In the 1980s, researchers began discovering 'unconventional' superconductors experimentally which could not be explained by BCS theory, including most notably high-temperature copper oxide compounds with $T_c > 100\,\mathrm{K}$ [26] (Fig. 1.12). These materials are not predicted to have electron-phonon coupling strong enough to cause such high T_c under BCS theory and do not show an observable isotope effect. A complete theoretical

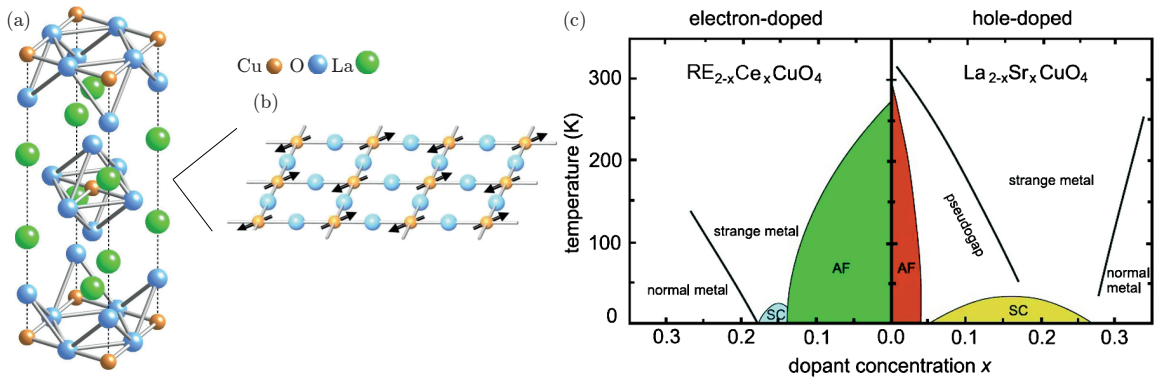

Figure 1.12: (a) the crystal structure of a typical cuprate superconductor, La_2CuO_4. (b) The in-plane antiferromagnetic structure of the AFM phase in the cuprates. (c) Typical phase diagrams for cuprate superconductors. Figure adapted from Ref. [27].

description of the physics of unconventional superconductors has not yet been realised, however the mechanism is widely thought to be related to magnetic fluctuations.

1.4.1 Copper-Oxide Superconductors

The highest critical temperatures are achieved in the cuprate superconductors. These compounds contain copper-oxygen planes stabilised by spacer layers of other materials as illustrated in Fig. 1.12 (a) for the compound $(La_{1-x}Sr_x)_2CuO_4$. The parent compound of this group ($x = 0$) is an antiferromagnetic insulator at low temperatures, with the spins on the Cu sites ordered as depicted in Fig. 1.12 (b). As the composition is altered by increasing x holes are doped onto the CuO_2 planes, resulting in the phase diagram shown in Fig. 1.12 (c). The AFM ordering temperature is gradually reduced on doping, with a novel 'pseudogap' phase appearing first, before superconductivity is seen in a 'dome' which starts close to the point where the AFM ordering is completely suppressed to 0 K. Although magnetic ordering has been suppressed in superconducting samples, it has been shown that strong magnetic fluctuations with similar $\mathbf{q}$ to the ordering wavevector still remain and the prevalent theories propose these magnetic fluctuations as the attractive superconducting pairing interaction. Exotic forms of CDW have also been observed in the pseudogap region, but the significance of these forms of charge order for superconductivity has yet to be established [27, 28]. A detailed examination of the cuprates including the pseudogap and superconducting mechanism can be found in

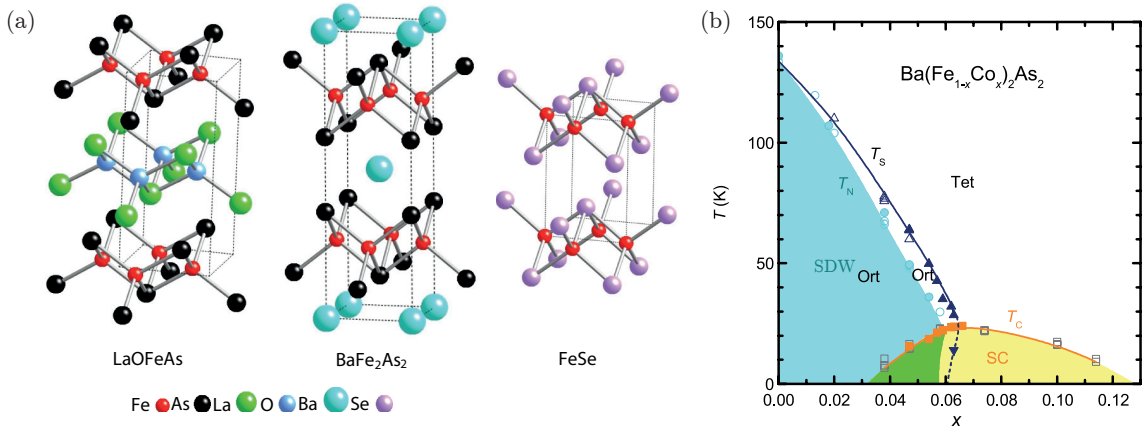

Figure 1.13: (a) the crystal structure some typical iron-based superconductors. (b) The phase diagram for a typical iron-arsenide superconductor. Figure adapted from Ref. [27].

Ref. [27].

1.4.2 Iron-Based Superconductors

In 2008, the first in a new class of unconventional superconductors containing iron was discovered. These materials contain Fe ions in a square planar arrangement, with pnictide (As, P) or chalcogenide (Te, Se, S) sites located just above or below the centres of the Fe squares, as shown in Fig. 1.13 (a). Most compositions also have spacer layers containing cations which stabilise the full tetragonal structure, with the exception of $Fe_{1-y}Se$ and $Fe_{1-y}S$ which can be grown as stable structures without these layers, albeit with a small amount of iron deficiency (y). In the case of FeSe it is possible to chemically intercalate ions (e.g. K^+, Li^+, Na^+, Ba^{2+}) or small molecules (e.g. NH_3) between the layers, allowing some degree of control over the interlayer separation and electronic doping with minimal physical disruption to the active FeSe plane. It has also recently become possible to grow monolayer FeSe on $SrTiO_3$, which has been shown to have a remarkably high $T_c \sim 100\,K$. The physics of one FeSe intercalate, $Li_{1-x}Fe_xOHFe_{1-y}Se$, is the subject of one of the major chapters of this thesis, Chapter 3.

Many of the bulk iron based superconductors (FeSCs) can be modified in a variety of ways, including electron doping ($Ba(Fe_{1-x}Co_x)_2As_2$), hole ($(K_{1-x}Ba_x)Fe_2As_2$) doping and isovalent chemical substitution ($BaFe_2(As_{1-x}P_x)_2$, $Fe_{1-y}(Se_{1-x}S_x)$). In the iron arsenides such as $BaFe_2As_2$ the parent compound usually shows a transition on cooling to

a commensurate SDW state with wavevector $(\pi/a, \pi/a, 0)$ in the Brillouin zone of the tetragonal unit cell, sometimes called the 'stripe SDW' since it has the same symmetry as the C-type AFM structure in Fig. 1.5. This is accompanied by an orthorhombic ('nematic') structural distortion in which the sizes of the in-plane lattice parameters a and b change slightly, with all other features of the structure remaining the same. The SDW wavevector closely matches Fermi surface nesting seen in ARPES [27] and the structural distortion was originally thought to be related to the magnetic order, even though the two transitions do not quite coincide, with the distortion usually occurring a few K above the SDW order as in Fig. 1.13 (b). In $Fe_{1-y}Se$, a structural distortion similar to that in the iron arsenides is seen but there is no accompanying magnetic order, and superconductivity then appears at $T_c \sim 9\,K$ [29]. The lack of magnetic order in $Fe_{1-y}Se$ has prompted several novel proposals to explain the structural distortions in iron based superconductors, although this is the still the source of considerable debate.

Upon doping in the ways listed above, the magnetic and/or structural order is generally suppressed and superconductivity appears, forming a dome whose peak roughly coincides with the doping level where the competing SDW/orthorhombic order would have reached zero temperature (Fig. 1.13 (b)). This phase diagram is very similar to that of the cuprates, and theories involving paring mediated by magnetic fluctuations with the same symmetry as the nearby SDW state have proven quite successful in modelling the physics of the iron-based superconductors, although this is still an area of active debate.

More in-depth review papers on the iron based superconductors can be found in Refs. [27, 30, 31]

1.4.3 Gap Symmetry and the Spin Resonance

Theoretically speaking all superconductors exhibit a gap function $\Delta_{\mathbf{k}}$, which is in general complex and tells us the amplitude and phase of the superconducting state for carriers on the Fermi surface at a point $\mathbf{k}$ in the Brillouin zone [2]. Alternatively, $\Delta_{\mathbf{k}}$ can be thought of as a Fourier coefficient of the real space wavefunction $\Delta(\mathbf{r})$ which tells us

the amplitude and phase of the single, macroscopic quantum state at position $\mathbf{r}$ in the material.

Superconductors are often categorised by the symmetry of the gap function. The band structure and Fermi surface of any material must be unchanged under all symmetry operations of the point group of the crystal structure $\{\hat{R}\}$ as well as the inversion operation ($\mathbf{k} \rightarrow -\mathbf{k}$, labelled $\bar{1}$) if the crystal in non-magnetic. The most useful way to do this is therefore to examine how the gap function transforms under the same symmetry operations, i.e. the point group of the crystal composed with the inversion, $\{\hat{R} \otimes \bar{1}\}$. This involves projecting $\Delta_{\mathbf{k}}$ onto the irreducible representations (irreps) of the relevant group

$$\Delta_{\mathbf{k}} = \sum_{\Gamma m} \eta_{\Gamma m} f_{\Gamma m}(\mathbf{k}) \tag{1.41}$$

where Γ labels the different irreps, $m = 1, ..., d$ labels the components of a d dimensional irrep, the functions $f_{\Gamma m}(\mathbf{k})$ are a set of basis functions for $\mathbf{k}$ space which have the same symmetry properties as irrep Γ and $\eta_{\Gamma m}$ are the projection coefficients. This procedure is discussed in detail in Ref. [2].

For most superconductors it turns out that only one of the coefficients $\eta_{\Gamma m}$ is non-zero, meaning that the superconducting gap has well-defined symmetry under the group $\{\hat{R} \otimes \bar{1}\}$, although there are a few exotic cases where it is possible two coefficients are involved, leading to two closely-spaced critical temperatures seen in specific heat [2]. Under BCS theory the gap function is a constant, $\Delta_{\mathbf{k}} = |\Delta|$, so it transforms under the trivial irrep and is invariant under all symmetry operations in $\{\hat{R} \otimes \bar{1}\}$. This pairing is usually termed 's-wave' since its rotational invariance means it can be written in terms of the s-wave ($l = 0$) spherical harmonic. In fact, the usual definition of 'conventional' superconductivity is that the gap function transforms in the same way as the BCS gap function, i.e. under the trivial irrep of $\{\hat{R} \otimes \bar{1}\}$.

For the unconventional superconductors mentioned in this section the situation is slightly more complicated since the Fermi surface often contains multiple sheets, however

the theory can be extended if we allow there to be different gap functions on the different Fermi sheets $\Delta_{\mathbf{k}}^{j}$, where each of the individual gaps transform under the same irrep.

As a concrete example, a schematic of the possible 2D Fermi surface for monolayer FeSe is shown in Fig. 1.14 together with some possible gap distributions. The s^{+-}–wave gap, for example, has a constant, positive gap function one Fermi sheet and a different, negative but also constant gap function on the other sheet. Each of the individual gap functions is isotropic, so the gap is s-wave, and the $+-$ shows that the gap changes sign between the different Fermi sheets. The d-wave gap function is the same on both Fermi sheets but is not constant across the Brillouin zone; instead, it has a rotational symmetry which is the same as one of the d-wave ($l = 2$) spherical harmonics.

The symmetry and **k**-dependence of the superconducting gap function are important results which differ between the various microscopic theories of superconductivity [27]. Significantly, they are also experimentally observable via a variety of techniques.

If the proposed symmetry constrains the gap to have zero magnitude at some **k** points which are on the Fermi surface, the resulting gap nodes should cause low-energy excitations which persist below T_{c} whose effect can be seen in heat capacity and Nuclear Magnetic Resonance (NMR) measurements. Muon spin rotation measurements can also probe gap nodes via penetration depth measurements [33].

Angle Resolved Photoemission Spectroscopy can give direct information about the **k**-dependence of the magnitude of the gap function, while scanning tunnelling spectroscopy (STS) yields similar information. The possibility of determining the sign distribution via STS has also been realised recently, although this technique is still being developed [34, 35]. Both STS and ARPES are surface probes and have limited k_z-resolution in 3D materials, however.

Inelastic neutron scattering can also give bulk, k_z-sensitive information about the sign distribution of the gap via measurements of the 'spin resonance' [27].

The spin resonance, which has been observed widely in unconventional superconductors including iron arsenides, iron selenides and the cuprates [36–39], is a collective

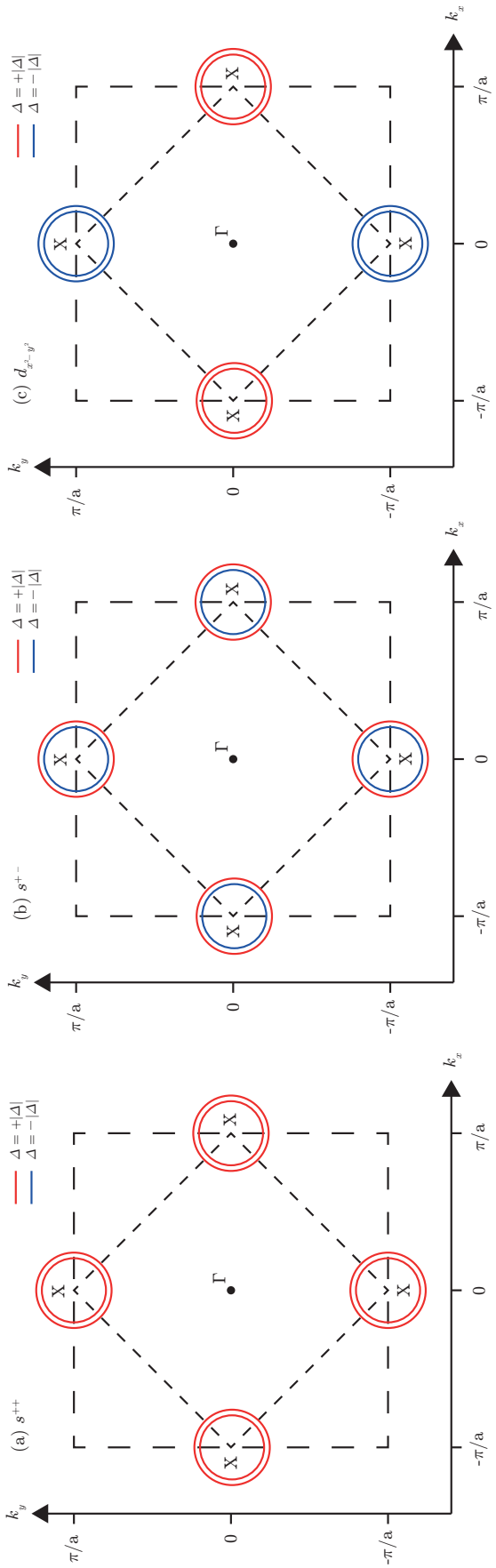

Figure 1.14: Some of the proposed sign distributions of the superconducting gap function Δ on the Fermi surface of monolayer FeSe. (a) s^{++}-wave, (b) s^{+-}-wave, (c) $d_{x^2-y^2}$-wave. The Fermi surface shown here is a schematic representation of that reported in literature [32].

spin excitation that appears below T_c whose signature is a peak in the inelastic neutron scattering spectrum. The resonance peak is centred on a characteristic wavevector $\mathbf{Q}_{\rm res}$ which is often close to or the same as the propagation vector of the antiferromagnetic or SDW phase that borders superconductivity, and the peak appears in a narrow range of energy $E_{\rm res} \simeq 5$–$6\,k_{\rm B}T_c$ just below the maximum of the superconducting gap.

In weak coupling spin fluctuation theories of superconductivity the spin resonance is caused by strong scattering between points on the Fermi surface that are connected by $\mathbf{Q}_{\rm res}$ and have opposite signs of the superconducting gap function. More precisely, for a multiband superconductor the imaginary part of the dynamical magnetic susceptibility at the resonance energy $\chi''(\mathbf{q}, E_{\rm res})$ is proportional to a coherence factor

$$\chi''(\mathbf{q}, E_{\rm res}) \propto \sum_{i,j} \sum_{\mathbf{k},\mathbf{k}'} \Big[1 - \frac{\Delta^i_{\mathbf{k}} \Delta^j_{\mathbf{k}'}}{|\Delta^i_{\mathbf{k}}||\Delta^j_{\mathbf{k}'}|}\Big] \delta(\mathbf{k} - \mathbf{k}' - \mathbf{q}) \tag{1.42}$$

where $\Delta^i_{\mathbf{k}}$ is the superconducting gap function on band i at wavevector $\mathbf{k}$ and the sums are over pairs of Fermi sheets (i, j) and over wavevectors $\mathbf{k}$ and $\mathbf{k}'$ on the Fermi sheets i and j respectively [40, 41]. For real superconducting gap functions the factor in square brackets is 2 if the signs of $\Delta^i_{\mathbf{k}}$ and $\Delta^j_{\mathbf{k}'}$ are opposite and zero if they are the same, and the delta-function means we only see contributions from pairs of points on the Fermi surface separated by $\mathbf{q}$ in reciprocal space. The coherence factor is therefore effectively a nesting integral over the Fermi surface with contributions due to sections with the same sign of Δ removed, so the resonance tends to be sharp in $\mathbf{q}$ when there are parallel sections of Fermi surface with opposite sign of Δ [40, 42–44].

At the very least, unambiguous observation of a spin resonance therefore establishes that a superconductor is unconventional, since there must be sign change on at least some parts of the Fermi surface. Indeed, this was the way that it was originally established that some of the early unconventional superconductors such as the cuprates cannot be explained in BCS theory [2]. Measurements of the momentum dependence of the resonance peak can, however, provide further very useful information on the symmetry of the superconducting gap and the underlying band structure. For example, if it can

be shown to be peaked at a certain wavevector this indicates nesting between sections of Fermi surface with opposite signs of the gap function. A study of the spin resonance in one iron-based superconductor forms one of the core chapters of this thesis, Chapter 3.

Chapter 2

Experimental Methods

I have used a wide variety of experimental techniques to perform the research presented in this thesis. In this chapter I shall give a brief overview of these techniques, including both practical details and the theory behind them, with greater focus on those techniques which were of greater importance in my research. References with more detailed discussions for the interested reader are cited in each section.

2.1 Magnetisation Measurements

Using magnetometry devices such as a Superconducting Quantum Interference Device (SQUID) Magnetometer or Vibrating Sample Magnetometer (VSM), it is possible to measure the AC and DC magnetisation of samples as a function of temperature, magnetic field and frequency. The theory presented in Section 1.2 should make it clear that magnetisation measurements are a crucial piece of information in determining the behaviour of a material experimentally, and indeed a magnetisation study is usually one of the first techniques used to assess a new sample.

2.1.1 DC Magnetisation

Two slightly different pieces of equipment were used to perform the DC magnetisation measurements in this thesis, the SQUID magnetometer [45] and VSM [46] (Fig. 2.1). In both cases, the sample is packed inside a plastic capsule and the capsule placed inside a

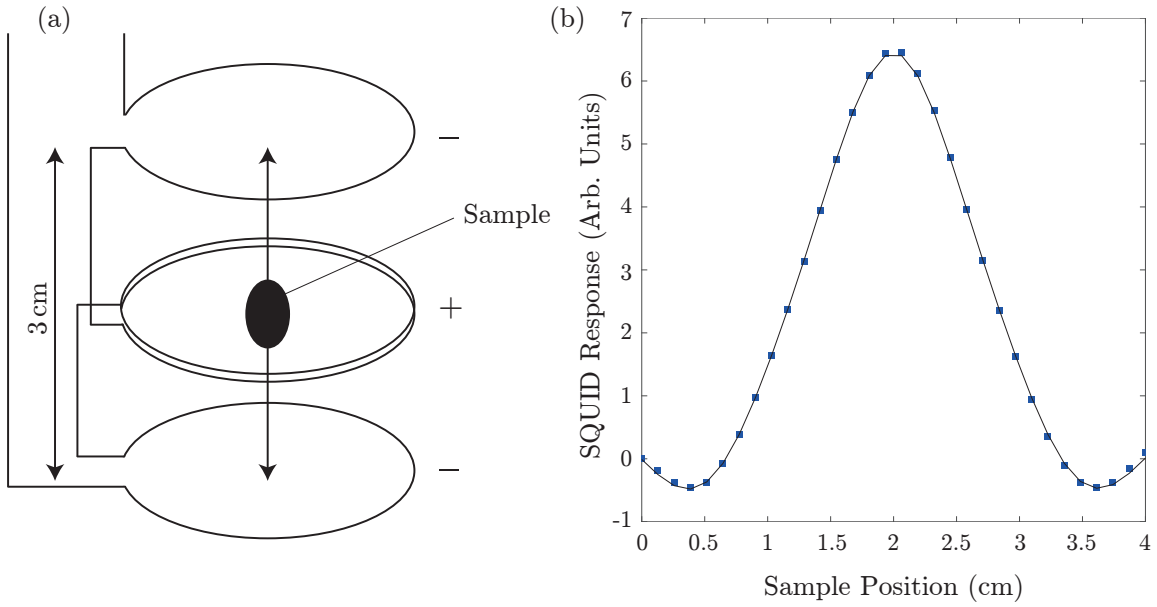

Figure 2.1: (a) Schematic of the coil set of the Quantum Design SQUID magnetometer used in this work. The sample is driven vertically through the coils as marked. A VSM is similar except there is only one coil and the sample is vibrated vertically about the centre of the coil. (b) Sample data showing the SQUID response as the sample is driven vertically through the coils (blue squares) and the fitted response function (black line) whose magnitude determines the measured sample moment.

plastic straw, with the plastic containing no magnetic impurities and giving only a small diamagnetic background which is close to constant along the length of the straw. A background subtraction using a measurement of an empty straw and capsule is possible, however this was never necessary in the present work since the sample responses were always much larger than the background.

The sample straw is attached to the end of a probe and lowered into a ^{4}He cryostat, which is itself located inside the bore of a superconducting high field magnet. By pumping on the ^{4}He in the sample space it is possible attain a base temperature of 1.8 K, and when combined with a heater and calibrated thermometer in the sample space any stable temperature between 1.8 and 300 K can be achieved. The superconducting magnets have maximum fields of 7 T (SQUID magnetometer) and 16T (VSM).

In the SQUID magnetometer, three measurement coils are wound around the sample space in the $-+-$ configuration shown in Fig. 2.1 (a), with the $-$ polarity coils consisting of a single turn and the $+$ coil two turns. The sample is then driven vertically through the coils and the voltage across the whole coil set monitored, resulting in a response

similar to that plotted in Fig. 2.1 (b) as a function of straw position due to the time-varying magnetic flux through the coils as the sample moves. This response is then fitted to the predicted response function, with the magnitude of the fit parameters yielding the sample's magnetic moment. The moments obtained from a few such scans at a given temperature and magnetic field are averaged to reduce noise, meaning the measurement time for a single data point is typically about 1 minute.

In the VSM the sample is located in the centre of a pickup coil and the sample vibrated up and down at a constant frequency $f = 40\,\mathrm{Hz}$. The time-varying voltage in the coil V_{coil} is measured and all components at frequencies other than the sample vibration frequency filtered out. This voltage is given by

$$V_{\mathrm{coil}} = \frac{d\Phi}{dt} = \left(\frac{d\Phi}{dz}\right)\left(\frac{dz}{dt}\right) \tag{2.1}$$

where Φ is the flux through the coil and z is the vertical position of the sample. Since z varies sinusoidally,

$$\begin{aligned} z &= A\sin(2\pi f t) \\ V_{\mathrm{coil}} &= 2\pi f C m A\cos(2\pi f t) \end{aligned} \tag{2.2}$$

where C is a constant and m is the sample's magnetic moment [46]. This means that the magnitude of the voltage response at the vibration frequency can be easily converted to the sample moment. A VSM measurement is continuous with a much shorter measuring time than the SQUID magnetometer, allowing much more data to be obtained.

For either type of magnetometer, M v. H curves are taken simply by sweeping the magnetic field, usually in a complete loop $0 \to +H \to -H \to +H$ to detect any hysteresis. If the magnetic susceptibility is needed a low-field measurement, typically at $H = 1000\,\mathrm{Oe}$,[1] can be used provided the magnetisation is expected to be linear in H up to the measurement field. Susceptibility and magnetisation data are usually normalised

[1] Oersted (Oe) is the unit of magnetic field H in the 'CGS' (centimetre-gram-second) system which is commonly used in magnetometers like the MPMS and PPMS. The conversion is $1\,\mathrm{Oe} = \frac{1000}{4\pi}\,\mathrm{A\,m^{-1}} = 79.577\,\mathrm{A\,m^{-1}}$. The CGS unit for magnetic flux density B is Gauss, with conversion $1\,\mathrm{T} = 10000\,\mathrm{G}$.

either per mole (χ_{mol}) or per unit volume (χ_{v}).

2.1.2 AC Magnetisation

If the sample is placed in the coil centre of a magnetometer and a time-varying, sinusoidal magnetic field applied it is possible to probe the AC magnetic susceptibility over a wide range of frequencies. In this thesis I have performed AC magnetisation measurements in a SQUID magnetometer which can access frequencies between 0.1 Hz and 1 kHz. The measurement is performed via a 'two-point' method. This entails performing two measurements, one with the sample positioned in the bottom, negatively-wound coil and the other with it in the middle, positively wound coils of the SQUID magnetometer (Fig. 2.1). During the first measurement the magnetometer applies a 'nulling' signal to the SQUID coils, with the aim of exactly cancelling out the sample response and obtaining zero current through the coils. After refining the nulling waveform down to a predetermined precision, the magnetometer moves on to the second part of the measurement with the sample in the middle coil, during which it continues to apply the nulling waveform to the coils. By doing this any background signal which is independent of the sample is cancelled out. Since the middle coil has twice as many turns and is wound in the opposite direction compared to the bottom coil, a sample response will be observed in the second measurement which is three times what the response due to a single coil would have been. This combination of enhanced sample response and efficient background cancellation allows for very high-precision measurement of the sample magnetisation.

The measurement is performed over a small number of complete cycles of the AC applied field and the time dependence of the observed response after the nulling procedure is fitted to a sine wave at the measurement frequency plus constant and H–linear background terms. By examining the magnitude of the fitted waveform and its phase relative to the applied field the real (m') and imaginary (m'') parts of the magnetisation can be obtained. As with DC measurements, the moment is typically normalised per mole or per unit volume, and the susceptibilities χ' and χ'' can be obtained by normalising to

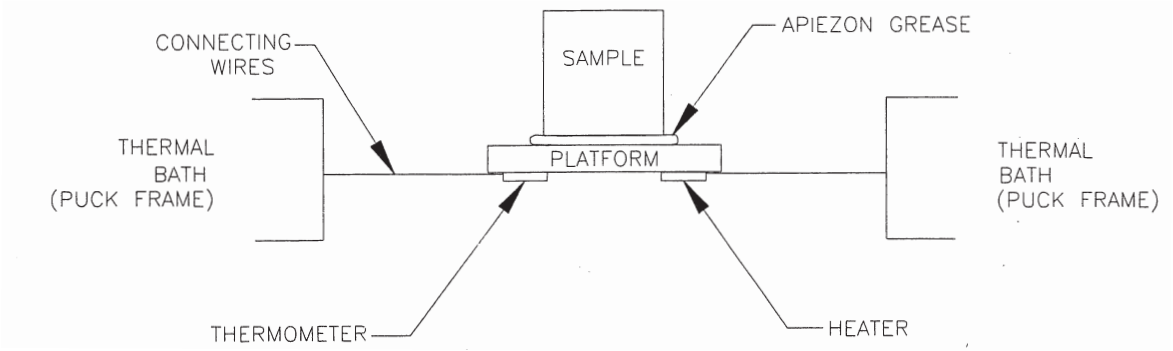

Figure 2.2: Schematic of the thermal connections between the sample, platform and puck (thermal bath) in the PPMS Heat Capacity measurement system used in this work.

the amplitude of the measurement field (typically around 4 Oe).

2.2 Specific Heat

The heat capacity of a sample at constant pressure $C_P = \left(\frac{dQ}{dT}\right)_P$ is a useful probe of the low-lying excitations of the system being studied and can sometimes reveal low-lying modes which other techniques are not sensitive to.

Specific heat measurements in this thesis were performed using the Heat Capacity option on a Quantum Design Physical Property Measuring System (PPMS) [47]. In this instrument the sample is bonded to an epoxy platform using grease, with a heater and thermometer mounted on the underside of the platform (Fig. 2.2). The platform is connected to a thermal bath (in this case, a metal puck) via thin constantan connecting wires and the whole setup is placed under high vacuum so that thermal contact between the puck and platform is dominated by these wires. The puck is in thermal contact with a ^{4}He cryostat to allow temperature control between room temperature and 2 K, and surrounded by a superconducting magnet which can provide magnetic fields up to 11 T.

Once the system has reached thermal equilibrium at the temperature of interest a small, known amount of heat is applied to the platform by the heater over a short period of time, and the temperature at the thermometer on the sample platform is monitored as the heat is lost from the sample through the platform to the bath. If there is good thermal contact between the sample and platform, a simple exponential decay of temperature is seen after the heater is switched off, whereas if the contact is poor the decay is usually

well approximated by the sum of two exponentials, one due to heat flowing from the sample to the platform and one due to heat flowing from the platform to the bath. In either case the combined heat capacity of the sample, platform and grease can then be determined by fitting the decay of the temperature measured by the thermometer, given the known thermal conductivity of the wires between the platform and the puck. In most cases it is also necessary to perform a background measurement of the heat capacity of the puck and grease without the sample and subtract this from the data to obtain the sample heat capacity. Further details of the measurement and fitting procedure can be found in Ref. [47].

In most condensed matter systems we are primarily interested in the low-temperature heat capacity. This will always contain contributions from the lattice, which are typically fitted to the Debye model ($C = \alpha T^3$ where α is a constant) [6] and for metals a contribution due to the conduction electrons, which is usually fitted using the Sommerfeld model ($C = \gamma T$) [1]. The Sommerfeld coefficient γ is related to the density of states at the Fermi surface and can therefore be compared to other measurements of electronic band structure to check if all Fermi surface sheets have been observed [48]. If only these two contributions are present ($C = \alpha T^3 + \gamma T$), a plot of C/T v. T^2 will be linear with y-intercept γ and gradient α.

2.3 Scattering Theory

Scattering of radiation whose wavelength is on the order of the inter-atomic separation, for example x-rays and neutrons, is a very versatile and powerful technique in the study of condensed matter systems. For many decades elastic scattering of these probes has been used for very precise determination of the crystal structure of samples, as well as any ordered magnetic structure in the case of neutron scattering [49]. With more recent developments in instrumentation and the high fluxes available at modern x-ray and neutron sources many higher-order effects can also be usefully studied including inelastic, resonant and polarisation-dependent processes. For example, inelastic neutron

scattering is a powerful probe of low-energy structural and magnetic excitations, while polarisation can be used to experimentally separate scattering due to magnetism from that due to structural phenomena. The much higher energies of x-rays, meanwhile, allow measurement of higher energy excitations, and tuning of the incident x-ray energy to a resonant enhancement can be employed to make the scattering species-dependent.

In this section I shall give a brief overview of the specific scattering techniques I have employed in the work presented in this thesis. A more detailed discussion of the full breath of x-ray and neutron scattering techniques can be found in Refs. [6, 49, 50].

2.4 General Scattering Theory

Fermi's Golden Rule [6] gives the scattering rate per unit time $\Gamma(\mathbf{k}', \mathbf{k})$ for incoming particles with wavevector $\mathbf{k}$ and energy $E_{\mathbf{k}}$ scattering into a state with outgoing wavevector $\mathbf{k}'$ and energy $E_{\mathbf{k}'}$:

$$\Gamma(\mathbf{k}', \mathbf{k}) = \frac{2\pi}{\hbar} |\langle \mathbf{k}' | V | \mathbf{k} \rangle|^2 \delta(E_{\mathbf{k}'} - E_{\mathbf{k}}). \tag{2.3}$$

The matrix element

$$\langle \mathbf{k}' | V | \mathbf{k} \rangle = \frac{1}{L^3} \int \mathrm{d}\mathbf{r} e^{-i(\mathbf{k}'-\mathbf{k})\cdot\mathbf{r}} V(\mathbf{r}) \tag{2.4}$$

is the component of the Fourier transform of the scattering potential $V(\mathbf{r})$ at momentum transfer $\mathbf{Q} = \mathbf{k}' - \mathbf{k}$, while the δ-function ensures elastic scattering.

In a crystal with a periodic potential $V(\mathbf{r}) = \sum_{\mathbf{R}} V_{\mathrm{uc}}(\mathbf{R} + \mathbf{r})$, we can split the matrix element into two factors

$$\langle \mathbf{k}' | V | \mathbf{k} \rangle = \frac{1}{L^3} \Big[\sum_{\mathbf{R}} e^{-i(\mathbf{k}'-\mathbf{k})\cdot\mathbf{R}} \Big] \Big[\int_{\mathrm{uc}} \mathrm{d}\mathbf{x} e^{-i(\mathbf{k}'-\mathbf{k})\cdot\mathbf{x}} V_{\mathrm{uc}}(\mathbf{x}) \Big] \tag{2.5}$$

where $V_{\mathrm{uc}}(\mathbf{x})$ is the potential due to one unit cell centred at $\mathbf{x} = \mathbf{0}$ and $\{\mathbf{R}\}$ are the real lattice vectors.

The first factor in equation 2.5 is zero unless the momentum transfer is equal to a

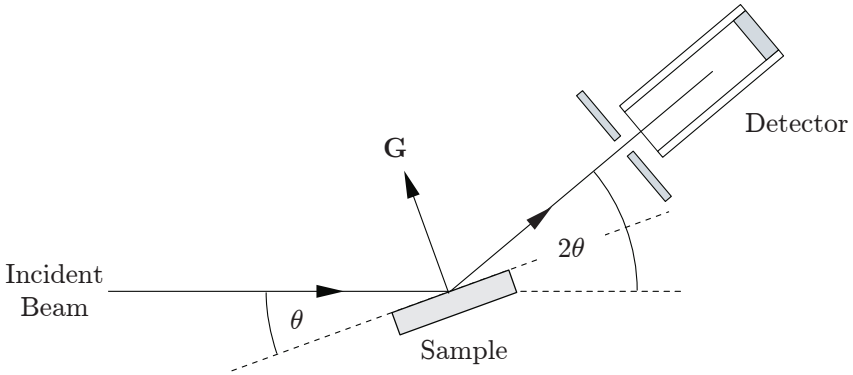

Figure 2.3: Experimental geometry of an elastic scattering experiment. 2θ is the scattering angle and $\mathbf{G}$ is the reciprocal lattice vector corresponding to the lattice planes which the beam diffracts off in this geometry. Figure adapted from Ref. [51].

reciprocal lattice vector, i.e. $\mathbf{Q} = \mathbf{k}' - \mathbf{k} = \mathbf{G}$ where $e^{i\mathbf{R}\cdot\mathbf{G}} = 1$ for all $\mathbf{R}$ on the real lattice and $\mathbf{G}$ on the reciprocal lattice. This condition can be fulfilled by defining the reciprocal lattice in terms of the real lattice vectors $\mathbf{a}$, $\mathbf{b}$ and $\mathbf{c}$ via the general relations

$$\begin{gathered}\mathbf{a}^* = 2\pi\frac{\mathbf{b}\times\mathbf{c}}{\mathbf{a}\cdot\mathbf{b}\times\mathbf{c}},\ \mathbf{b}^* = 2\pi\frac{\mathbf{c}\times\mathbf{a}}{\mathbf{a}\cdot\mathbf{b}\times\mathbf{c}},\ \mathbf{c}^* = 2\pi\frac{\mathbf{a}\times\mathbf{b}}{\mathbf{a}\cdot\mathbf{b}\times\mathbf{c}} \\ \mathbf{G} = h\mathbf{a}^* + k\mathbf{b}^* + l\mathbf{c}^*\end{gathered} \tag{2.6}$$

for (h, k, l) integers.

For every $\mathbf{G}$ on the reciprocal lattice there is a corresponding set of lattice planes, i.e. a set parallel planes which contains all of the lattice points, which are normal to $\mathbf{G}$ and have separation ('d-spacing') $d_{hkl} = 2\pi/|\mathbf{G}|$. It can be shown that scattering with momentum transfer $\mathbf{Q} = \mathbf{G}$ is equivalent to diffraction off the set of lattice planes with Miller indices (hkl) [6].

A typical experimental arrangement for measuring diffraction (elastic scattering) off a set of lattice planes in a crystal using a monochromatic source with wavelength λ is shown in Fig. 2.3. The incoming and outgoing radiation in such an experiment must be at the same angle θ to the sample surface, with 2θ often referred to as the scattering angle. It can be shown that the Laue condition $\mathbf{G} = \mathbf{k}' - \mathbf{k}$ in this geometry implies that

$$\lambda = 2d_{hkl}\sin\theta \tag{2.7}$$

which is the famous Bragg's law. Since d_{hkl} is determined by the real lattice vectors, the locations of peaks in elastic scattering intensity ('Bragg peaks') can be used to determine the lattice type and lattice parameters in a sample.

The remaining factor in equation 2.5 is the structure factor, $S(\mathbf{G})$

$$\begin{aligned} S(\mathbf{G}) &= \int_{\text{uc}} \mathrm{d}\mathbf{x} e^{-i\mathbf{G}\cdot\mathbf{x}} V_{\text{uc}}(\mathbf{x}) = \sum_d f_d e^{i\mathbf{G}\cdot\mathbf{x}_d} \\ f_d(\mathbf{G}) &= \int \mathrm{d}\mathbf{x}_d e^{-i\mathbf{G}\cdot\mathbf{x}_d} V_d(\mathbf{x}_d) \end{aligned} \tag{2.8}$$

where f_d is the form factor due to atom d in the unit cell and we have used the fact that the potential is the sum of potentials due to individual atoms

$$V_{\text{uc}}(\mathbf{x}) = \sum_d V_d(\mathbf{x} - \mathbf{x}_d) \tag{2.9}$$

and $V_d(\mathbf{x}_d)$ is the potential due to an atom d situated at $\mathbf{x}_d = \mathbf{0}$. The structure factor is the Fourier transform of the *basis*, i.e. the contents of the unit cell, and determines the relative intensities of reflections at different (hkl). Information about Bragg peak intensities can therefore be used to examine the ionic species and their positions within the unit cell. This kind of experiment is complicated somewhat, however, by the fact that observed intensity is determined by $|S(\mathbf{G})|^2$ and is therefore missing information about the relative phases of structure factors at the different Bragg peaks - the 'phase problem'. There is no general way to get around this in first-principles crystal structure solution, so in reality a combination of methods mostly involving some degree of prior knowledge or expectation of the likely structure is used.

The precise Q-dependence of the atomic form factors for different probes will be discussed in the relevant sections below.

2.5 X-ray Scattering

X-rays are photons in the energy range of approximately 100 eV–100 keV. This is often split further into 'soft' x-rays below around 5 keV and 'hard' x-rays above this energy.

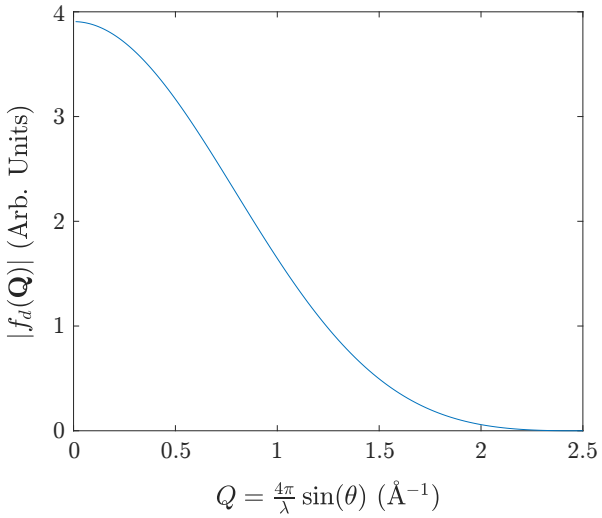

Figure 2.4: The typical Q-dependence of the x-ray atomic form factor for an atom of width ~ 1 Å.

They provide a very powerful probe due to the large range of wavelengths and energies accessible as well as very high fluxes available at modern x-ray sources. They do also have some weaknesses; for example, the x-ray form factor for an ion (Fig. 2.4) is proportional to the charge on the ion, so they are not very sensitive to small atoms (and almost totally insensitive to hydrogen ions) and even amongst heavier elements it is difficult to distinguish between ions with similar atomic number.

X-ray diffraction measurements on single crystals and powders are a routine sample characterisation technique used throughout the work presented in this thesis. It is usually relatively easy to index the observed peaks in such a diffraction pattern with (hkl) values, yielding the unit cell and lattice parameters, while other features such as the presence of any unindexed peaks and powder rings and the width, shape and any smearing of the Bragg peaks allow for assessment of the sample quality and impurity content. This information alone is often sufficient for sample characterisation purposes, however for high quality samples it is sometimes also possible to partially solve or refine the structure within the unit cell based on the peak intensities, as demonstrated in Chapter 4. All of the lab-based x-ray diffraction which I performed in this work employed an Oxford Instruments Supernova Diffractometer.

It is also possible to perform a range of x-ray scattering measurements at synchrotron

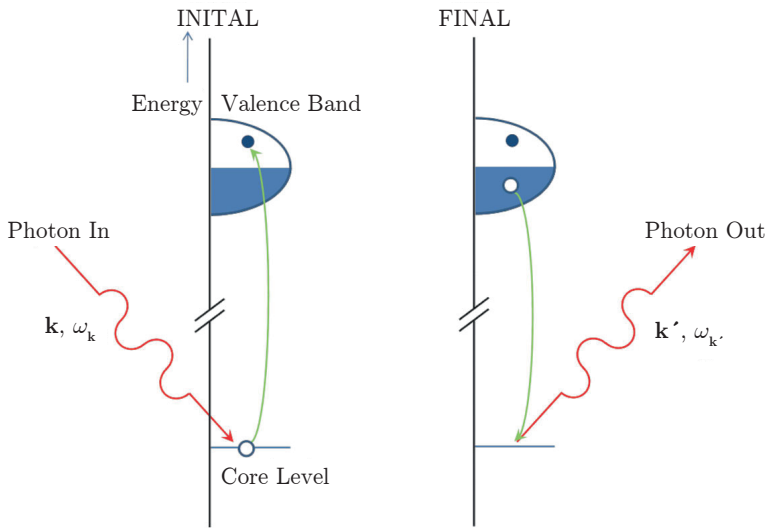

Figure 2.5: Schematic of the dominant, direct RIXS process. Figure reproduced from Ref. [52].

facilities such as Diamond Light Source at Harwell, U.K. and the European Synchrotron Radiation Facility (ESRF) in Grenoble, France. These sources provide a massively increased flux compared to lab-based diffractometers, allowing observation of much lower intensity features of the spectrum, assuming radiation damage and heating of the sample can be avoided. Chapter 4 presents an example of the observation of weak superstructure on the beamline I19 of the Diamond Light Source which allowed for the determination of a small crystalline distortion in the material studied.

2.5.1 Resonant Inelastic X-Ray Scattering

As synchrotron x-ray fluxes increase and instrumentation develops it has become possible to measure a range of useful resonant and inelastic phenomena. I present results from one such technique in this thesis - Resonant Inelastic X-Ray Scattering (RIXS), illustrated in Fig. 2.5. The dominant, 'direct' RIXS process involves tuning the incident photon energy to match the energy difference between a core electron shell (for example the $2p$ shell) and the excited level of interest (for example, some magnetic excitation in a part-filled $5d$ shell). The photon is absorbed in a dipolar process, promoting a core electron to the excited level and forming an intermediate state with a core hole. The intermediate state is very unstable and short-lived and has a range of possible decay routes. The significant one for direct RIXS is the decay of one of the other $5d$ electrons to fill the

core hole via another dipolar process which emits another x-ray photon. The net effect of this process is to create a particle-hole excitation in the $5d$ shell, with the energy and momentum transferred from the photon. The difference in energy and momentum between the incident and outgoing photons is then used to determine the excitation's energy and momentum above the ground state.

By varying the incident x-ray energy it is possible to see a range of different excited levels resonate, building up a full excitation spectrum. Since the incident energy is tuned to match a resonance on one specific ionic species in the sample, this is a highly targeted measurement of the single-ion excitations on that species.

RIXS is a versatile probe of single-ion excitations with the potential to observe charge, orbital and magnetic excitations. The excitation and decay processes from the core state are both subject to a dipolar matrix element, however, which means RIXS can be either forbidden or very weak for certain excited states which have small or zero matrix elements. It is a second-order process and is correspondingly weak compared, for example, to elastic scattering, even when the enhancement due to resonance is taken into account. The energy transfer is also very small ($\lesssim$ a few eV) compared to the photon energies ($\sim$ keV), so very high energy resolution as well as very high statistics are required.

In order to optimise resolution and signal, RIXS measurements are usually performed with the detector at right angles to the incident beam ($2\theta = 90^{\text{o}}$) since the polarisation factor ensures elastic scattering processes have zero intensity at this angle, and with a relatively long sample-to-detector distance $\sim 1\,\text{m}$. With modern instrumentation, it is now possible to measure excitations via RIXS with energy resolution down to a few tens of meV.

The RIXS measurements presented in this thesis (Chapter 5) were performed on the beamline ID20 at the ESRF [53]. A comprehensive review of the many aspects of the RIXS method which I do not touch on in this thesis can be found in Ref. [52].

2.6 Neutron Scattering

Neutron spectroscopy is a very powerful technique for probing condensed matter systems [49, 50]. 'Thermal' neutrons, i.e. neutrons with energies close to 0.025 eV ($= k_{\mathrm{B}} \times 290\,\mathrm{K}$), have wavelengths similar to the separation of atoms in crystals and interact directly with the nuclei via the strong nuclear force. Since nuclei are small compared to the neutron wavelength the interaction potential is very well approximated by a δ-function at the nucleus, resulting in atomic form factors which are Q-independent. The form factor is usually expressed in terms of a 'scattering length'

$$f_d(\mathbf{Q}) = b_d \tag{2.10}$$

where b_d is the scattering length of nucleus d, which may be complex.

The neutron has a spin $s = 1/2$ and resulting magnetic moment $|\mu_{\mathrm{n}}| = 1.9\,\mu_{\mathrm{N}}$ where μ_{N} is the nuclear magneton. This means that the neutron can also couple to the nucleus via a magnetic interaction with the nuclear spin I, modifying the coupling compared to that from the strong force alone. Since the nuclear spins tend to point in random directions, this leads to a random distribution of scattering lengths on the nuclei in sample. An additional random component comes from the fact that most elements naturally occur as a mixture of different isotopes which will have different scattering lengths, although this component can sometimes be removed by growing samples using isotopically pure starting materials.

In order to accommodate this disorder, neutron scattering is split into coherent and incoherent processes. The coherent scattering is the scattering pattern which would be seen if all nuclei had the same, average scattering length

$$b_{\mathrm{coh}} = \langle b_i \rangle \tag{2.11}$$

where the average is over all sites i in the sample, while incoherent scattering is any extra scattering due to deviations from this average characterised using the incoherent

scattering length

$$b_{\text{inc}} = \sqrt{\langle b_i \rangle^2 - \langle b_i^2 \rangle}. \tag{2.12}$$

Incoherent scattering therefore contains nuclear spin incoherent scattering as discussed above as well as contributions due isotopic disorder

In most cases the coherent scattering channel is dominant and contains nuclear Bragg peaks as expected under general scattering theory. The values of the scattering lengths are governed by the details of the strong interaction and vary unpredictably across the periodic table. This means that, unlike for x-rays, atoms with similar charge Z can be easily distinguished via the intensities of Bragg peaks in coherent neutron scattering. Neutron diffraction patterns are also much more sensitive than x-rays to light elements.

Nuclear spin- and isotope-incoherent scattering is usually completely flat as a function of Q and in unpolarised neutron scattering is typically fitted as part of the background. For most elements this does not present a significant problem, however in a few well-known cases where one of the components of the incoherent scattering is strong or the coherent scattering length is very small the incoherent scattering background can significantly reduce the statistics of the coherent channel or even mask it altogether. Notable examples are natural Vanadium, which has almost zero coherent scattering length, and ^{1}H, which has a very large nuclear spin incoherent scattering length. In such cases, isotopically enriched samples are used to get around the problem; I present one such example in Chapter 3 where I use a deuterated sample (D = ^{2}H) to avoid the strong incoherent scattering which would come from natural hydrogen.

In addition to nuclear scattering the neutron can interact with electron spins and angular momenta in the sample via its magnetic moment. It is therefore a very powerful direct probe of magnetic effects including short- and long-range magnetic order, since these will cause extra scattering to appear as the order develops. Long range order can lead to extra Bragg peaks appearing in the spectrum which are not allowed for the nuclear scattering alone or to changes in the intensity of the nuclear Bragg peaks, while

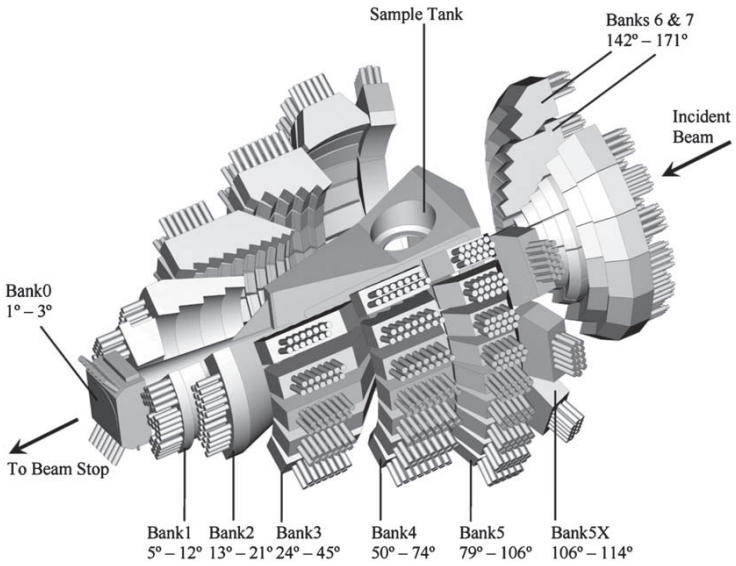

Figure 2.6: Schematic of the GEM beamline at ISIS, a typical instrument used for elastic neutron diffraction and sample characterisation. Figure reproduced from Ref. [54].

short range correlations lead to broader areas of extra scattering appearing around the Q corresponding to the typical length scale of the correlations. Magnetic scattering is, however, subject to a magnetic form factor $f_{\text{mag}}(\mathbf{Q})$ which is strongest at low Q and which contains a factor of $\mathbf{Q} \times \mathbf{M} \times \mathbf{Q}$. This factor is the projection of $\mathbf{M}$ onto the plane perpendicular to $\mathbf{Q}$, so only components of the sample magnetisation perpendicular to $\mathbf{Q}$ are probed.

In practice, elastic neutron scattering is often measured in a spectrometer similar to that pictured on Fig 2.6. The sample is mounted inside a cryostat in the neutron beam and surrounded by detectors covering as much of the available solid angle as possible, in order to probe as much of Q space as possible. A single incident neutron energy is selected by two choppers, which consist of two disks of neutron-absorbing material with slits in them which rotate at a variable angular frequency. Since a neutron's velocity depends on its energy, for a given angular frequency only neutrons with one particular energy will pass through both slits and reach the sample. This is the commonly referred to as the 'time-of-flight' (TOF) method.

2.6.1 Polarised Neutron Scattering

If a polarised beam of neutrons is used and the polarisation of diffracted neutrons measured, it is possible to separate most of the different coherent, incoherent and magnetic cross-sections. The equations for the so-called xyz-method are

$$\begin{aligned}\left(\frac{d\sigma}{d\Omega}\right)_{\text{nuc}} &= \frac{1}{6}\left[2\left(\frac{d\sigma}{d\Omega}\right)_{\text{Tnsf}} - \left(\frac{d\sigma}{d\Omega}\right)_{\text{Tsf}}\right] \\ \left(\frac{d\sigma}{d\Omega}\right)_{\text{si}} &= \frac{1}{2}\left(\frac{d\sigma}{d\Omega}\right)_{\text{Tsf}} - \left(\frac{d\sigma}{d\Omega}\right)_{\text{mag}} \\ \left(\frac{d\sigma}{d\Omega}\right)_{\text{mag}} &= 2\left(\frac{d\sigma}{d\Omega}\right)^{x}_{\text{sf}} + 2\left(\frac{d\sigma}{d\Omega}\right)^{y}_{\text{sf}} - 4\left(\frac{d\sigma}{d\Omega}\right)^{z}_{\text{sf}}\end{aligned} \tag{2.13}$$

where $\frac{d\sigma}{d\Omega}$ are differential cross sections and 'nuc', 'si' and 'mag' refer to the nuclear, spin-incoherent and magnetic cross-sections [55]. x, y and z refer to the direction of the neutron polarisation axis relative to a Cartesian coordinate system and 'sf' and 'nsf' mean the spin-flip and non-spin-flip cross sections along the relevant axis. 'Tsf' and 'Tnsf' mean the total (non-)spin-flip cross sections summed over all three directions x, y, z.

If a '6-point' measurement is performed, i.e. subsequent measurements of the spin-flip and non-spin-flip cross sections for beam polarised parallel to each of x, y and z in turn, then these equations can be used to extract the desired magnetic, nuclear and spin-incoherent cross sections.

Polarised neutron scattering is a very powerful technique for probing magnetic scattering since the strong nuclear contributions to the spectrum can be effectively removed. It can also be used as way to remove the spin-incoherent background in order to study nuclear scattering in samples containing atoms like ^{1}H which have a large spin-incoherent cross-section.

Polarised neutron spectrometers typically have a similar geometry to unpolarised spectrometers, except the polariser and analyser mirrors are chosen to only reflect one of the two spin species (Fig. 2.7). The whole beam path is in a small magnetic field with variable direction ('guide field') which determines the axis of the neutron polarisation.

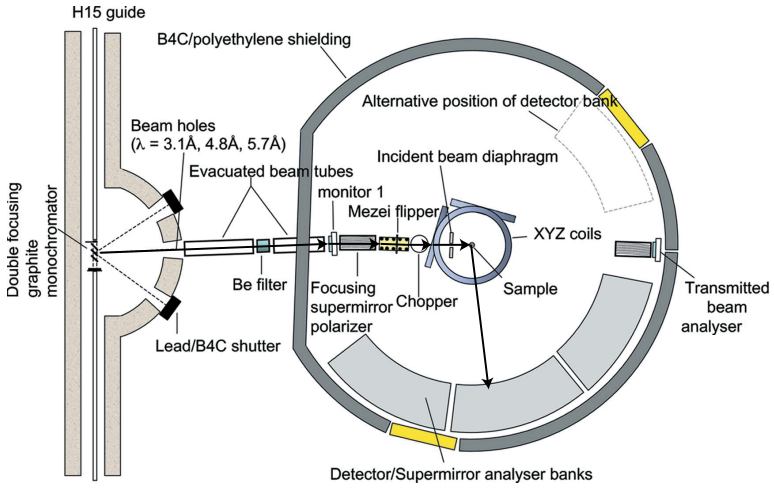

Figure 2.7: Schematic of the D7 beamline at the Institut Laue-Langevin (ILL), the instrument used to perform polarised neutron diffraction in this work. The arrows mark the beam path. Figure reproduced from Ref. [55], where further details on the components of this spectrometer can be found.

A magnetic 'flipper' is placed after the polariser which can invert the polarisation of the incident beam with high efficiency, meaning that changing between spin-flip and non-spin-flip mode simply requires turning the flipper on or off. In order to calibrate background, detector and flipper efficiencies and sample absorption, a range of calibration measurements are performed for each sample including the empty sample can, cadmium (a very strong absorber), quartz (only spin-flip scattering) and vanadium (only incoherent scattering with a known cross-section).

2.6.2 Inelastic Neutron Scattering

Thermal neutron energies and momenta are very similar to those of excitations in condensed matter such as phonons and magnons, making inelastic neutron scattering a useful tool for studying their dispersions. A typical 'triple-axis' spectrometer suitable for unpolarised neutron scattering is pictured in Fig. 2.8. The incident energy can be varied by changing the diffraction angle at the monochromator and the outgoing energy using the angle at the analyser, while the momentum transfer is determined by the scattering angle at the sample. Another common design is the time-of-flight (TOF) spectrometer, shown in Fig. 2.9. In this case, choppers select the incident energy while the time of flight and beam path length can be used to determine the outgoing neutron

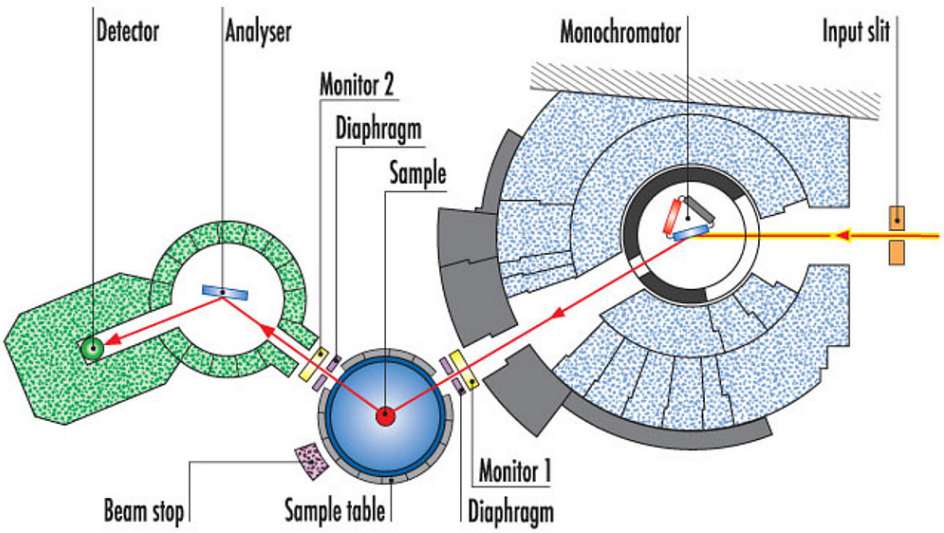

Figure 2.8: Diagram of the IN8 instrument at the ILL, a typical triple axis spectrometer used for inelastic neutron scattering. Figure reproduced from Ref. [56].

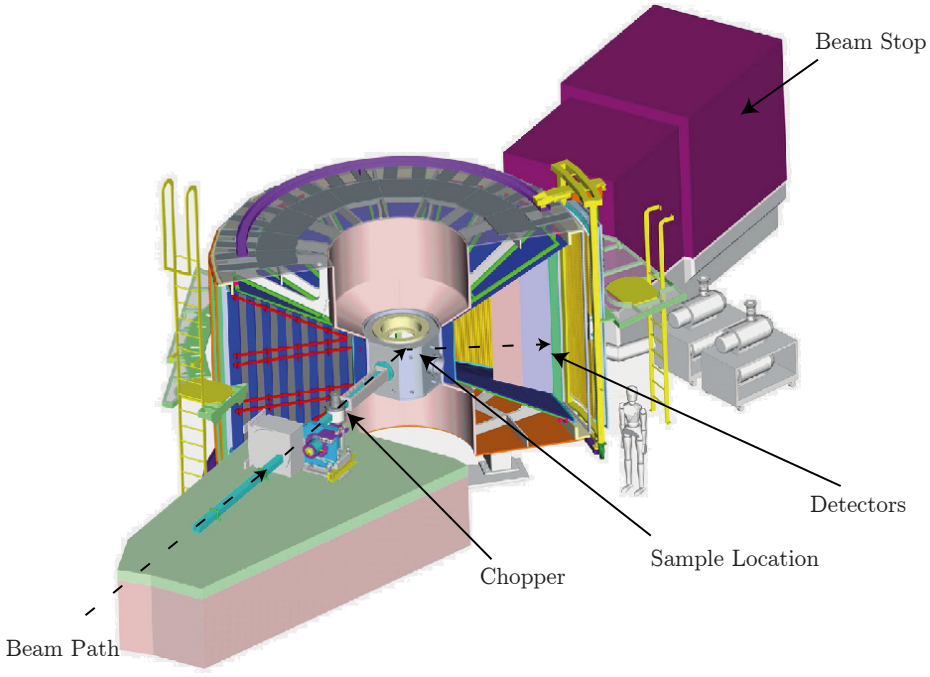

Figure 2.9: Diagram of the Merlin spectrometer at the ISIS facility [57], a typical time-of-flight spectrometer used for inelastic neutron scattering. Figure reproduced from Ref. [58].

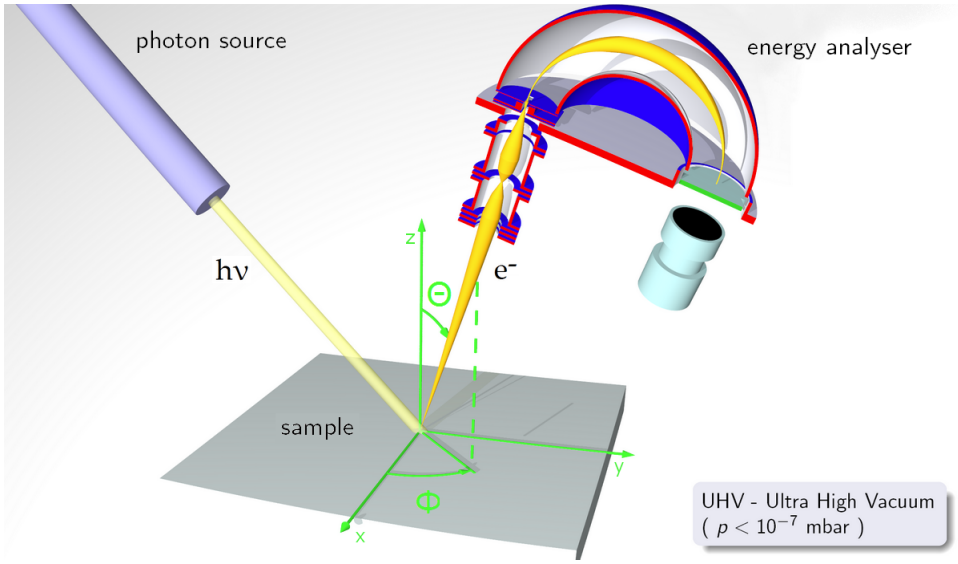

Figure 2.10: Schematic of the ARPES technique. Figure reproduced from Ref. [59].

energy, since higher energy neutrons have higher velocity. The diffraction angle at the sample again determines the momentum transfer, and a large bank of detectors can be used to cover a large range of Q simultaneously [57].

The inelastic neutron scattering spectrum is proportional to the dynamical structure factor $S(\mathbf{Q}, \omega)$ as well as a form factor for the relevant type of scattering. This means that the dispersions of excitations can be directly measured, assuming the neutron couples to them. A typical spectrum will contain phonon scattering at high Q and magnetic modes or diffuse scattering at low Q (if present), allowing these two types of excitation to be distinguished with care by examining the relevant parts of the spectrum and possibly their temperature dependence. An example of a measurement of magnetic excitations using a TOF spectrometer can be found in Chapter 3.

2.7 Angle Resolved Photoemission Spectroscopy (ARPES)

Angle Resolved Photoemission Spectroscopy (ARPES) is powerful technique for measuring electron band dispersions in crystals. It involves exposing the sample to soft x-rays at a known energy which are absorbed by electrons at the surface of the material. If the x-ray energy is larger than the binding energy of the electron, it will escape the sample.

A detector is positioned above the sample at a variable angle which contains an energy analyser capable of measuring the outgoing electron flux as a function of energy. Using conservation of energy and momentum, it is possible to reconstruct the electron's original energy and momentum in the sample before it was ejected from the detector angle and incident x-ray and outgoing electron energies. A detailed discussion of how this is achieved can be found in Refs. [1, 60] and a diagram of a typical ARPES instrument is shown in Fig. 2.10.

The ARPES technique is by its nature only sensitive to the sample surface and has limited k_z resolution. It is therefore best-suited to quasi-2D layered systems. There is also an ARPES matrix element, meaning that certain electron bands may be weak or absent in ARPES due to their symmetry or orbital character. An example of the use of ARPES to study changes in the electronic structure of a quasi-2D system can be found in Chapter 3.

2.8 Muon Spin Rotation/Relaxation (μSR)

μSR is unique among the techniques discussed here since it is an implantation probe which involves allowing positive or negative muons (μ^+/μ^-) to stop in the sample and interact with the internal, microscopic environment before monitoring their decay products.

Muons for such an experiment are typically produced at spallation sources, for example the ISIS Neutron and Muon Source, by bombarding a target (made from graphite at ISIS) with high-energy protons. A small proportion of the protons interact with nucleii in the target, producing positive and negative pions

$$\begin{aligned} p + p &\rightarrow p + n + \pi^+ \\ p + n &\rightarrow p + p + \pi^- \end{aligned} \tag{2.14}$$

which then decay very quickly (mean lifetime = 26 ns) into muons

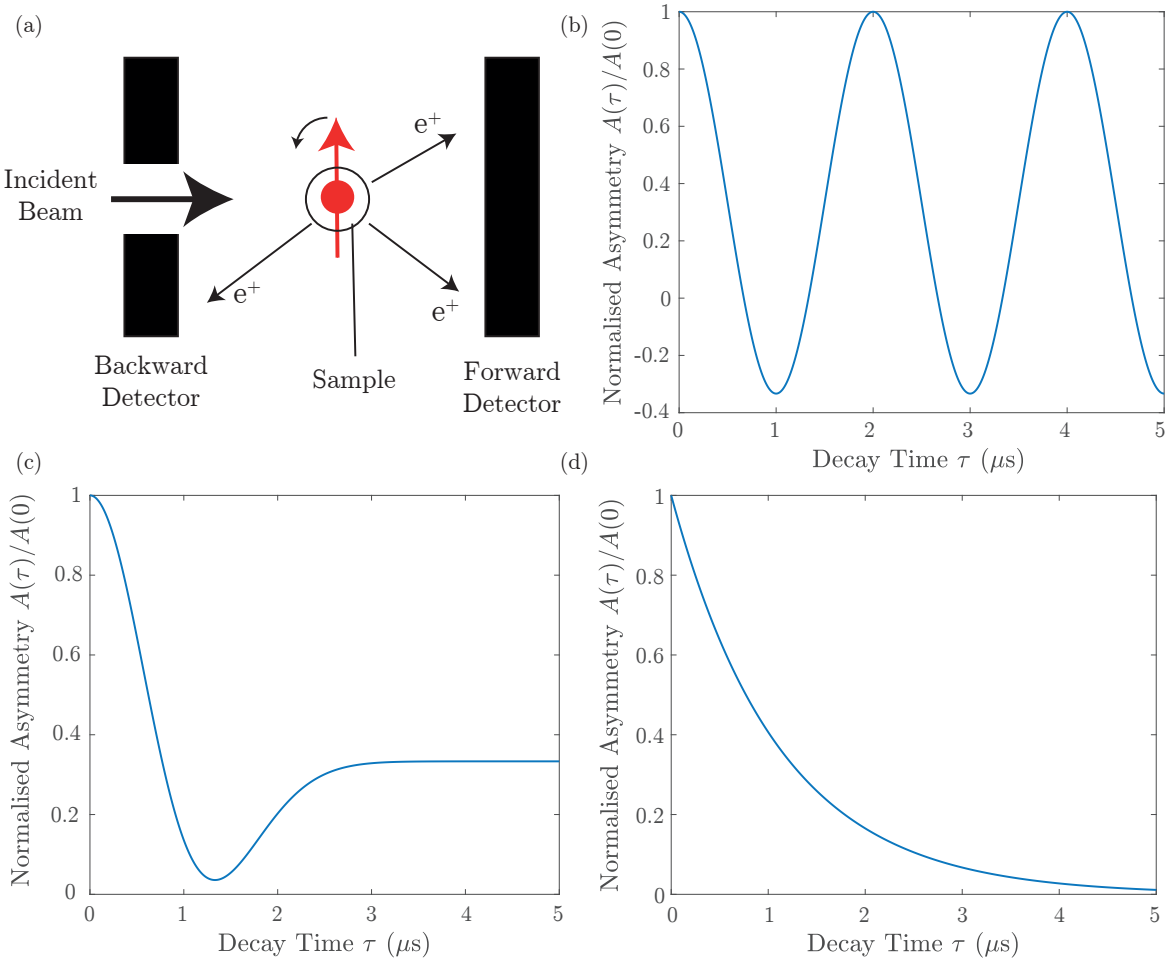

Figure 2.11: (a) Geometry of a typical zero-field μSR measurement. (b) Theoretical asymmetry due to the same, constant magnetic field at all of the muon stopping sites. (c) Theoretical response due to a random distribution of static magnetic fields at the muon stopping sites (the 'Kubo-Toyabe' function [61]). (d) Theoretical response due to an oscillating magnetic field at the muon stopping sites with a single characteristic timescale.

$$\pi^{\pm} \rightarrow \mu^{\pm} + \nu_{\mu}. \tag{2.15}$$

The muon is a spin-1/2 particle with magnetic moment $0.0048\,\mu_{\mathrm{B}}$ [5]. Due to parity violation in the weak force the muon's spin direction is guaranteed to be antiparallel to its direction of travel after the pion decay, meaning a perfectly spin-polarised beam is naturally produced. A single charge species, usually the positive muon, is then selected and the beam focussed onto the sample using multipole magnets.

The sample is mounted inside a foil packet, usually made of silver. The muons interact electrostatically with the atoms in the foil and sample, slowing down and stopping after travelling through a few millimetres of material. The thickness of the foil is therefore chosen so that as many muons as possible stop in the sample. Inevitably, a small fraction of muons will however stop in the sample environment, leading to a small background signal.

Once it has stopped in the sample, the muon will interact with any internal magnetic field at the muon stopping site via its spin; for example if there is a static magnetic field the muon will precess around that field, or if there is a fluctuating magnetic field the muon spin may be randomly re-oriented.

Usually the presence of the muon does not affect the sample's properties in a noticeable way, however in some cases the muon can influence its environment through its electric charge. This is especially true in materials whose electronic or magnetic properties are highly sensitive to ionic positions, such as in the Pr-containing pyrochlores [62], where the muon causes a distortion of the nearby PrO_8 units and changes the crystal field energy levels on the Pr site. In these situations significant care is required in determining the muon-induced effects, although this is sometimes achievable via in-depth DFT calculations.

Muons are unstable with a half life of $2.2\,\mu$s, decaying into a positron and two neutrinos

$$\mu^+ \rightarrow \nu_\mu + \bar{\nu}_\mathrm{e} + \mathrm{e}^+. \tag{2.16}$$

Parity violation in this decay means that the positron's emission direction is asymmetric and more likely to be parallel to the muon's spin at the time of emission than anti-parallel. More precisely, the average fraction of positrons $N(\theta)/N_0$ emitted at an angle θ to the muon's spin is given by [63]

$$N(\theta) = N_0(1 + \cos(\theta)/3). \tag{2.17}$$

This means that, by observing the emission directions of positrons as a function of time since muon implantation we can reconstruct the muon spin's time evolution while stopped in the sample.

In a μSR experiment the sample is placed between two positron detector banks, in the forward and backward directions with respect to the initial muon beam (Fig. 2.11 (a)). The quantity of interest is then the decay asymmetry A,

$$A(\tau) = \frac{N_\mathrm{F}(\tau) - \alpha N_\mathrm{B}(\tau)}{N_\mathrm{F}(\tau) + \alpha N_\mathrm{B}(\tau)} \tag{2.18}$$

where $N_\mathrm{F}(\tau)$ and $N_\mathrm{B}(\tau)$ are the positron count rates in the forward and backward detectors and α is an instrumental parameter which takes into account different detector efficiencies between the two banks. This asymmetry has a maximum possible value of 1/3 for perfectly polarised muons whose spin does not evolve with time and perfect detectors. In reality, initial asymmetries of 25%–30% are typical.

Some common types of μSR spectra are shown in Fig. 2.11 (b–d). If the muons in the sample all experience the same, static magnetic field their spins will precess about the field in a coherent manner, leading to oscillations in the asymmetry as the spin direction oscillates between the two detector banks (Fig. 2.11 (b)). The period of the oscillations can be used to directly calculate the internal magnetic field experienced by the muon. If there are a few distinct muon stopping environments with different magnetic

fields a superposition of multiple oscillations may be also be seen, with the amplitude of each oscillation being related to the proportion of muons experiencing the corresponding field. This type of oscillatory response makes μSR a very powerful, microscopic probe of ordered magnetic systems, since it is rare for a long-range magnetically ordered system not to show such a response.

In the absence of magnetic order, a random distribution of static fields on microsecond timescales at the muon sites results in 'Kubo-Toyabe' relaxation (Fig. 2.11 (c)) with a single, underdamped oscillation as the muon spins gradually lose coherence and '1/3-tail' [61]. Alternatively, fields which fluctuate on microsecond timescales can cause relaxation similar to that in Fig. 2.11 (d), which may fit to a single exponential (corresponding to a single dominant fluctuation frequency) or the sum of several exponentials. In these disordered situations in-depth modelling of the microscopic behaviour including the spatial distribution of muon stopping sites is often required to obtain quantitative information from the spectrum.

Further details on the μSR technique and its applications can be found in Refs. [63, 64].

Chapter 3

Spin resonance in the iron-based superconductor $\mathbf{Li_{1-}_{x}Fe_{x}ODFe_{1-}_{y}Se}$

In this chapter I present an inelastic neutron scattering study of the recently-synthesised iron-based superconductor (FeSC) $Li_{1-x}Fe_xODFe_{1-y}Se$. This material stands out amongst FeSCs since it bears many similarities to monolayer FeSe which has been shown to exhibit a remarkably high T_c, perhaps as high as 100 K, including almost perfect FeSe layers, a similar electron doping level and highly 2D electronic structure. Additionally, $Li_{1-x}Fe_xODFe_{1-y}Se$ itself has a critical temperature $T_c \simeq 41$ K which is among the highest seen in bulk FeSCs. Understanding the band structure and nature of the superconducting order parameter in $Li_{1-x}Fe_xODFe_{1-y}Se$ therefore promises insight into the mechanism of superconductivity in FeSCs and information on how efforts to increase T_c further might be best directed in future.

A large, deuterated powder sample of $Li_{1-x}Fe_xODFe_{1-y}Se$ with almost no Fe vacancies in the FeSe planes ($y \simeq 0$) and the minimum possible interstitial iron (minimum x) was produced via a novel post-synthetic lithiation procedure. I measured the inelastic neutron scattering spectrum of this sample at a series of temperatures below and just above the superconducting transition, observing a clear excitation with a double-peaked shape appearing on cooling below T_c. The structure of this excitation is remarkably similar to one seen in the superconducting state of the structurally similar FeSe-intercalate

$Li_{0.6}(ND_2)_{0.2}(ND_3)_{0.8}Fe_2Se_2$. Its Q dependence plausibly corresponds to nesting between Fermi surface sheets seen in a previous ARPES study, and its energy and temperature dependence strongly indicate it is a superconducting spin resonance.

When taken in combination with ARPES data and evidence from quasiparticle interference experiments (QPI) that the superconducting gap is nodeless, the Q-dependence of the observed spin resonance places strong constraints on the possible gap symmetries, completely ruling out several candidates including s^{++} symmetry. At the very least this is important information for testing theories of the superconducting mechanism in $Li_{1-x}Fe_xOHFe_{1-y}Se$. Since the electronic structure and doping in $Li_{1-x}Fe_xOHFe_{1-y}Se$ is very similar to that of monolayer FeSe, it is possible that this can also provide valuable insight into the mechanism behind the very high T_c in that system.

The results and analysis in this chapter have been published in Physical Review B **94**, 144503 (2016).

I am grateful to my collaborators on this project including D. Woodruff and Simon Clarke's group in the Chemistry Department at Oxford who grew the samples and took the XRD and Magnetisation characterisation data and M. Rahn and A. T. Boothroyd from my group in Oxford who helped perform the neutron scattering measurements.

3.1 Introduction

Much of the rich phenomenology of the iron-based superconductors, especially those containing FeSe layers, remains unexplained [65–69]. The parent phase β-$Fe_{1+x}Se$ has a relatively low superconducting transition temperature T_c of 8.5 K [70, 71] which can be enhanced in a variety of ways including chemical substitution [65], the application of pressure [72] or the intercalation of alkali metal ions and small molecules [73–80]. Remarkably, superconductivity has been observed in monolayers of FeSe on $SrTiO_3$ with T_c up to 65 K [81], and perhaps as high as $T_c \sim 100$ K [82]. Intercalation significantly lengthens the c-axis of the tetragonal unit cell and appears to increase the isolation of the FeSe layers, mimicking the 2D electronic and physical environment of monolayer

FeSe in bulk materials [32]. This suggests that bulk superconductivity at similarly high temperatures might be achievable in derivatives of FeSe that have been tuned to optimal carrier doping and inter-layer separation via chemical intercalation.

Intercalation of alkali ions to form compounds with bulk compositions close to $A_{0.8}Fe_{1.6}Se$ (A = K, Rb, Cs) has been reported to increase T_c up to 45 K [73–76]. The product, however, is inhomogeneous with a majority non-superconducting phase containing iron vacancies and superconductivity in a minority phase [83, 84]. An alternative route is to synthesize intercalates of FeSe at room temperature or below from solutions of electropositive metal ions in ammonia [77–80]. This method can yield single-phase material with vacancy-free FeSe layers and a controllable electronic doping level due to variable amounts of intercalated metal ions and ammonia.

In addition to the ammonia intercalates, a LiOH-intercalate $Li_{1-x}Fe_xOHFe_{1-y}Se$ was recently synthesised and is a bulk superconductor with T_c in excess of 40 K [85–87]. This material was initially synthesized by a hydrothermal route which was subsequently adapted to include a post-synthetic lithiation step, resulting in almost vacancy-free FeSe layers [88]. Investigations throughout the stable composition range ($x \simeq 0.2$, $0.02 < y < 0.15$) found the highest T_c values when the iron vacancy concentration is low ($y < 0.05$), corresponding to significant electron doping of the FeSe layers [88]. Consistent with this, angle-resolved photoemission spectroscopy (ARPES) [32, 89] and scanning tunnelling spectroscopy [90] measurements have shown that the Fermi surface consists only of electron pockets centred on the X points of the iron square lattice and that the band structure, Fermi surface and gap symmetry are very similar to those of the monolayer $FeSe/SrTiO_3$ superconductor [32]. This makes $Li_{1-x}Fe_xOHFe_{1-y}Se$ a particularly promising material for studying the superconducting mechanism in the FeSCs with the highest known critical temperatures.

Several competing theoretical models have been proposed to explain the superconductivity and remarkably high T_c in $Li_{1-x}Fe_xOHFe_{1-y}Se$ and other iron-based superconductors whose Fermi surface consists only of electron pockets. A variety of novel

pairing mechanisms based on magnetic [43, 91–95] and orbital [96, 97] fluctuations have been suggested, with the theories predicting different superconducting gap symmetries, including sign-preserving s^{++}-wave and sign-changing s^{+-} or d-wave. A conclusive determination of the gap symmetry and sign distribution on the Fermi surface, which is crucial for distinguishing between these theories, has so far proved elusive.

As discussed in Section 1.4.3, measurements of a spin resonance peak in inelastic neutron scattering can yield useful information about the symmetry of the superconducting gap and therefore potentially distinguish between the proposed paring mechanisms. The aim of the experimental work in this chapter was to try to measure and characterise this resonance experimentally in $Li_{1-x}Fe_xOHFe_{1-y}Se$.

3.2 Sample Characterisation

Two separate batches of polycrystalline $Li_{1-x}Fe_xODFe_{1-y}Se$, with masses of 9.18 g (S1) and 8.17 g (S2) respectively, were synthesized via a novel lithiation method as detailed in Ref. [88]. Starting from FeSe, parent samples were first obtained via a hydrothermal synthesis route in the presence of a large excess of LiOD. These samples were washed with deionised and deoxygenated water to remove any soluble side products. Any magnetic impurities were removed using a strong magnet. The parent samples obtained in this way then underwent a lithiation procedure in which they were stirred in a solution of lithium in liquid ammonia. This final step adds extra Li to the sample, in the process moving Fe out of the intercalate layer and into the FeSe layer (decreasing x and y in the chemical formula). The daughter samples come very close to perfect FeSe layers with the minimum possible amount of magnetic Fe in the intercalate layer.

Fully-deuterated samples were prepared in order to reduce the incoherent background in the neutron scattering measurements. All sample handling was performed in an inert atmosphere as the samples are known to be air-sensitive, with exposure to air of even a few minutes affecting the superconductivity. Synchrotron x-ray powder diffraction patterns taken on the Diamond Light Source I11 beamline [98] (Fig. 3.1 main pan-

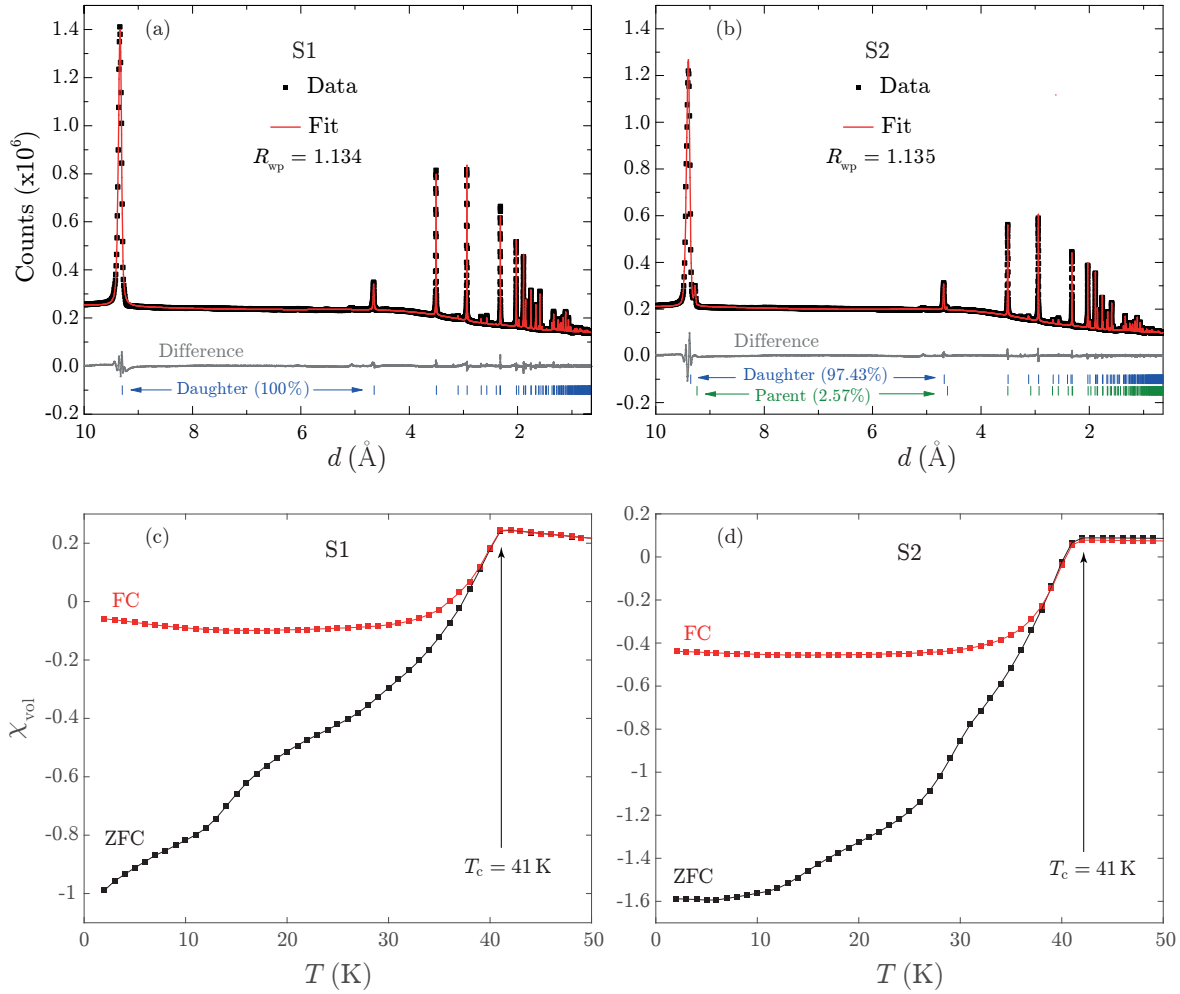

Figure 3.1: (a–b) X-ray powder diffraction data for two different deuterated powder samples S1 (a) and S2 (b) of $Li_{1-x}Fe_xODFe_{1-y}Se$ after lithiation. Neutron scattering data presented in later figures were recorded from the combined sample S1 + S2. Black points are experimental data and red lines are a fit obtained by Rietveld refinement with space group $P4/nmm$ and tetragonal lattice parameters a = 3.78088(1) Å, c = 9.30020(7) Å (Daughter S1 = $Li_{0.84}Fe_{0.16}ODFe_{0.99}Se$) and a = 3.77538(1) Å, c = 9.36136(7) Å (Daughter S2 = $Li_{0.83}Fe_{0.17}ODFe_{0.97}Se$). The sample in S2 is found to have a small impurity of the unlithiated parent sample (parent composition = $Li_{0.81}Fe_{0.19}ODFe_{0.94}Se$). (c–d) Measured volume magnetic susceptibility χ_{vol} on field-cooling (FC) and zero-field-cooling (ZFC) for the same two samples. T_c is determined using the first data point at which χ_{vol} begins to reduce with cooling. No correction has been made for demagnetisation.

els) show both samples to be high quality with almost no Fe vacancies in the FeSe plane and no detectable impurities except a small amount of unlithiated parent material in one of the samples. The refined compositions were $Li_{0.84}Fe_{0.16}ODFe_{0.99}Se$ (S1) and $Li_{0.83}Fe_{0.17}ODFe_{0.97}Se$ (S2) with a 2.6% impurity of $Li_{0.81}Fe_{0.19}ODFe_{0.94}Se$ in S2. The fitted crystal structure of the samples is presented schematically in Fig. 3.2, together with pure FeSe for comparison.

Field-cooled and zero-field-cooled magnetic susceptibility data taken on a Superconducting Quantum Interference Device (SQUID) magnetometer (Fig. 3.1 insets) show a high superconducting volume fraction and $T_c \simeq 41\,K$ in both samples. Evidence from a previous study on samples synthesised via the same method indicates that the impurity composition will either not superconduct or will do so only with a low T_c ($< 10\,K$) [88], and in light of this observation and its low mass fraction in the sample we expect the impurity to produce no measurable effect on the neutron spin resonance measurements discussed later in this work. We note that there is no essential difference in susceptibility between the deuterated samples measured here and published data from equivalent samples containing natural hydrogen [88], confirming that deuteration has no effect on the bulk superconducting properties of this system. Magnetic susceptibility and x-ray diffraction measurements confirmed that the samples remained unchanged after the experiment.

An independent study, Ref. [99], examined the magnetic behaviour of the Fe in the intercalate layer in one of the two samples used in this work (S1) via magnetisation and muon spin relaxation measurements, observing spin-glass-like behaviour with a freezing temperature $T_f \simeq 10\,K$. The inelastic neutron scattering spectra presented in this chapter are taken at temperatures significantly higher than 10 K and restricted to considerably higher energy transfer than any magnetic excitations seen in typical spin glasses [100] so it is unlikely the interstitial iron causes any signal in the datasets presented in this chapter.

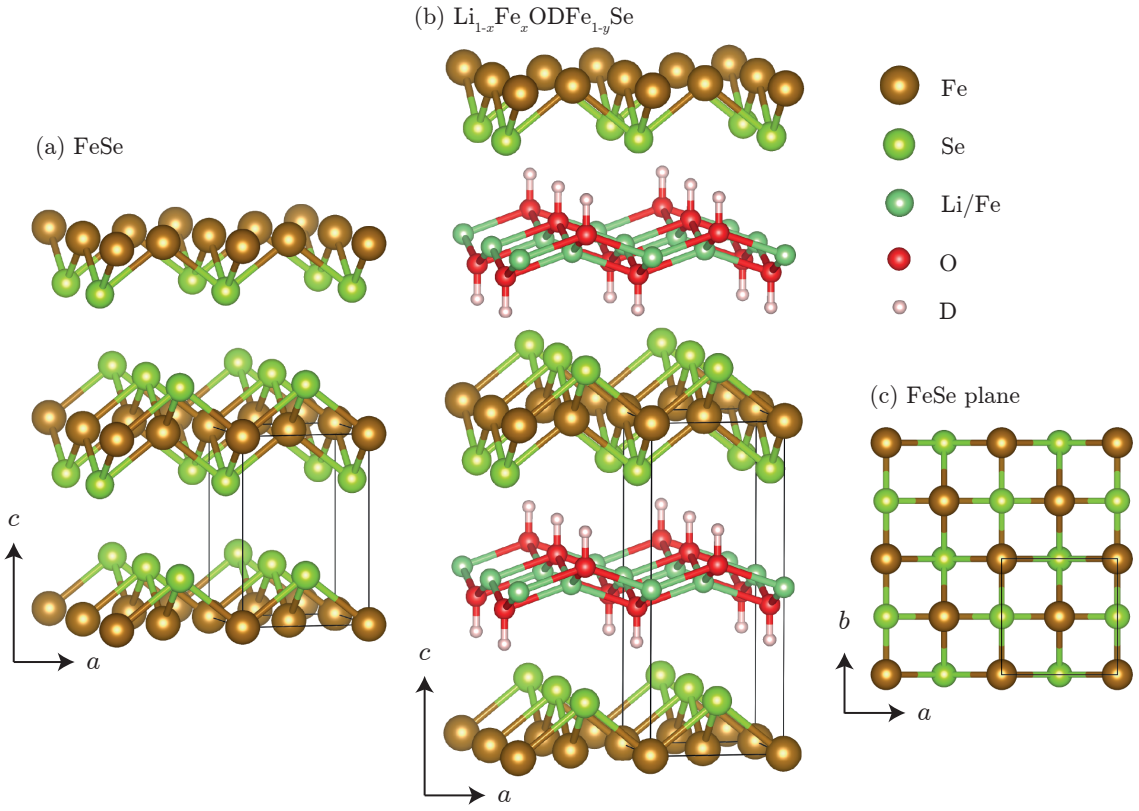

Figure 3.2: (a) The crystal structure of tetragonal FeSe. (b) The crystal structure of LiOD-intercalated FeSe, $Li_{1-x}Fe_xODFe_{1-y}Se$, studied in this chapter. (c) The FeSe square planar unit viewed along the c-axis. Black lines show the boundaries of a single two-Fe unit cell in each case.

3.3 Experimental Details

Inelastic neutron scattering measurements were performed on the Merlin time-of-flight chopper spectrometer at the ISIS facility [57]. The two powder samples S1 and S2 were sealed in separate aluminium foil packets in concentric annular geometry inside a cylindrical aluminium can with diameter 4 cm and height 4 cm. The can was mounted inside a closed-cycle cryostat. Spectra presented here were taken at a range of temperatures between 6.5 and 62 K with neutron incident energy $E_\mathrm{i} = 80$ meV and normalised to the scattering from a standard vanadium sample to place the data on an absolute intensity scale of $\mathrm{mb\,sr^{-1}\,meV^{-1}\,f.u.^{-1}}$, where $1\,\mathrm{mb} = 10^{-31}\,\mathrm{m^2}$ and f.u. stands for one formula unit of $Li_{1-x}Fe_xODFe_{1-y}Se$ (such that all scattering in this work is presented per Fe site in the FeSe layer), although we note that we have not corrected for the strong neutron attenuation of the sample. We estimate from the full width at half maximum (FWHM) of the elastic line that the energy resolution in this configuration is 5 meV at the elastic line and 3.7 meV at an energy transfer of 24 meV. All spectra presented here have also been corrected for the Bose population factor $\{1 - \exp(-E/k_\mathrm{B}T)\}^{-1}$, where E is the neutron energy transfer and T is the temperature, so that the presented quantity is the dynamical susceptibility $\chi''(Q, E)$.

3.4 Results

Figure 3.3 (a) presents scattering as a function of momentum transfer Q averaged over the energy transfer range $19 < E < 29$ meV. The two sets of measurements shown are for temperatures of $T = 6.5$ K and $T > T_\mathrm{c}$, where the $T > T_\mathrm{c}$ curve is an average of data collected at 51 and 62 K to improve the statistics. The justification for averaging is that the 51 and 62 K data show no observable difference over the (Q, E) range of interest after correction for the Bose factor. The general increase in scattering with Q is due to scattering from phonons, but the $T = 6.5$ K curve has a clear enhancement in spectral weight over the $T > T_\mathrm{c}$ curve in a broad range of Q from around 1.2 to 2.6 $\mathrm{Å^{-1}}$. We attribute the excess scattering at low temperatures to the spin resonance appearing

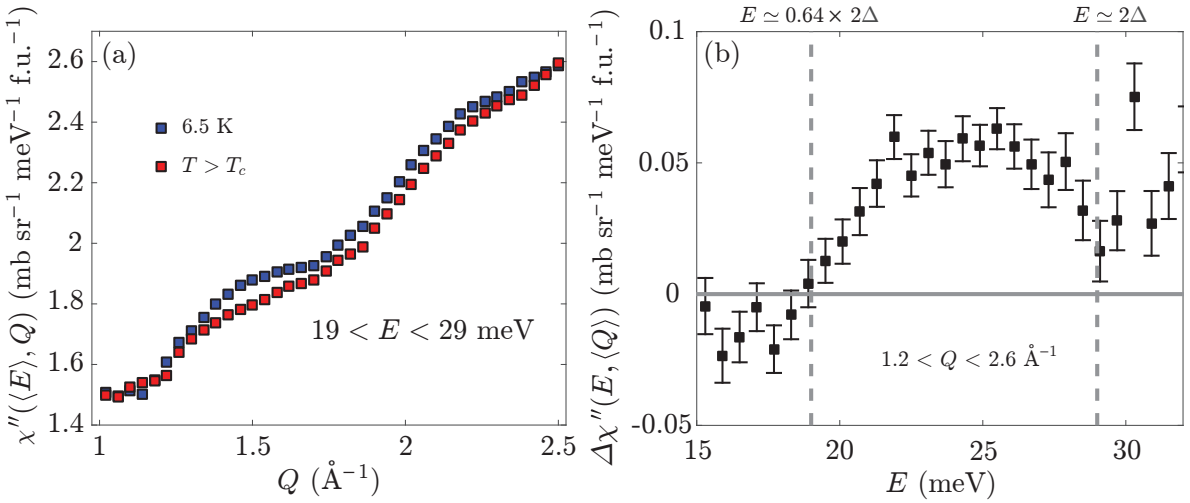

Figure 3.3: (a) Measured dynamical susceptibility of $Li_{0.84}Fe_{0.16}ODFe_{0.98}Se$ at $T = 6.5\,K$ and $T > T_c$ as a function of momentum transfer $Q = |\mathbf{Q}|$ averaged over the range of energy transfer $19 < E < 29\,meV$. Data for $T > T_c$ are an average of runs recorded at 51 K and 62 K. The formula unit (f.u.) used for normalisation is that of $Li_{0.84}Fe_{0.16}ODFe_{0.98}Se$. (b) Excess neutron scattering intensity $\Delta\chi''(E, \langle Q\rangle) = \chi''(E, \langle Q\rangle, T = 6.5\,K) - \chi''(E, \langle Q\rangle, T > T_c)$ as a function of energy transfer E. The normal state intensity is the average of runs recorded at 51 K and 62 K as in (a) and the signal is averaged across the full double peak structure, i.e. $1.2 < Q < 2.6$ Å^{-1}. Dashed vertical lines mark $E \simeq 2\Delta$ and $E \simeq 0.64 \times 2\Delta$, where $\Delta \simeq 14.5\,meV$ is the superconducting gap from ARPES [32].

in the superconducting state, since any change in the phonon background is taken into account by the Bose population factor correction.

Further evidence that this is the spin resonance can be seen in the energy dependence of excess scattering at 6.5 K relative to $T > T_c$ (Fig. 3.3 (b)), which shows a broad hump between about 20 and 30 meV. Using $T_c = 41\,K$ and the gap energy $\Delta \simeq 14.5\,meV$ measured by ARPES on samples of this material with the same electron doping level and T_c [32], we see that this signal is fully consistent with other unconventional superconductors where the resonance appears at $E_{res} \simeq 0.64 \times 2\Delta$ ($\simeq 19\,meV$), or more approximately at $E_{res} \simeq 5.8\,k_B T_c$ ($= 21\,meV$) [101].

A plot of the excess scattering as a function of Q averaged over the energy range from 19 to 29 meV is given in Fig. 3.4 (a). These energies correspond to the whole energy range for scattering below the pair-breaking energy from $0.64 \times 2\Delta \simeq 19\,meV$ up to $2\Delta \simeq 29\,meV$. The excess scattering has a double peak structure at 6.5 K with no clear change in the shape or position of either peak at intermediate temperatures

Composition	Q_1 (Å^{-1})	σ_1 (Å^{-1})	Q_2 (Å^{-1})	σ_2 (Å^{-1})
$Li_{0.84}Fe_{0.16}ODFe_{0.98}Se$	1.46(3)	0.12(4)	1.97(7)	0.32(8)
$Li_{0.6}(ND_2)_{0.2}(ND_3)_{0.8}Fe_2Se_2$	1.43(6)	0.27(7)	2.07(7)	0.21(8)

Table 3.1: Best-fit parameters for a two-Gaussian lineshape plus a constant background obtained from a least-squares fit to the 6.5 K data in Figure 3.4 (a) ($Li_{0.84}Fe_{0.16}ODFe_{0.98}Se$) and the 5 K data in Figure 3.5 ($Li_{0.6}(ND_2)_{0.2}(ND_3)_{0.8}Fe_2Se_2$, from Ref. [102]). The Q_is are peak centres and σ_is the corresponding standard deviations where $\sigma = \mathrm{FWHM}/2\sqrt{2\ln 2}$.

in the superconducting state, for example 30 K. Some other features are visible in the data, especially in the 30 and 42 K curves, which though small are not accounted for by statistical noise. These could be the result of subtle variations in the background signal with temperature, e.g. small changes in phonon modes, whose effect is magnified by the subtraction of two very similar signals.

In order to quantify the peak shapes and temperature dependence, we performed a fit similar to that in Ref. [102] of the subtracted data at 6.5 K to two Gaussian peaks plus a constant background. Peak heights a_i, centres Q_i and widths σ_i as well as the background were all allowed to vary independently, yielding the fitted parameters shown in Table 3.1. For intermediate temperatures, the peak widths and centres were fixed to the values in Table 3.1 and the ratio between the peak heights a_1/a_2 to its value at 6.5 K such that only two parameters, the overall amplitude of the whole feature A and the background, were refined. Within this treatment, A shows a general increasing trend below T_c (Fig. 3.4 (b)) which could plausibly be consistent with an order-parameter-like temperature dependence, $I \sim (T - T_0)^{1/2}$. However, there is insufficient data to establish such a relationship conclusively.

The spin resonance signal we observed here for $Li_{1-x}Fe_xODFe_{1-y}Se$ ($T_c \simeq 41$ K) is remarkably similar to that measured on a powder sample of $Li_{0.6}(ND_2)_{0.2}(ND_3)_{0.8}Fe_2Se_2$ ($T_c \simeq 43$ K) [102]. Cuts along the Q axis are presented for both materials in Fig. 3.5 averaged over the same energy range. The excess scatting at low temperatures shows the same double-peak structure for each material, with peak positions at the same Q to within experimental error. Fitted parameters are compared in Table 3.1. The most

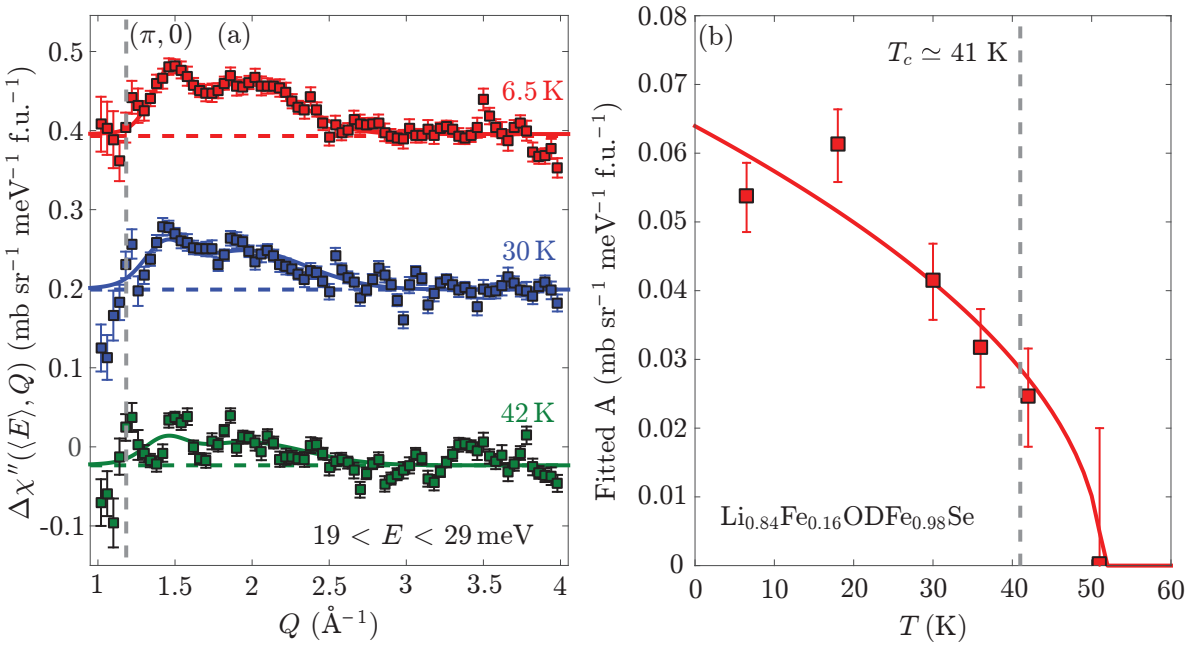

Figure 3.4: (a) Excess neutron scattering intensity as a function of Q at 6.5 K, 30 K and 42 K relative to the average of runs recorded at 51 K and 62 K, as in Fig. 3.3 (a). The 30 K and 6.5 K data have been offset vertically by 0.2 and 0.4 units, respectively. Dark coloured lines are a best fit to two Gaussians plus a constant background at each temperature, while horizontal broken lines are the constant background at each temperature as a guide to the eye. The dashed vertical line marks the Q position corresponding to the 2D wave vector $(\pi, 0)$ in the 1-Fe square lattice Brillouin zone. (b) Temperature dependence of the fitted overall amplitude A of the double-peak structure observed in (a). The red line is the best fit to an order-parameter-like behaviour $I \sim (T - T_0)^{1/2}$.

significant difference between the two datasets is a constant scale factor resulting in ~ 3 times more scattering per Fe site for the ammonia intercalate. This scale factor applies to the whole spectrum including the elastic line and is explained by increased attenuation (neutron absorption and elastic scattering) due partly to the greater presence of Li in the LiOD-intercalate, which exhibits a significant neutron absorption cross-section, and partly to the greater average neutron path length in the sample used here (the mass of sample measured in [102] was 11.4 g, compared to 17.98 g here). Another difference is some extra scattering from the ammonia-intercalate at low $Q \simeq 1.2\,\text{Å}^{-1}$ which has the effect of widening the lower Q peak and is not present for the LiOD-intercalate.

In order to gain information about the superconductivity from the data presented here it is necessary to know where the resonance occurs in the Brillouin zone. Using similar arguments to those presented in Ref. [102] for the ammonia-intercalate we attribute the two peaks to scattering from resonance positions in the first and second Brillouin zones. It is clear for the LiOD-intercalate that the resonance does not occur at the Fe square lattice wave vector $(\pi, 0)$, as found in pure FeSe [103] (vertical dashed lines in Figs. 3.4 (a) and 3.5). Instead, as shown in Fig. 3.6, it is found to be in the vicinity of $(\pi, \pi/2)$ and equivalent positions as seen in other FeSe intercalates, and is in fact best described by $(\pi, 0.67\pi)$. This is remarkably close to $(\pi, 0.625\pi)$ as predicted in one calculation [104].

In Ref. [102] it is suggested that the extra weight around $Q \simeq 1.2\,\text{Å}^{-1}$ may be from a small secondary superconducting phase with a $(\pi, 0)$ resonance appearing around 10 K, possibly due to some degree of phase separation or sample inhomogeneity. The sharper first order peak and complete lack of excess scattering at Q corresponding to $(\pi, 0)$ in the data presented here indicates there is no such minority phase or sample inhomogeneity in the LiOD-intercalate.

Similarly, the initial studies of the LiOH-intercalate reported evidence for either antiferromagnetic (Ref. [85]) or ferromagnetic (Ref. [86]) order. The low energy spin-wave excitations of any long-range magnetic order would have a characteristic scattering intensity at low energies which would disperse away from the respective order-

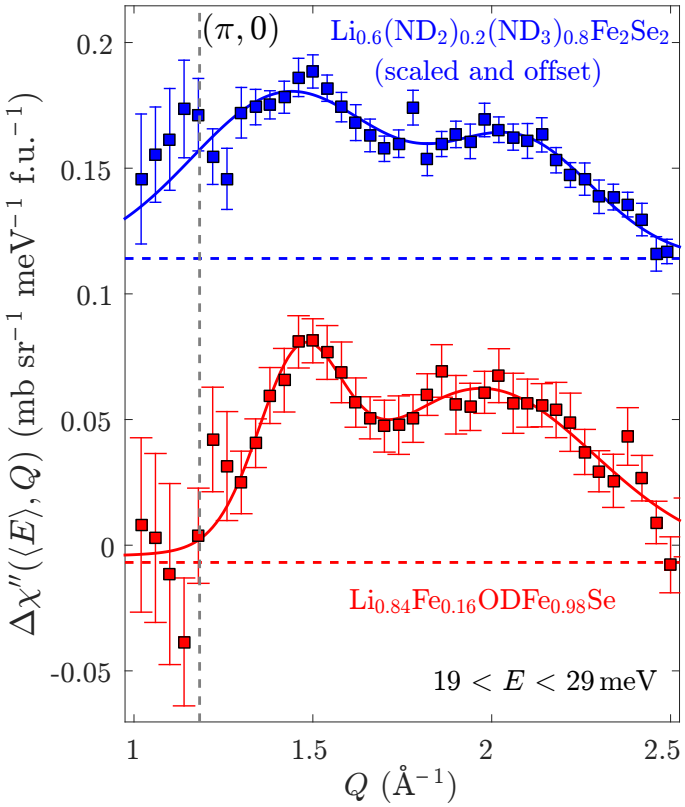

Figure 3.5: The 6.5 K dataset from Fig. 3.4 (a) for $Li_{0.84}Fe_{0.16}ODFe_{0.98}Se$ plotted with an equivalent dataset at 5 K for the lithium ammonia/amide intercalated $Li_{0.6}(ND_2)_{0.2}(ND_3)_{0.8}Fe_2Se_2$ from Ref. [102]. For ease of comparison, the $Li_{0.6}(ND_2)_{0.2}(ND_3)_{0.8}Fe_2Se_2$ dataset has been offset vertically and scaled by a constant factor so that the lower Q peak maximum is the same height above background as that in the $Li_{0.84}Fe_{0.16}ODFe_{0.98}Se$ data to take into account the differing attenuation between the two samples.

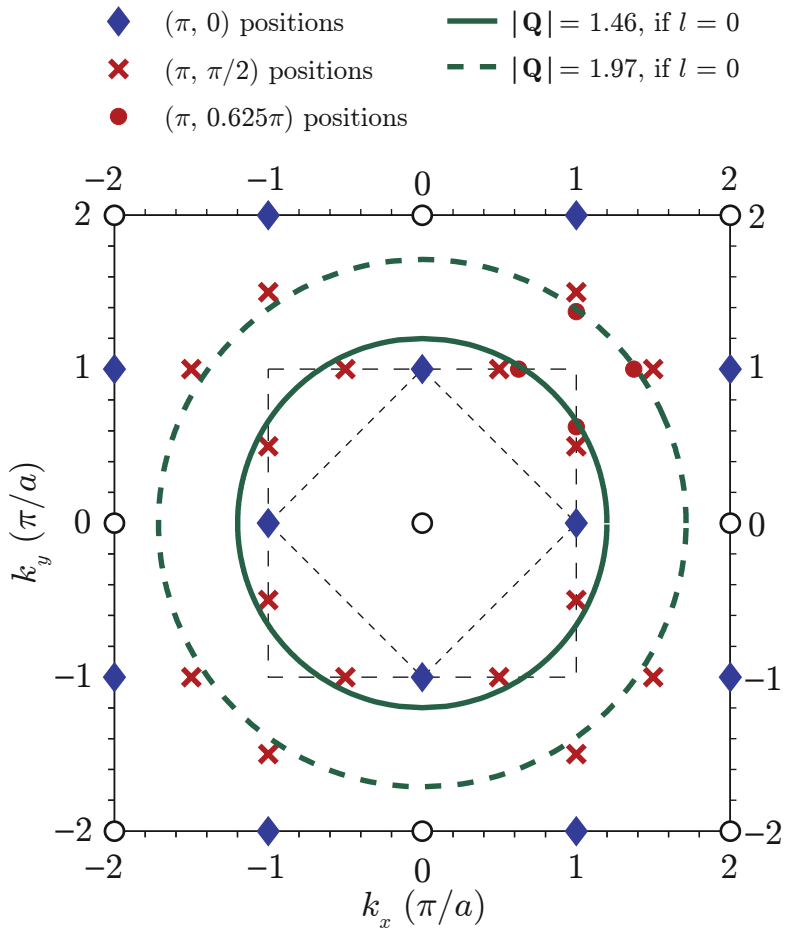

Figure 3.6: Schematic of the $k_z = 0$ plane in the reciprocal space of $Li_{1-x}Fe_xODFe_{1-y}Se$ and $Li_{0.6}(ND_2)_{0.2}(ND_3)_{0.8}Fe_2Se_2$ with selected points of interest marked. Green circles mark the possible wavevectors of the spin resonance seen in this work and Ref. [102], assuming $l = 0$. Longer and shorter dashed black lines mark the 1-Fe and 2-Fe Brillouin zone boundaries respectively. Figure reproduced from Ref. [102]

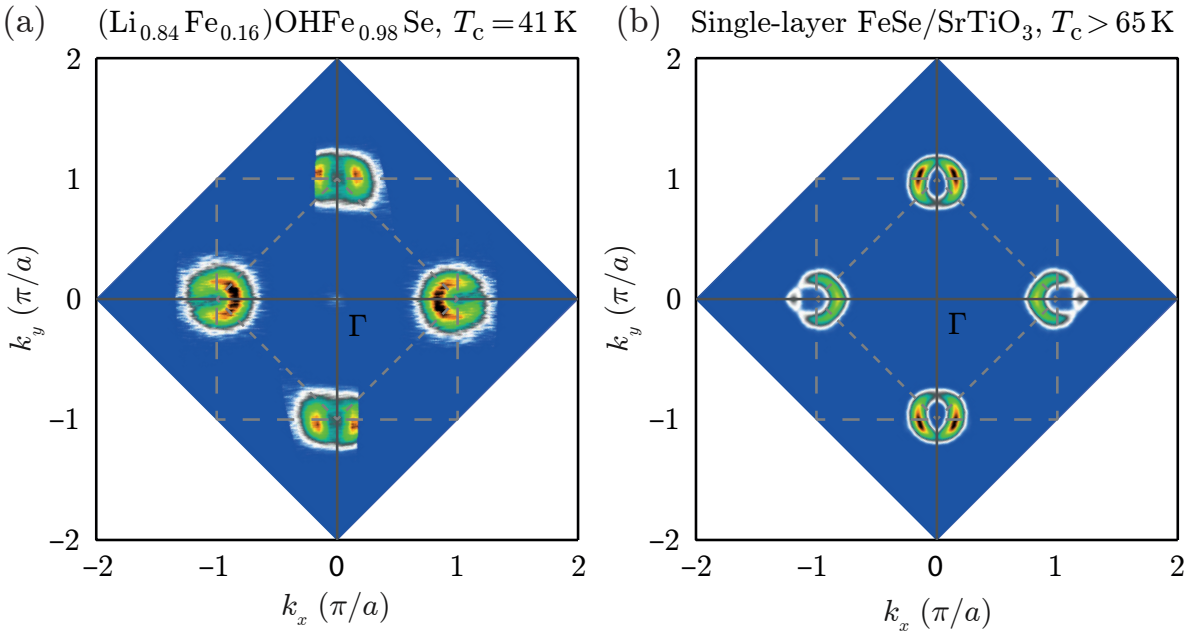

Figure 3.7: ARPES data at 20 K in the $k_z = 0$ plane for (a) $Li_{0.84}Fe_{0.16}OHFe_{0.98}Se$ and (b) monolayer FeSe on $SrTiO_3$, showing the similarity of the band structure. Grey squares mark the Brillouin zone boundaries. Figure reproduced from Ref. [32].

ing wave vectors. We did not observe any such scattering in the neutron spectrum of $Li_{0.84}Fe_{0.16}ODFe_{0.98}Se$, consistent with the lack of any magnetic Bragg peaks in neutron diffraction [88, 105, 106]. Furthermore, the study Ref. [99] on the same sample used in our work also saw no evidence for long-range magnetic order at any temperature in magnetisation and muon spin rotation (μSR) measurements. Since μSR in particular is a highly sensitive probe of any internal magnetic fields this makes magnetic order in our sample extremely unlikely and constrains any magnetic order in samples of optimally superconducting $Li_{1-x}Fe_xOHFe_{1-y}Se$ in other works to a minority phase with different chemical composition.

3.5 Discussion

Recently, the band structure, Fermi surface and superconducting gap of LiOH-intercalated FeSe with the same level of electron doping and T_c as the sample used in this work were measured in two ARPES studies [32, 89] and via scanning tunnelling spectroscopy [90]. Some of the ARPES data from one of these studies, Ref. [32], is reproduced in Fig. 3.7 for reference. Both ARPES studies found that the Fermi surface consists of almost iden-

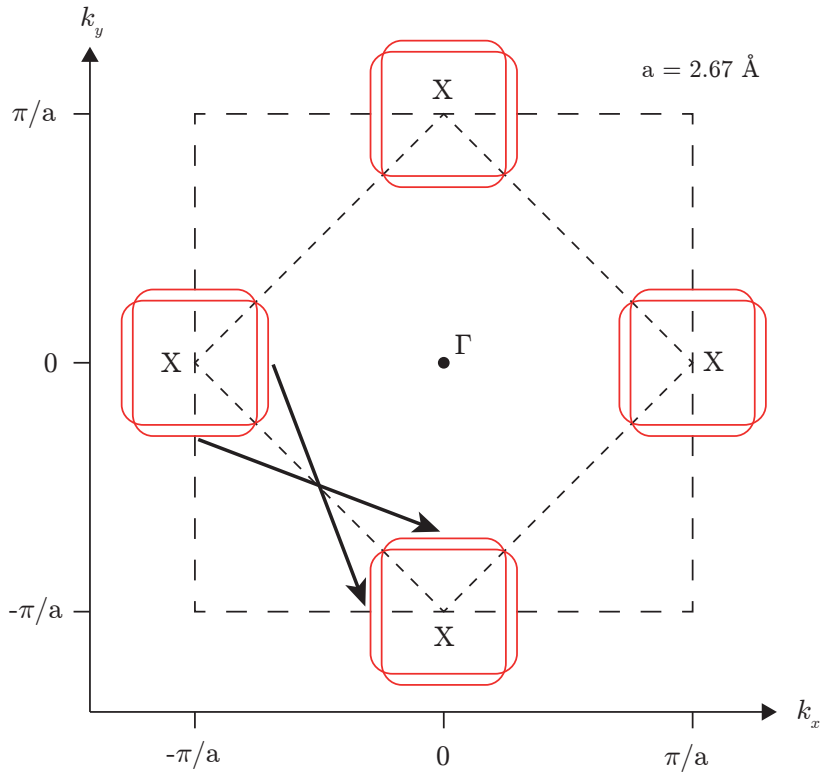

Figure 3.8: Schematic Fermi surface in the $k_z = 0$ plane for $Li_{1-x}Fe_xOHFe_{1-y}Se$, based on the calculation in Ref. [104] and qualitatively consistent with all current experiments. Brillouin zone boundaries are marked with thick dashed lines (1-Fe BZ) and thin dashed lines (2-Fe BZ) while the lattice parameter used here $a = 2.67\,\text{Å}$ is that of the 1-Fe in-plane unit cell. Γ and X labels mark special points of the 1-Fe Brillouin zone, with each X point surrounded by two box-like fermi sheets (red lines) which in reality are presumably hybridised at the points where they approach each other to avoid crossings. Thick arrows mark nesting vectors between straight, parallel sections of Fermi surface which cause a peak in nesting around $(\pi, 0.625\pi)$ as calculated in Ref. [104].

tical, highly 2D electron pockets centred on $(\pi, 0)$ and $(0, \pi)$, i.e. the two X points of the 1-Fe square lattice Brillouin zone, although theoretical calculations indicate that it is reasonable to expect two closely spaced Fermi sheets at each of these X points which are presumably not resolvable in ARPES and may hybridise with one another. The scanning tunnelling spectroscopy study provided strong evidence for this two-Fermi-sheet scenario, showing that there are two different superconducting gaps. A schematic of this Fermi surface geometry is provided in Fig. 3.8, with the precise Fermi surface cross-sections represented by those calculated in Ref. [104], although it should be noted that there is no experimental verification of these cross-sections due to limited resolution in ARPES.

Naïvely, nesting in this Fermi surface geometry would be expected to peak at (π, π),

i.e. the vector connecting two X points at $(\pi, 0)$ and $(0, \pi)$, however it has been shown via theoretical calculations [95, 104] that if the pockets have a non-circular cross section then it is possible for the nesting to have a broad plateau around (π, π) and to reach its maximum at some other position. For example, a full calculation for the type of Fermi surface represented in Fig. 3.8 shows the maximum is at $(\pi, 0.625\pi)$ [104] due to enhanced nesting between parallel sections of the box-like Fermi surfaces as marked by bold arrows in Fig. 3.8. It is also possible to obtain a peak at $(\pi, \pi/2)$, as observed for the alkali-metal intercalates [107–111], or at $(\pi, 0.67\pi)$ as found in this work, by varying the precise Fermi surface geometry and size slightly. The detailed shape of the Fermi surface around the X points is not established in the ARPES data reported so far on $Li_{1-x}Fe_xOHFe_{1-y}Se$.

In weak-coupling spin fluctuation models the spin resonance is caused by nesting between sections of Fermi surface *with the opposite sign of the superconducting gap*, so our observation of a resonance at the very least rules out s^{++} pairing in which the gap has the same sign at all places on all Fermi sheets.

There is evidence from scanning tunnelling spectroscopy (STS) [90] that the gaps on all Fermi sheets are nodeless and anisotropic, with the fitted gaps nevertheless preserving the 4-fold rotational symmetry of the crystallographic space group. If this is assumed to be correct then only three possible gap distributions remain, with either (i) the sign change between two decoupled Fermi sheets at the same X point, or (ii) the sign change between equivalent Fermi sheets at different X points, or (iii) both (i) and (ii). In order to verify these assumptions a better experimental determination of the Fermi surface structure around a single X point is required, for example from higher resolution ARPES, STS or quantum oscillations experiments.

3.6 Subsequent Works

Following the publication of the work in this chapter, several other studies on the same material appeared. In particular, a single crystal inelastic neutron scattering study [112]

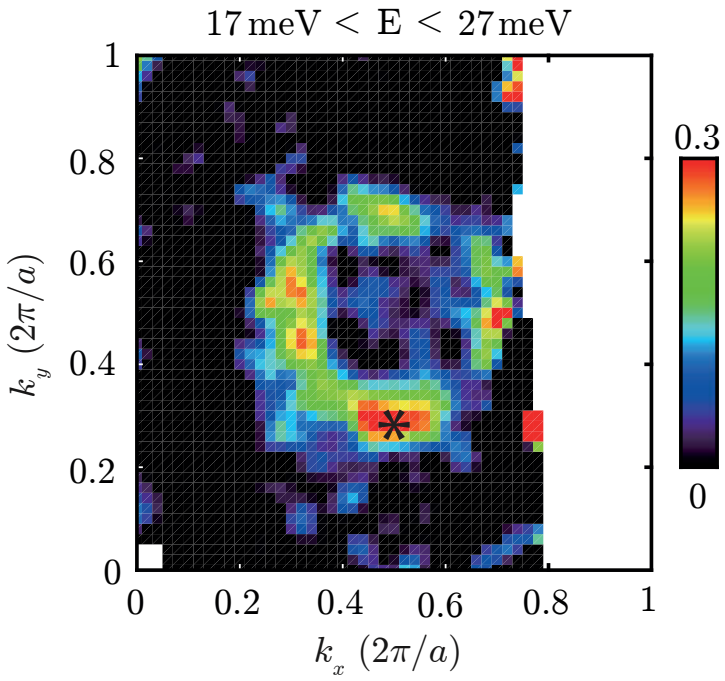

Figure 3.9: The spin resonance in the $k_z = 0$ plane in a single crystal of $Li_{0.8}Fe_{0.2}ODFeSe$ observed via inelastic neutron scattering. The hot-spot marked * is at the wavevector $(\pi, 0.67\pi)$ consistent with the powder data presented in this chapter. Figure reproduced from Ref. [112].

measured the $k_z = 0$ plane structure of the spin resonance, seeing rings of scattering surrounding $(\pi, \pi, 0)$ which are peaked at $(\pi, 0.62\pi, 0)$ as shown in Fig. 3.9. Another independent inelastic neutron scattering study [113] performed similar measurements at $k_z = \pi$, observing scattering peaked at $\mathbf{Q} = (\pi, 0.54\pi, \pi)$. In both cases the energy dependence shows a broad enhancement in scattering between around 16 meV and 30 meV and the enhanced scattering is absent above T_c, consistent with a spin resonance. Overall these data are consistent with and confirms the conclusions of our powder experiment, with the additional observation of a small, non-trivial k_z dependence which could not have been deduced from our data due to the effects of powder averaging.

There is also a recent quasiparticle interference (QPI) study [34] looking at the QPI pattern near to non-magnetic Zn impurities in the FeSe layer which presented evidence that the sign-change in the gap function is between the two Fermi sheets at the same X point, i.e. case (i) from the discussion above. However, one theoretical study cast some doubt on the validity of this novel technique [35].

3.7 Summary

In summary, we have observed a spin resonance appearing in the superconducting state of the FeSe intercalate $Li_{0.84}Fe_{0.16}ODFe_{0.98}Se$ at a 2D wave vector close to $(\pi, \pi/2)$ as found in other FeSe-intercalates. Best agreement with the data is obtained with the wave vector $(\pi, 0.67\pi)$. We see no evidence for a $(\pi, 0)$ resonance, and the data are remarkably similar to previous measurements on the lithium ammonia/amide intercalate $Li_{0.6}(ND_2)_{0.2}(ND_3)_{0.8}Fe_2Se_2$ reported in Ref. [102]. The observed wavevector $(\pi, 0.67\pi)$ is plausibly consistent with the nesting vector between pairs of 2D electron Fermi sheets around $(\pi, 0)$ and $(0, \pi)$ seen in ARPES and scanning tunnelling spectroscopy, which rules out conventional s^{++} pairing. When considered in the light of evidence that the gap is nodeless, the observations constrain the sign of the gap to have one of three possible distributions on the Fermi surface.

Chapter 4

Coupled charge density wave and lattice distortion in $Na_2Ti_2Pn_2O$ (Pn = As, Sb)

In this chapter I present a single crystal x-ray diffraction study of the titanium oxypnictide compounds $Na_2Ti_2Sb_2O$ and $Na_2Ti_2As_2O$, with supporting μSR and ARPES measurements. These materials, along with other physically similar titanium oxypnictides, exhibit density wave (DW) transitions in close proximity to superconductivity whose precise nature and symmetry-breaking has been the subject of considerable debate. In many established unconventional superconductors it is thought that superconductivity and the proximate density wave order are intimately connected, so information about the precise nature of the density wave order in titanium oxypnictides is likely to be crucial in establishing the superconducting mechanism in this family.

Single crystal x-ray diffraction data on $Na_2Ti_2Sb_2O$ and $Na_2Ti_2As_2O$ samples had shown clear, weak superstructure reflections at non-integer (h, k, l) positions appearing at the density wave transition temperature T_{DW}, indicative of a small crystallographic distortion. I was able to refine against the data the different possible distortion modes which correspond to the irreducible representations of the crystallographic space group.

In this way we obtained the precise distortion mode and all atomic positions in the DW phase for both studied compositions. By analysing band back-folding in our collaborators' ARPES data as well as some μSR data from powder samples I was then able to use the distortion modes I had established to show that the DW in both samples studied is a commensurate, two-**q** charge density wave and determine the active propagation vectors in each case. This result implies a strong electron–phonon coupling, offering a likely explanation for the superconductivity in the related material $BaTi_2Sb_2O$.

The results and analysis presented in this chapter have been published in Physical Review B **94**, 104515 (2016).

I am grateful to a number of collaborators on this project, including the group of Y.-G. Shi at the Chinese Academy of Science in Beijing who grew the crystals, L. Gannon, A. J. Princep and A. T. Boothroyd from my research group in Oxford and the beamline scientists on I19 at the Diamond Light Source who performed the XRD measurements and R. D. Johnson who helped with the symmetry analysis.

4.1 Introduction

As discussed in earlier chapters, unconventional superconductivity often appears in the neighbourhood of other symmetry-breaking ground states, especially density waves [114]. In many of the prominent theoretical scenarios strong fluctuations of the order parameter characteristic of the proximate density wave ground state appear close to the superconducting region of the phase diagram and are integral to the pairing interaction. Since there is such a strong relationship between the symmetry of the density wave state and that of the superconducting pairing interaction it is therefore important to fully determine the nature of any phase competing with superconductivity and any associated broken symmetries.

Superconductivity close to spin density wave order has been established in many systems, notably the iron-based superconductors. The SDW in these materials is assisted by partial nesting of quasi-two-dimensional electron and hole Fermi surface pockets [27, 115],

which is suppressed under a range of conditions including doping and chemical and physical pressure. At the point where the SDW is suppressed strong spin fluctuations in the equivalent symmetry channel remain and these fluctuations are widely thought to play a central role in mediating unconventional superconducting pairing [116]. Superconductivity proximate to CDW formation is less often encountered but is known in several transition-metal chalcogenides and oxides [117–120], especially the layered copper oxides where CDW order is found to compete with superconductivity in several hole-doped materials [28, 121–126]. Theoretical work suggests that charge fluctuations near the onset of CDW order may play an important role in the superconducting pairing mechanism [127].

The layered titanium oxypnictides [128] $A\mathrm{Ti}_2Pn_2\mathrm{O}$ (A = Ba, Na_2, $(\mathrm{SrF})_2$, $(\mathrm{SmO})_2$; Pn = As, Sb, Bi) share structural similarities with the copper oxide and Fe-based superconductors and display anomalies in magnetic, transport and thermal properties at various temperatures up to 400 K which have been interpreted as some kind of density wave transition [129–136]. Recently, superconductivity at $T_\mathrm{c} \simeq 1.2\,\mathrm{K}$ was discovered in one member of this family, $\mathrm{BaTi}_2\mathrm{Sb}_2\mathrm{O}$, which also shows a proposed DW order below $T_\mathrm{DW} \simeq 55\,\mathrm{K}$, prompting suggestions of unconventional superconductivity [136, 137]. This explanation was supported by the observation that substitution of Na for Ba increases T_c up to 5.5 K with concomitant gradual suppression of the DW transition [137]. A similar anticorrelation between T_c and T_DW has been observed with other chemical substitutions indicating competition between the superconducting and DW phases, although there remain large regions of the phase diagrams in which they appear to coexist [138–142].

Many attempts have been made to identify the nature of the DW phase in the titanium oxypnictides, although a complete characterisation has proved elusive. Electronic structure models predict a highly anisotropic Fermi surface with box-like electron and hole pockets that are quite well nested and therefore susceptible to either SDW or CDW instabilities [143–149], and ARPES data revealed a Fermi surface in good agreement with

theory as well as evidence for gap formation at the DW transitions on parts of the Fermi surface, confirming that the DW has a strong electronic component [150, 151]. Meanwhile Density Functional Theory (DFT) phonon calculations predicted strong electron–phonon coupling, which could plausibly induce a crystallographic distortion and encourage a CDW in the accompanying symmetry channel [152, 153].

μSR studies of Na-doped $BaTi_2(As_{1-x}Sb_x)_2O$ did not detect any static magnetic moments, leading to the conclusion that the DW phase in this composition cannot be a SDW and is most likely a CDW [154, 155], while a Nuclear Quadrupole Resonance (NQR) study observed microscopic breaking of 4-fold symmetry and concluded that only a commensurate CDW could explain the data [156].

Further evidence for 4-fold symmetry breaking at the DW temperature came from a neutron diffraction study in $BaTi_2(As,Sb)_2O$ [157] and Raman scattering in $Na_2Ti_2As_2O$ [158]. Electron and neutron diffraction studies of ATi_2Pn_2O compounds [154, 157] did not observe any magnetic or charge superstructure associated with a SDW or CDW ordering, however, prompting proposals that the DW phase is either some form of novel intra- unit cell orbital nematic state [157, 159], or is characterized by an orbital polarization that takes place without any lowering of symmetry [160].

The aim of the work presented here was to search for a crystallographic distortion at the DW temperature as predicted by phonon DFT using high-resolution x-ray diffraction. Any such distortion would likely be coupled to a CDW with the same symmetry via electron-phonon coupling, so a full low-temperature structural characterisation may shed light on the symmetry breaking of the DW.

4.1.1 High-Temperature Crystal Structure

The established high-temperature crystal structure of the titanium oxypnictides is shown in Fig. 4.1. The key structural element present in all compositions is the Ti_2O square planar motif, with O sites on the corners of the squares and Ti on the sides (Fig. 4.1 (c)). This is the anti-structure of the CuO_2 planes seen in the high-temperature cuprate superconductors. Above and below the centre of the squares are pnictogen (Pn) sites

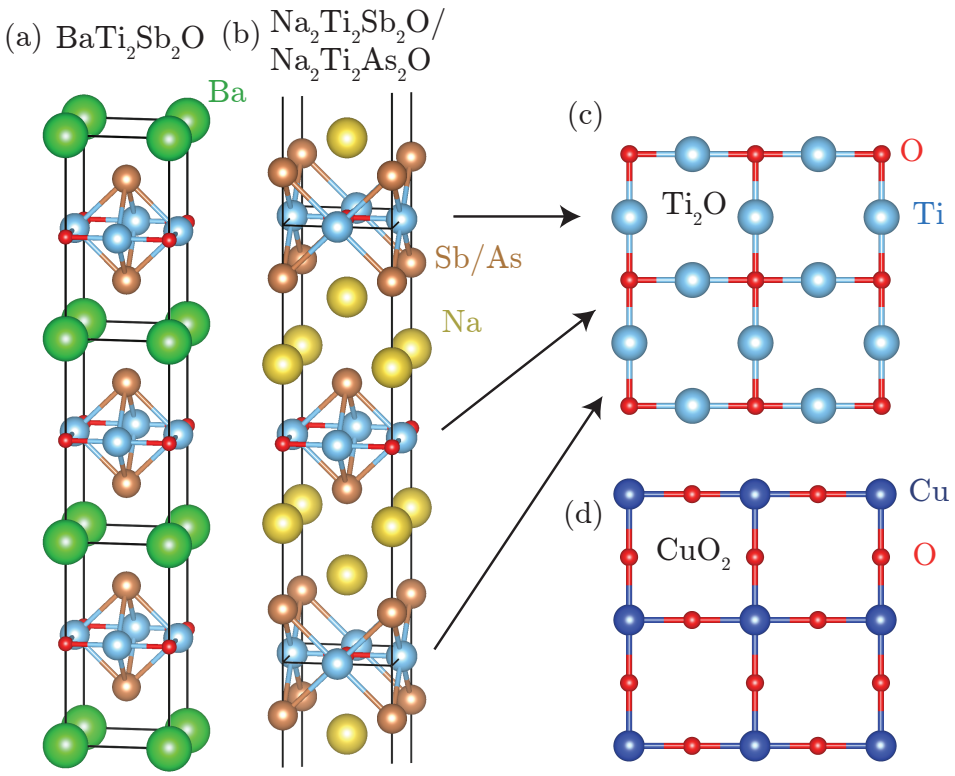

Figure 4.1: (a) The crystal structure of superconducting $BaTi_2Sb_2O$ (b) The crystal structure of the compositions studied in this chapter, $Na_2Ti_2Sb_2O$ and $Na_2Ti_2As_2O$ (c) The Ti_2O square-planar unit common to all Ti oxypnictide families (d) The structurally similar CuO_2 square-planar unit present in the Copper Oxide high-T_c superconductors.

occupied by As, Sb or Bi, which is similar to the structure of the iron-based superconductors. The electronic properties of the iron-based superconductors are very sensitive to the height of the pnictogen site above the Fe layer, presumably since hybridisation with the pnictogen p-orbitals significantly modifies in-plane Fe-Fe bonding, and the Ti oxypnictides have been shown to exhibit a similar sensitivity to this parameter [128].

The valence states of the constituent ions in the active Ti_2Pn_2O layers are O^{2-}, Pn^{3-} and Ti^{3+}, with the Ti valence state being especially noteworthy as it leads to a d^1 configuration which is the conjugate of the d^9 configuration of Cu in the cuprates and might therefore be expected to behave in a similar manner. The total charge per Ti_2Pn_2O formula unit is –2, meaning that positively charged spacer layers are required for overall charge neutrality. In the two compositions studied here there are two Na^+ spacer layers between active Ti_2Pn_2O layers, whereas for the superconducting composition there is a single Ba^{2+} layer (Fig. 4.1 (a–b)). There is also some variation in stacking, with the square planes in neighbouring pairs of Ti_2Pn_2O layers being offset by the in-plane vector (1/2, 1/2) for $Na_2Ti_2Pn_2O$, while neighbouring planes are not offset in $BaTi_2Pn_2O$.

4.2 Sample Characterisation

Single crystals and powder samples of $Na_2Ti_2Sb_2O$ and $Na_2Ti_2As_2O$ were prepared via a flux method as described by Shi *et al.* [161]. High-purity starting materials of Ti and TiO_2 powder were mixed together with NaAs or NaSb flux in the correct molar ratio and heated in an inert atmosphere at around 1200 ^{0}C for 5 hours before being cooled and spun in a centrifugal separator to remove excess flux. Following this process, plate-like single crystals with typical dimensions of around 3 mm× 3 mm× 0.1 mm were obtained.

Magnetic susceptibility and electrical resistivity measurements (Fig. 4.2) show clear anomalies at $T_{\mathrm{DW}} \simeq 115\,\mathrm{K}$ and $T_{\mathrm{DW}} \simeq 320\,\mathrm{K}$ for $Pn =$ Sb and As, respectively, coinciding with the DW transition temperatures in these materials known from literature [161]. The $Pn =$ As compound appears to undergo a metal-to-insulator transition on cooling through T_{DW}, whereas for $Pn =$ Sb the sample remains metallic throughout, albeit

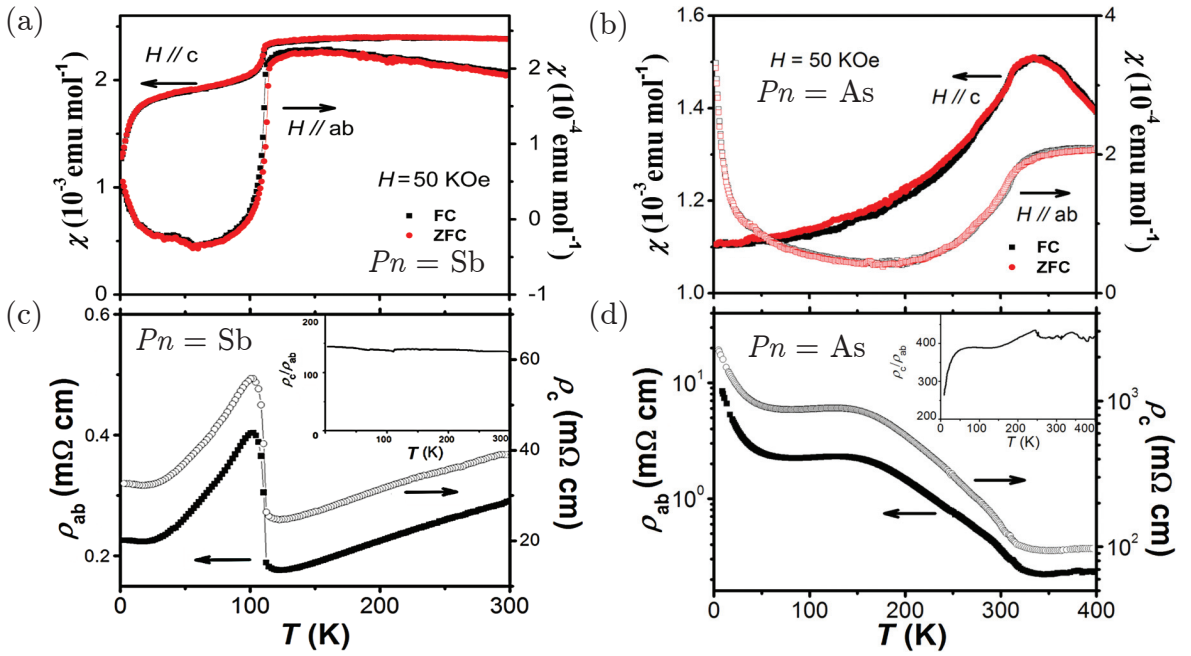

Figure 4.2: (a–b) In-plane ($H \parallel ab$) and out-of-plane ($H \parallel c$) magnetic susceptibility of single crystals of $Na_2Ti_2Sb_2O$ (a) and $Na_2Ti_2As_2O$ (b). (c–d) In-plane (ρ_{ab}) and out-of-plane (ρ_c) resistivity of the same crystals. Figures reproduced from Ref. [161].

with a stepped increased in resistivity on entering the DW phase. There is also a large uniaxial anisotropy with magnetic susceptibility and electrical resistivity being an order of magnitude higher out-of-plane (parallel to the c-axis) than in-plane (perpendicular to c), consistent with a layered structure. There is no evidence for in-plane symmetry breaking in this initial transport data.

4.3 Results and analysis

4.3.1 Muon Spin Relaxation (μSR)

μSR measurements were performed on the EMU spectrometer at the ISIS Pulsed Muon Facility using powder samples of $Na_2Ti_2Pn_2O$ (Pn = Sb, As) packed inside 25μm silver foil packets mounted on a silver backing plate and measured at temperatures above and below T_{DW} using a closed-cycle refrigerator. Figure 4.3 shows the temperature variation of the measured zero-field μSR asymmetry after muon implantation. The asymmetry shows no characteristic features associated with magnetic order (oscillations) or magnetic fluctuations in either sample and has a very small relaxation rate which is virtually

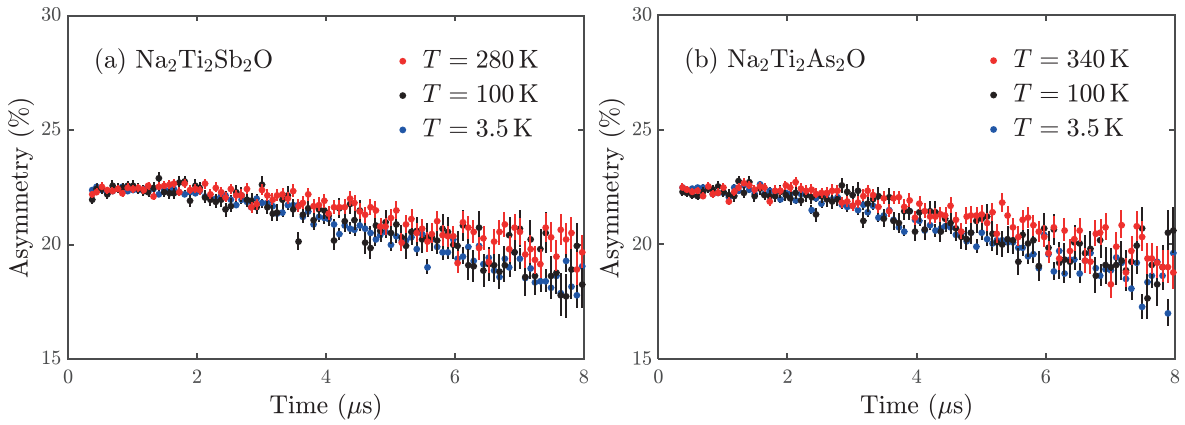

Figure 4.3: Temperature dependence of the μSR asymmetry for (a) $Na_2Ti_2Sb_2O$ and (b) $Na_2Ti_2As_2O$. There is no evidence in the curves for any relaxation due to magnetic order or magnetic fluctuations.

independent of temperature. Furthermore, there was no change in the asymmetry of the muon spin precession in a weak transverse field, indicating that any magnetic fluctuations at the muon stopping site are negligibly small. This observed μSR behaviour is most likely dominated by nuclear relaxation from Na and Sb/As nuclei with the very small temperature variation plausibly caused by muon diffusion at high temperatures. These results strongly indicate that the DWs in $Na_2Ti_2Pn_2O$ are most likely CDWs rather than SDWs, since a SDW would result in magnetic fluctuations and long-range order.

4.3.2 X-ray Diffraction

Temperature dependent x-ray diffraction measurements were performed on single crystal samples of $Na_2Ti_2Pn_2O$ (Pn = Sb, As) using a Mo-source Oxford Diffraction Supernova diffractometer equipped with a liquid nitrogen flow cryostat. The diffraction data presented here on $Na_2Ti_2As_2O$ were collected from a large single crystal of approximate dimensions $2 \times 0.5 \times 1\,mm^3$, while data taken on $Na_2Ti_2Sb_2O$ were from a much smaller sample $0.5 \times 0.5 \times 0.1\,mm^3$. Additionally, synchrotron x-ray diffraction patterns were recorded from a single-crystal of $Na_2Ti_2Sb_2O$ at high ($T = 300\,K > T_{DW}$) and low ($T \sim 100\,K < T_{DW}$) temperatures on the I19 beamline [162] at the Diamond Light Source. The experiment was conducted in the experimental hutch EH1 using an incident monochromatic beam at the Zr edge with a wavelength of 0.6889 Å, and a 4-circle diffractometer with a charge-coupled device (CCD) detector. The Helix device installed

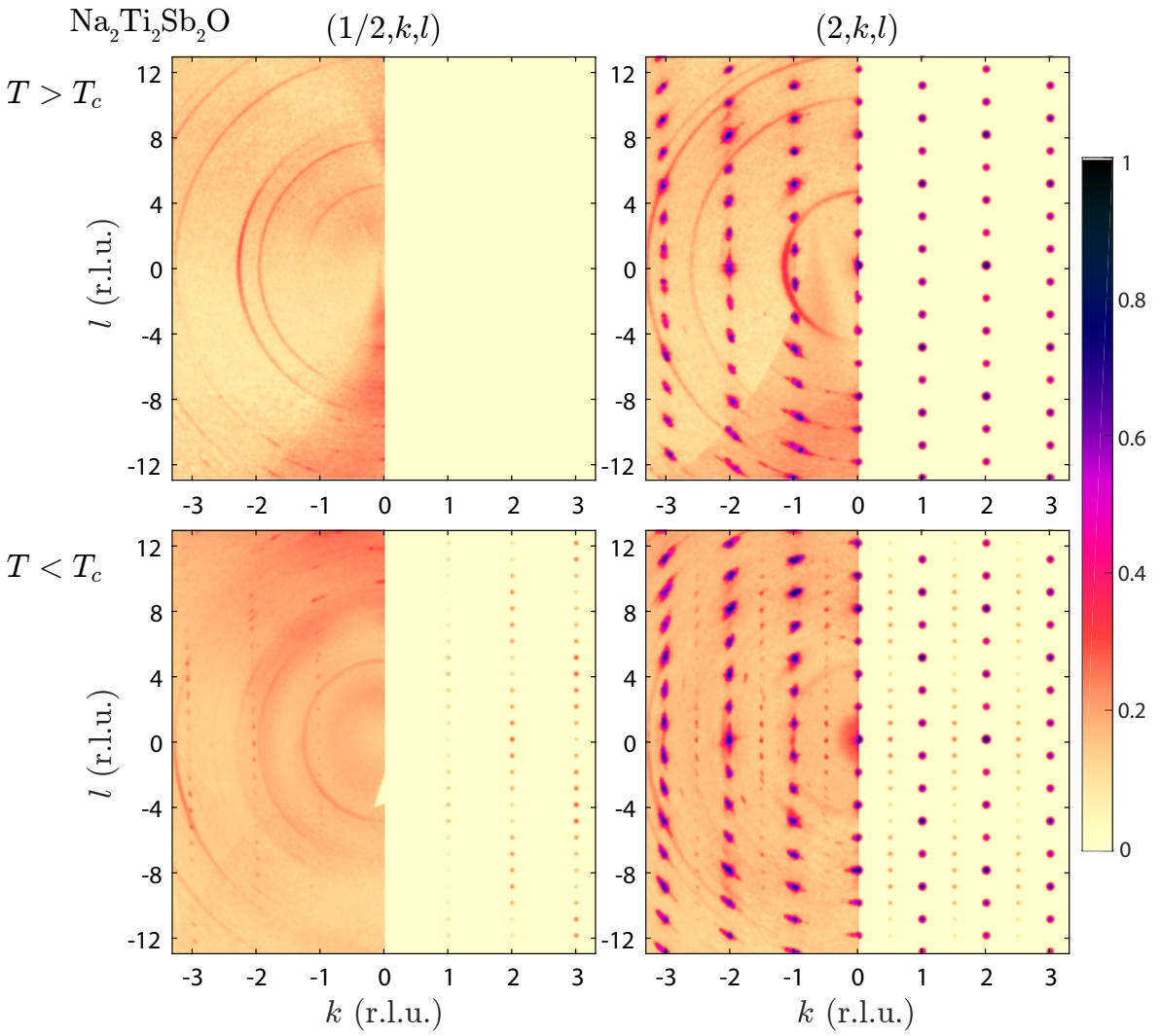

Figure 4.4: Experimental single crystal x-ray diffraction maps (left half-panels) and simulations (right half-panels) in the $(1/2, k, l)$ and $(2, k, l)$ reciprocal space planes of $Na_2Ti_2Sb_2O$ measured at temperatures above (300 K) and below (∼100 K) the structural distortion temperature T_{DW}. Intensities are plotted on a log scale.

on the beamline was used to cool the sample below its transition temperature using a flow of helium. These samples are air-sensitive and were coated with vacuum grease to prevent decomposition during diffraction measurements.

Figures 4.4 and 4.5 present x-ray diffraction intensity maps for $Na_2Ti_2Sb_2O$ and $Na_2Ti_2As_2O$ respectively in the $(1/2, k, l)$ and $(2, k, l)$ reciprocal space planes recorded above and below T_{DW}. Well-resolved Bragg peaks were seen in all these diffraction measurements, although data from both compounds show some elongation of the Bragg peaks along the c^*-direction and some mosaic broadening, especially in $Na_2Ti_2As_2O$. This indicates some disorder along the c-axis, likely due to random stacking faults which

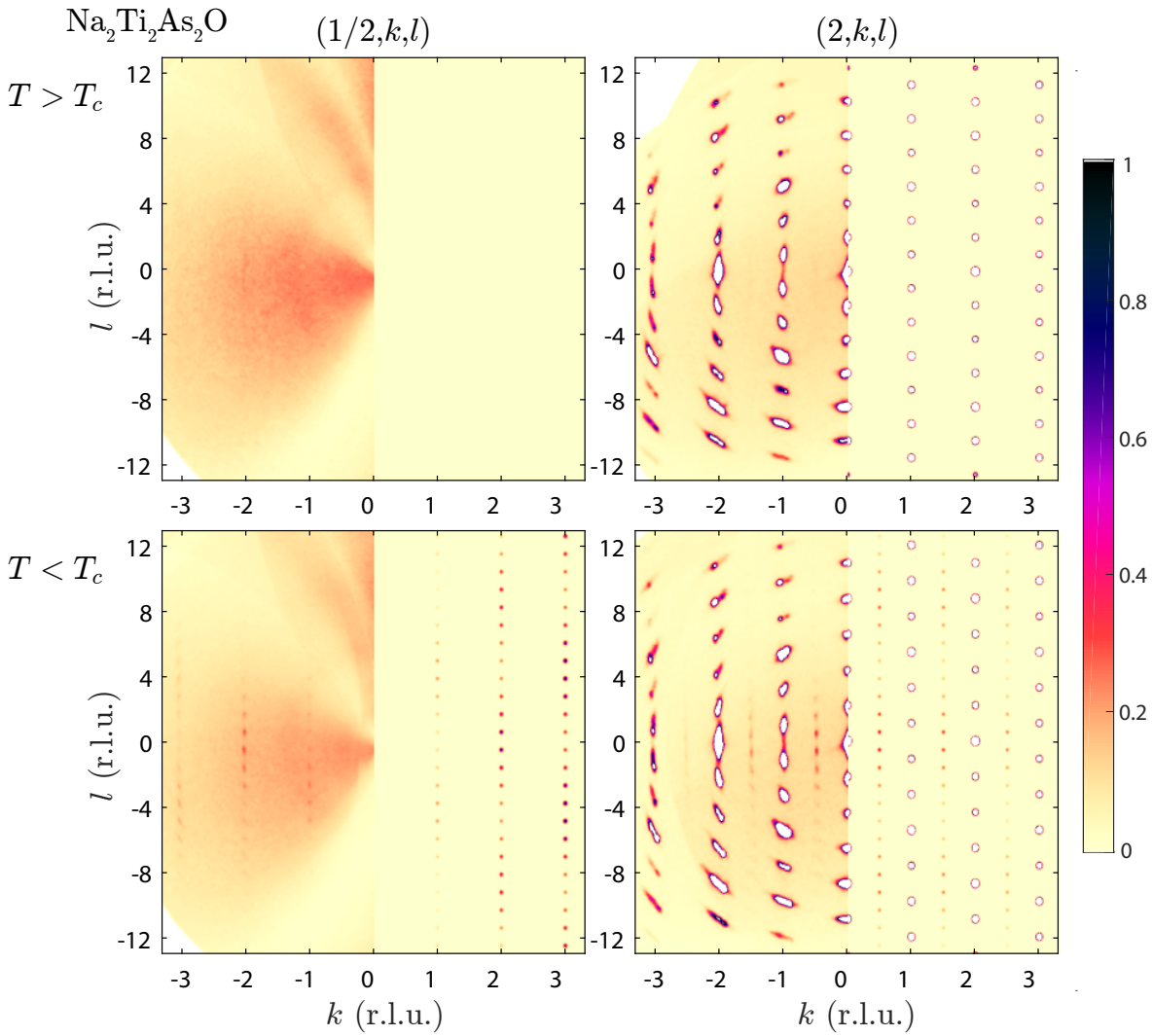

Figure 4.5: Experimental single crystal x-ray diffraction maps (left half-panels) and simulations (right half-panels) in the $(1/2, k, l)$ and $(2, k, l)$ reciprocal space planes of $Na_2Ti_2As_2O$ measured at temperatures above (330 K) and below (230 K) the structural distortion temperature T_{DW}. Intensities are plotted on a log scale.

may be anticipated in systems with weak inter-layer chemical bonding. All Bragg peaks in the highest temperature datasets for both compositions could be indexed in the established $I4/mmm$ space group, and we shall henceforth refer Bragg reflections and reciprocal lattice coordinates to the $I4/mmm$ conventional unit cell. The fitted tetragonal lattice parameters at 300 K are $a = 4.1525(4)$ Å, $c = 16.585(3)$ Å for Pn = Sb and $a = 4.061(1)$ Å, $c = 15.272(4)$ Å for Pn = As, consistent with literature values in both cases [131, 132]. Error bars on structural parameters quoted here and throughout this chapter correspond to uncertainties on the structural fitting and refinement procedure.

Upon cooling below T_{DW} the data reveal weak superstructure reflections appearing

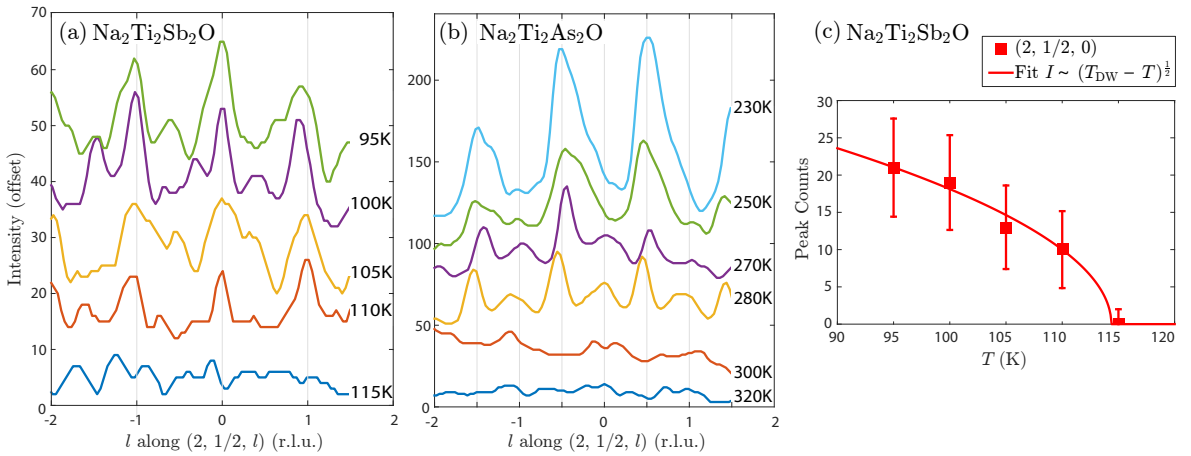

Figure 4.6: Measured x-ray intensity as a function of temperature close to T_{DW} along the cut $(2, 1/2, l)$ for (a) $Na_2Ti_2Sb_2O$ and (b) $Na_2Ti_2As_2O$. Successive cuts have been offset vertically for clarity. (c) Intensity at the maximum of the $(2, 1/2, 0)$ peak of $Na_2Ti_2Sb_2O$. The red line is a best fit of the form $I \sim (T_{\mathrm{DW}} - T)^{1/2}$, intended as a guide to the eye.

at positions with indices $h + k =$ half an odd integer, $l =$ integer for $Pn =$ Sb, while for $Pn =$ As a similar superstructure is observed except the peaks are shifted to half-integer positions along l. This superstructure is the key experimental observation of this chapter.

The precise l positions of the superstructure and its evolution as a function of temperature close to T_{DW} is best seen by taking cuts through the data from the laboratory x-ray diffractometer, as shown in Fig. 4.6. Figure 4.6 (a) shows the superstructure peaks in $Na_2Ti_2Sb_2O$ in cuts along $(2, 1/2, l)$, $-2 \leq l \leq 2$ at several temperatures between 95 and 115 K, Fig. 4.6 (b) shows a similar plot for $Na_2Ti_2As_2O$ at temperatures between 230 and 320 K and Fig. 4.6 (c) follows the $(2, 1/2, 0)$ peak maximum intensity as a function of temperature for $Na_2Ti_2Sb_2O$. The superstructure peaks were detected for temperatures below 115 K ($Pn =$ Sb) and 300 K ($Pn =$ As), consistent with the previously measured anomalies in bulk data at $T_{\mathrm{DW}} \simeq 115$ K ($Pn =$ Sb) and 320 K ($Pn =$ As). Mosaic broadening made it impossible to extract a reliable quantitative temperature dependence for the superstructure peaks for $Pn =$ As.

The superstructures in both materials can be indexed (after averaging over an equal population of equivalent domains) using either a two-$\mathbf{q}$ distortion with commensurate propagation vectors $\mathbf{q}_1$ and $\mathbf{q}_2$, or a single-$\mathbf{q}$ distortion with either of $\mathbf{q}_1$ or $\mathbf{q}_2$, where

$\mathbf{q}_1 = (1/2, 0, l)$ and $\mathbf{q}_2 = (0, 1/2, l)$, with $l = 0$ (Sb) or $l = 1/2$ (As).

In order to characterise the distortion further, displacive distortion modes of the $Na_2Ti_2Pn_2O$ $I4/mmm$ parent crystal structure were calculated using Isodistort [163]. Four irreducible representations of the in-plane commensurate propagation vector $(1/2, 0, 0)$ were determined, labelled $\Sigma1$, $\Sigma2$, $\Sigma3$, and $\Sigma4$ in Miller and Love notation [164], which support finite displacements of all atomic species present. Considering all symmetry-distinct directions of the order parameter, a total of 52 superstructures were found. We were able to constrain this number significantly by testing each against the qualitative features of our data shown in Figs. 4.4 and 4.5. Firstly, reflections extinct by I-centring in the high temperature parent phase at $h + k + l =$ odd positions were observed to remain extinct in the distorted phase. The super-space group must therefore contain a symmetry element that, for all atomic positions, gives a reflection condition equivalent to that of the I-centring translational symmetry of the parent. Secondly, the period-eight modulation observed in the diffraction intensity along l requires displacements of both Ti and Sb ions to be orthogonal to the $I4/mmm$ c-axis. Overall, we were left with just two two-$\mathbf{q}$ modes and two single-$\mathbf{q}$ modes.

The two-$\mathbf{q}$ modes are both described by the space group $Cmcm$ with basis $\{(2, 2, 0), (2, -2, 0), (0, 0, -1)\}$ and origin shift $(3/4, 5/4, -1/4)$ with respect to the parent structure, and within $\Sigma1$ and $\Sigma4$ representations, respectively. The $\Sigma1$ mode describes displacements of the titanium ions parallel to the respective O–Ti–O bond, whereas the $\Sigma4$ mode describes orthogonal displacements. A preliminary comparison of the calculated diffraction patterns due to both these $\Sigma1$ and $\Sigma4$ $Cmcm$ distortion modes to the experimental data indicated that both models can provide reasonable qualitative agreement with the data, but only the $\Sigma4$ model accurately reproduces the relative intensity between groups of reflections along l, when measured at different h or k as seen in Fig. 4.4.

A structural distortion model for $Na_2Ti_2As_2O$ was found via the same strategy, again yielding one two-$\mathbf{q}$ mode and two single-$\mathbf{q}$ modes which agree with the experimental data.

For both compositions the two-**q** mode involves Ti displacements perpendicular to the local O–Ti–O bond, whereas both single-**q** modes involve a mixture of displacements parallel and perpendicular to O–Ti–O bonds. As transverse displacements are expected to be energetically more favourable than longitudinal ones the two-**q** mode is the most likely distortion, so for each material we performed least-squares refinements of the two-**q** mode against the integrated intensities of the best resolved superstructure peaks at the lowest temperatures using the FullProf software package [165].

For Pn = Sb, all reflections from the model distorted structure obey $F_{hkl} = \pm F_{khl}$ where hkl are referred to the reciprocal space of the $I4/mmm$ structure, so that the contributions to intensity at any hkl from the two equivalent orthorhombic domains are equal. It was therefore possible to perform a quantitative refinement by using a single domain and refining an overall scale factor. For Pn = As, it was found that there is no overlap between superstructure reflections from the two equivalent domains so a quantitative fit was again possible by indexing half of the observed superstructure peaks using a single domain.

For both materials, displacements of the Ti and Sb/As sites are required to reproduce all of the qualitative features of the experimental data. A small displacement of the Na sites is also allowed by symmetry and was found to improve the quantitative fit slightly for Pn = Sb, although the fit is not very sensitive to this. Such a displacement would also be allowed for Pn = As, although our data are not of sufficient quality to perform a quantitative refinement in that case.

The x-ray diffraction intensities calculated from the model are shown in Fig. 4.4 for Pn = Sb and in Fig. 4.5 for Pn = As (right half-panels), and a plot of the observed versus calculated squared structure factors in both cases is given in Fig. 4.7. For both materials there is reasonable agreement between the observed and calculated superstructure intensities. In particular, the intensity modulation along $(0, 0, l)$ is well reproduced.

Figure 4.8 shows the in-plane distortion models for both materials and the relation between them and how the layers stack along c, while the relevant displacement pattern

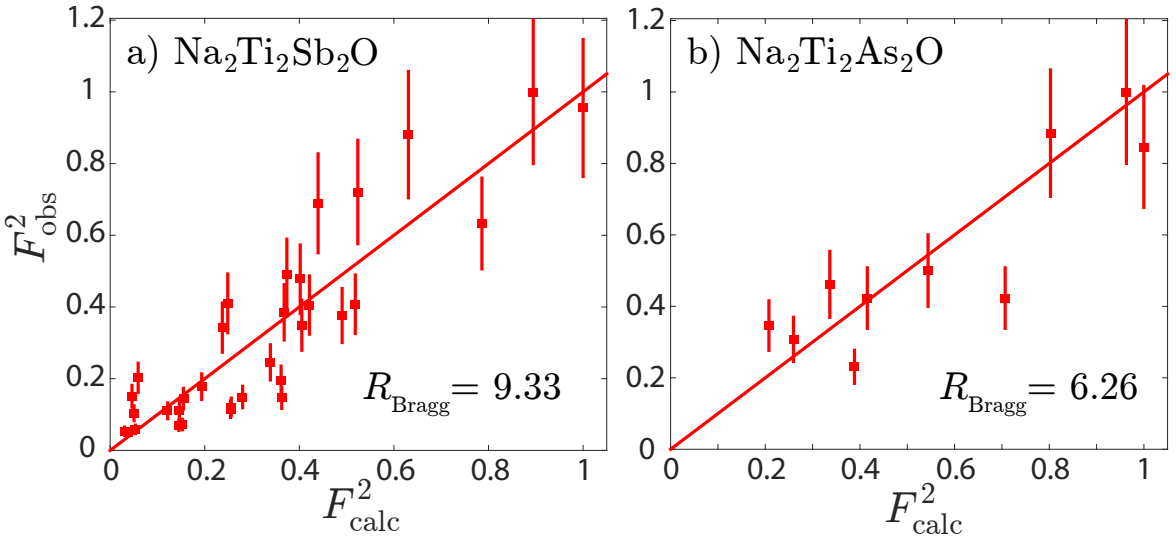

Figure 4.7: Comparison of observed and calculated modulus-squared structure factors for the superstructure peaks of $Na_2Ti_2Pn_2O$. The calculated values are obtained from the distortion models presented in the main text. Error bars represent estimated random errors, but an additional systematic error due to absorption affects some of the points. The R_{Bragg} values are high, but typical of superstructure refinements.

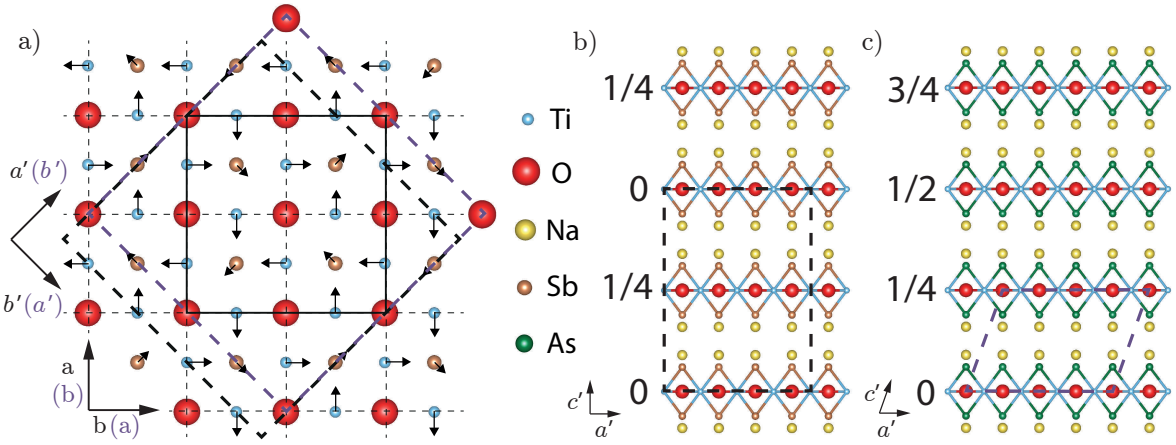

Figure 4.8: Proposed distortion model for $Na_2Ti_2Pn_2O$. (a) ab-plane distortion pattern of the Ti_2Pn_2O units. Thin dashed lines show the $I4/mmm$ unit cell boundaries, thick dashed lines the low temperature $Cmcm$ unit cell boundary and solid lines the unit cell of the Ti_2Pn_2O layer distortion pattern. (b) and (c) show how these layers stack along c, with the numbers beside each Ti_2Pn_2O unit representing the fractional translation along the orthorhombic a'-axis that relates the distortion pattern in that layer to the distortion pattern in the base layer. Black and purple dashed lines mark the unit cells of the distorted structures for Pn = Sb and As respectively.

Pn = Sb $Cmcm$	x	y	z
Na1	0	0.377(3)	0.93054
Na2	0	0.127(3)	0.43054
Na3	0.752(3)	0.125	0.93054
Ti1	0.3668(12)	0.0082(12)	0.25
Ti2	0.6332(12)	0.2418(12)	0.25
Ti3	0.8832(12)	-0.0082(12)	0.25
Ti4	0.1168(12)	0.2582(12)	0.25
Sb1	0	0.376(1)	0.12884
Sb2	0	0.126(1)	0.62884
Sb3	0.751(1)	0.125	0.12884
O1	0	0.625	0.25
O2	0	0.125	0.25
O3	0.75	0.375	0.25

Pn = As $C2/m$	x	y	z
Na1	0.9097	0	0.6389
Na2	0.4097	0	0.6389
Na3	0.1597	0.25	0.6389
Ti1	0.1315(14)	0.1185(14)	0
Ti2	0.8815(14)	0.3685(14)	0
As1	0.810(1)	0	0.2423
As2	0.311(1)	0	0.2423
As3	0.06058	0.24912(17)	0.2423
O1	0	0	0
O2	0	0.5	0
O3	0.25	0.25	0

Table 4.1: Atomic positions in the distorted structure of $Na_2Ti_2Pn_2O$ for Pn = Sb and As from the least-squares fits to our x-ray data shown in the main text.

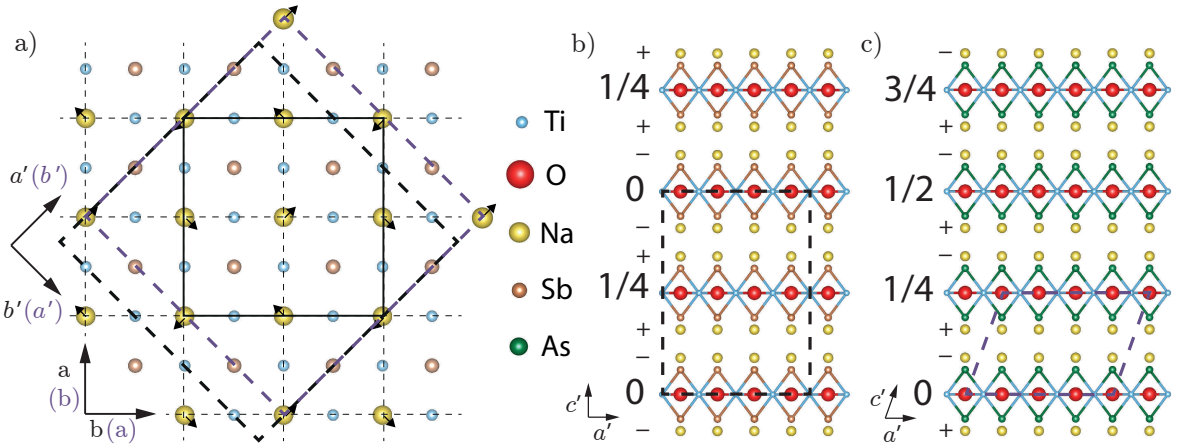

Figure 4.9: The proposed distortion in the Na layers. (a) *ab*-plane distortion pattern for a single Na layer relative to the positions of the Ti and Sb atoms in the nearest Ti_2Pn_2O unit, with thin dashed lines showing the high temperature $I4/mmm$ unit cell boundaries, thick dashed lines the low temperature unit cell boundary and solid lines the unit cell of the Ti_2Pn_2O layer distortion pattern. (b) and (c) show how these layers stack, with + and − beside each Na layer being the sign of the distortion in that layer, where + is defined as the pattern in (a), and the numbers beside each Ti_2Pn_2O unit giving the distortion pattern in that unit as defined in the main text. Black and purple dashed lines mark the unit cells of the distorted structures for Pn = Sb and As respectively.

for Na layers is presented in Figure 4.9. Final positions for all sites in the best-fit distorted structures can be found in Table 4.1. The in-plane displacement pattern of a layer of Ti_2Pn_2O units depicted in Fig. 4.8(a), which is the same for both compounds, is a 2×2 superstructure with the most significant distortion being an in-plane shift of all the Ti atoms perpendicular to the Ti–O nearest-neighbour bonds. The magnitude of the shift is found to be about 0.14 ± 0.03 Å for Pn = Sb and 0.10 ± 0.03 Å for Pn = As. The Pn sites immediately above and below each Ti_2O plaquette undergo a smaller in-plane distortion ($\simeq 0.012$ Å in both cases). Best agreement with experiment for Pn = Sb is obtained when the Na layers are allowed to distort slightly (by $\simeq 0.025$ Å) such that every Na atom moves parallel to the nearest Pn immediately above/below it along the c axis (Fig. 4.9). The fit was not very sensitive to the size of the Na distortion, however.

In the distorted phase the isolated Ti_2Pn_2O layer has 4-fold axes through half of the O sites, which plausibly explains why the a and b lattice parameters remain virtually the same [131]. The 4-fold axes do not coincide between layers upon stacking in the c direction, so the three-dimensional superstructures do not have 4-fold symmetry. For

Pn = Sb, the superstructure within one Ti_2Sb_2O layer displaces first by $\mathbf{t}$ and then by $-\mathbf{t}$, where $\mathbf{t} = (1/2, 1/2, 1/2)$ in $I4/mmm$. The resulting structure is orthorhombic with space group $Cmcm$ and lattice vectors $\mathbf{a}' = 2(\mathbf{a} + \mathbf{b})$, $\mathbf{b}' = 2(\mathbf{a} - \mathbf{b})$ and $\mathbf{c}' = \mathbf{c}$, see Figs. 4.8 (a) and (b). In the case of Pn = As, each layer is displaced by $\mathbf{t}$ relative to the one below resulting in a monoclinic structure with space group $C2/m$ and lattice vectors $\mathbf{a}' = 2(\mathbf{a} - \mathbf{b})$, $\mathbf{b}' = 2(\mathbf{a} + \mathbf{b})$ and $\mathbf{c}' = \frac{1}{2}(-\mathbf{a} + \mathbf{b} + \mathbf{c})$, Fig. 4.8 (c). The distortion in the As compound has period $2c$ along the c axis which is why the superlattice peaks appear at l = half-odd integer positions (half-even integer reflections are absent because the distortion of a Ti_2As_2O unit undergoes a phase shift of π upon translation by c along the c axis.) The diffraction maps shown in Fig. 4.4 (for Pn = Sb) and in Fig. 4.5 (for Pn = As) are averaged over equal populations of equivalent domains.

The superstructures found here have some features in common with the distortion mode predicted from density functional theory (DFT) by Subedi [152] for $BaTi_2Sb_2O$. Both involve transverse displacements of the Ti atoms relative to the O–Ti–O bond, and the calculated shift of $\simeq 0.14$ Å is very close to that obtained from our model. However, the predicted distortion mode has a $\sqrt{2}a \times \sqrt{2}a$ in-plane unit cell which has a smaller area and different propagation vectors than that obtained here and therefore cannot index some of the superstructure peaks observed in the x-ray pattern, for example the peak at (2, 1/2, 0).

4.3.3 Angle-Resolved Photoemission Spectroscopy

Figure 4.10(a) shows special points in the $k_z = 0$ plane in the reciprocal space of $Na_2Ti_2Sb_2O$. For the $I4/mmm$ parent structure, reciprocal lattice points (all symmetry-equivalent to $\Gamma = (0, 0, 0)$) are marked with filled circles and systematic absences with crosses. At the phase transition into the $Cmcm$ distorted structure determined by x-ray diffraction all crosses ($I4/mmm$ absences) become reciprocal lattice points, as well as the X = (1/2, 0, 0) and M = (1/2, 1/2, 0) points, which are marked with empty circles. According to our model, the X and Γ points become equivalent in the $Cmcm$ structure below T_{DW}, since X becomes the (1, 0, 0) point on the reciprocal lattice of the distorted

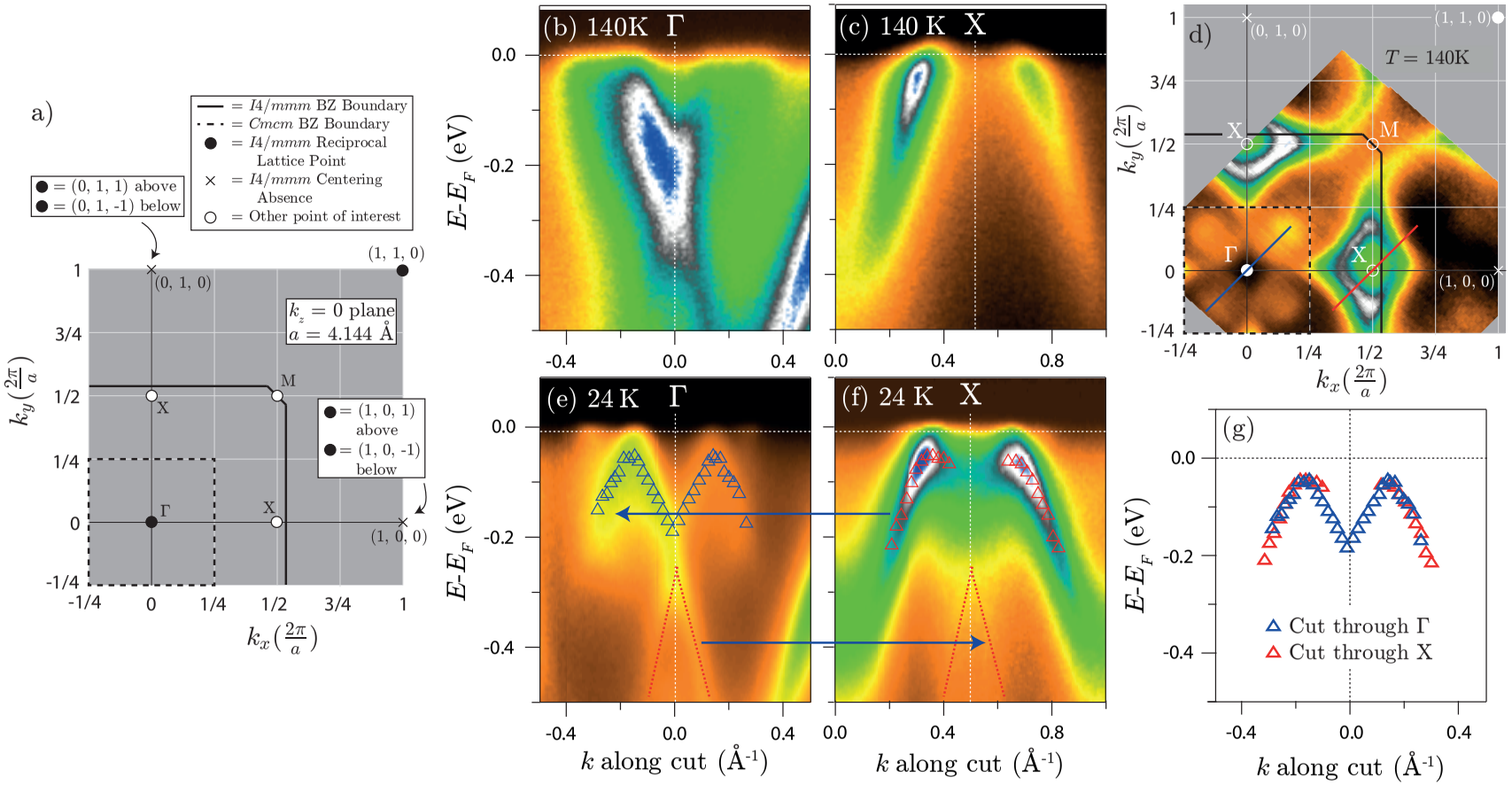

Figure 4.10: (a) $k_z = 0$ plane in the reciprocal space of $Na_2Ti_2Sb_2O$, with the folded ($Cmcm$) and unfolded ($I4/mmm$) Brillouin zone boundaries and the Γ, X and M points referred to in this figure as well as in the main text. (b, c, e and f) ARPES intensity plots of the band dispersions through the Γ and X points at 140 K and 24 K, above and below $T_{DW} \simeq 115$ K, respectively. The momentum locations are indicated as blue (b, e) and red (c, f) lines in panel (d). Blue and red triangles mark the band dispersions at 24 K determined from the energy distribution curves (EDCs). (d) Fermi surface intensity plot recorded at 140 K. (g) Superimposition of the band dispersions in cuts through the Γ [panel (e)] and X [panel (f)] points.

structure. One consequence of this is that any electronic bands which are present at X at high temperature should 'fold' back and appear at Γ in the distorted phase (and similarly the bands at Γ at high temperature should fold to X). Angle-resolved photoemission spectroscopy (ARPES) is very well suited to direct measurements of in-plane electronic band structure for layered materials, so looking for band folding in ARPES experiments presents an independent way to detect the symmetry breaking at T_{DW} and confirm that our distortion model is correct.

ARPES measurements were performed at the PGM (Plane Grating Monochromator) beamline of the Synchrotron Radiation Center (Wisconsin), as well as at the beamline SIS (Surface and Interface Spectroscopy) of the Swiss Light Source at Paul Scherrer Institute (PSI), both equipped with a Scienta R4000 analyzer. The energy and angular resolutions were set at 15-30 meV and 0.2°, respectively. The crystals were cleaved *in situ* and measured in the 24 to 150 K temperature range in a vacuum better than 8×10^{-11} Torr. The ARPES data were recorded using *s* polarized light.

Figure 4.10 (b, c, e and f) show measured band dispersions through the Γ (b, e) and X (c, f) points above ($T = 140$ K) and below ($T = 24$ K) T_{DW}, and Fig. 4.10 (d) shows the observed Fermi surface (FS) in the undistorted state at 140 K. The measured band structure at high temperature agrees with that reported in Ref. [150] as well as with DFT calculations. In previous studies it has been established that there are three FS sheets, one around each of Γ, X and M, all of which are quasi-2D and have approximately square cross-sections. The Γ FS sheet is predicted to show a more pronounced 3D warping, although this has not yet been observed experimentally, perhaps due to limited k_z resolution in the ARPES experiments [150]. We observed all the Γ, X and M FS pockets in our dataset, although we saw only two opposite sections of the squarish FS pocket at M, which we attribute to matrix element effects. Since these three FS pockets are similar in shape at the first order, it is plausible that a CDW with wavevectors $\mathbf{q}_1 = (1/2, 0, 0)$ and $\mathbf{q}_2 = (0, 1/2, 0)$ can develop due to nesting between them as suggested by Tan *et al.* [150], depending on the precise 3D nature and warping of the FS sheets.

At 140 K > T_{DW}, the band structures around Γ and X are clearly different. While an electron band is found at Γ, a hole band is observed at the X point, both of which cross E_{F} directly (Fig. 4.10 (b) and 4.10 (c)). Upon cooling down to 24 K (Fig. 4.10 (e–g)) the Γ and X bands fold onto each other and hybridize near E_{F}, thus gapping the Fermi surface as expected for a CDW gap formation. This band folding and the resulting back-bending can be seen in our data, particularly in Fig. 4.10 (g) where we extract the band positions relative to the nearby high-symmetry point via Energy Distribution Curve (EDC) analysis. The folded bands coincide remarkably well, fully consistent with a CDW with the wavevectors $\mathbf{q}_1$ and $\mathbf{q}_2$. This provides evidence that at least some parts of the Γ and X FS pockets are involved in the CDW gap formation. Whether the M point FS sheet is also involved, and whether the CDW gap on each of these three FS sheets is full or only partial as a function of k_z remain open questions that may be answered via more in-depth ARPES studies.

Our ARPES measurements cannot reliably distinguish whether the CDW exhibits both or only one of the propagation vectors $\mathbf{q}_1$ and $\mathbf{q}_2$ due to the effects of domains in the single-$\mathbf{q}$ case. However if CDWs with $\mathbf{q}_1$ and $\mathbf{q}_2$ do develop simultaneously (which is reasonable since $\mathbf{q}_1$ and $\mathbf{q}_2$ are equivalent in $I4/mmm$) then they are expected to couple to a two-$\mathbf{q}$ lattice distortion with the same propagation vectors $\mathbf{q}_1$ and $\mathbf{q}_2$. We have detected precisely such a distortion in this work, providing a unified picture of a coupled CDW and lattice distortion appearing at $T_{\mathrm{DW}} = 115$ K in $Na_2Ti_2Sb_2O$. ARPES data have not been published for the case of Pn = As, but non-magnetic DFT calculations [147] predict a very similar Fermi surface to Pn = Sb with quasi-two-dimensional (2D) Fermi sheets around the Γ, X and M points. Nesting vectors of the form $\mathbf{q}_1 = (1/2, 0, l)$ and $\mathbf{q}_2 = (0, 1/2, l)$ for some l leading to associated CDWs coupled to the lattice distortion are therefore plausible in this case too.

4.3.4 Subsequent Works

Following the completion and publication of the work presented in this chapter some other papers have appeared on these materials. Particularly noteworthy is Ref. [166],

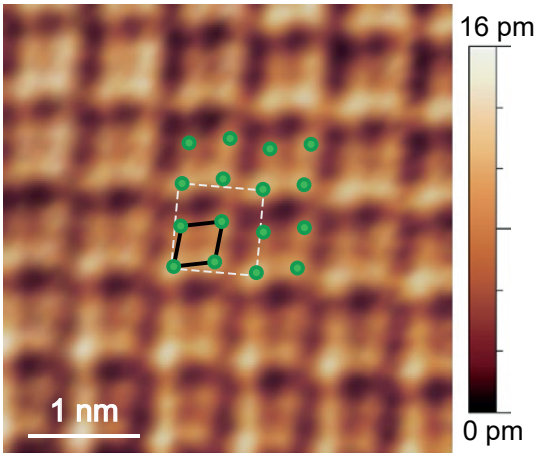

Figure 4.11: An STM image taken in a defect-free area of the Na-terminated surface of a cleaved single crystal of $Na_2Ti_2Sb_2O$, reproduced from Ref. [166]. Green dots mark the locations of Na atoms, with the black lines indicating the distorted lattice and white dashed lines marking the unit cell of the 2 x 2 superstructure.

a Scanning Tunnelling Microscopy (STM) study on $Na_2Ti_2Sb_2O$ in which the authors directly image the atomic displacements on the Na-terminated surface of a cleaved single crystal. The observed Na displacement pattern matches exactly the two-**q** distortion found in the work presented in this chapter, albeit with a larger magnitude of Na displacement which can plausibly be explained as a surface effect.

Two further phonon DFT studies have also appeared [167, 168] which reproduce most of the significant features seen here including a CDW and lattice distortion with one or both of $\mathbf{q}_1$ and $\mathbf{q}_2$.

4.4 Summary

The identification of the DW transition in the titanium oxypnictides as a lattice distortion coupled to a CDW solves the puzzle of the nature of this transition and provides a complete determination of the low temperature ordered phase including the periodicity, symmetry and lattice distortion mode. Fermi surface nesting assists the CDW to form, and the opening of a gap on nested parts of the Fermi surface explains the increase in resistivity and drop in magnetic susceptibility observed at T_{DW}. The observed lattice instability implies a strong electron-phonon coupling for at least this one mode, which points towards a conventional phonon-mediated mechanism for the superconduct-

ing phase found in doped $BaTi_2Sb_2O$. However, given that superconductivity appears upon suppression of the CDW transition, unconventional mechanisms involving charge fluctuations, similar to that proposed in Ref. [127] for the copper oxide superconductors, cannot be ruled out. The results provide a new impetus for theoretical models of superconductivity in this system.

Chapter 5

$J_{\text{eff}} = 0$ ground state and defect-induced spin glass behaviour in the pyrochlore osmate $Y_2Os_2O_7$

In this chapter I present a detailed study of the $5d$ osmate $Y_2Os_2O_7$ via a wide variety of experimental techniques. Interest in compounds containing ions in the $5d^4$ electronic configuration like $Y_2Os_2O_7$ has developed in recent years following the discovery of non-zero magnetic moment in the perovskite iridates A_2YIrO_6 (A = Sr, Ba). The magnetic ions in these materials have a nominal non-magnetic $J_{\text{eff}} = 0$ state in the single-ion limit, leading to proposals of novel co-operative mechanisms involving the condensation of magnetic excitons to explain the unexpected magnetism. There has, however, been no definitive experimental confirmation of this and further studies in some compositions indicated that the magnetism is actually related to disorder or extrinsic effects in experimental samples.

$Y_2Os_2O_7$ was the subject of one recent study which observed a non-zero magnetic moment and spin-glass behaviour, however prior to my work the origin of the magnetic moment was unclear. It represents a promising candidate for the realisation of excitonic magnetism since the OsO_6 octahedra are corner-sharing, meaning the magnetic superex-

change between Os sites is expected to be quite strong, one of the key requirements of theories of excitonic condensation.

By combining results from a variety of experimental techniques including AC and DC magnetisation measurements, μSR, polarised neutron scattering and RIXS, I have been able to establish that the magnetism in $Y_2Os_2O_7$ is very likely to be due to large magnetic moments located on a small fraction ($\lesssim 5\%$) of the Os sites in the sample, likely related to microscopic crystalline disorder. The majority of Os sites exhibit the $J_{\text{eff}} = 0$ non-magnetic state, and I was able to measure their single-ion excitation spectrum and show that it matches the results of single-ion calculations. I also studied the dynamics of the spin freezing, showing that at low temperature some areas of the sample remain non-magnetic and that some of the spins in the magnetic parts of the sample remain dynamic, which may indicate clustering of the magnetically active Os sites.

The results and analysis presented in this chapter are the subject of a paper which is under review for the journal Physical Review B.

I am grateful to my collaborators on this project including members of the group of Youguo Shi at the Beijing Institute of Physics who prepared the sample, C. V. Topping who helped perform the high field magnetisation measurements, F. K. K. Kirschner who performed the μSR simulations and M. C. Rahn, A. J. Princep, H. Jacobsen and A. T. Boothroyd from my group in Oxford who helped perform the μSR, polarised neutron scattering and RIXS measurements.

5.1 Introduction

In the single-ion picture, octahedrally coordinated transition-metal ions with a d^4 electronic configuration, such as Os^{4+} and Ir^{5+}, are expected to have a non-magnetic singlet ground state in both the strong spin-orbit and strong Hund's coupling limits. For strong spin-orbit coupling, the t_{2g} levels are split into a fully-filled $j_{\text{eff}} = 3/2$ quadruplet and an empty $j_{\text{eff}} = 1/2$ doublet yielding an overall $J_{\text{eff}} = 0$, while for strong Hund's coupling each site is in a $S = 1$, $L_{\text{eff}} = 1$ state with L_{eff} and S coupled together under the

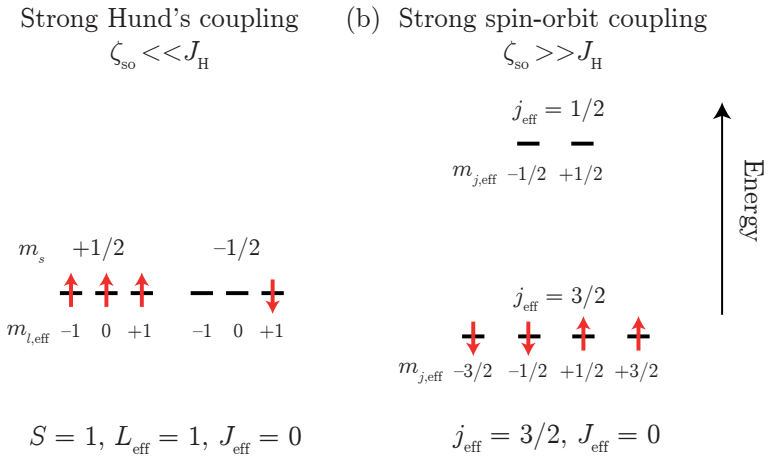

Figure 5.1: The arrangement of electrons among single-electron states in the t_{2g} manifold for the d^4 configuration in (a) the strong Hund's coupling and (b) the strong spin-orbit coupling limits.

spin-orbit interaction to form also a $J_{\text{eff}} = 0$ state, as shown in Fig. 5.1.

Such materials have been studied since the 1960s [174], and although many are non-magnetic there are cases in which a magnetic moment and possibly magnetic ordering is nevertheless observed experimentally [169–171, 173, 175–179] with several different novel mechanisms being proposed to explain this [172, 180–182]. Notable examples which have been studied recently include the double perovskite iridates $A_2\text{YIrO}_6$ (A = Sr, Ba) [169, 170, 177] and the pyrochlore osmates $R_2\text{Os}_2\text{O}_7$ (R = rare earth) [173].

For the iridates some theories proposed that a novel excitonic mechanism related to the interplay of spin-orbit coupling and superexchange was behind the magnetic state [180–182], however it has been pointed out that the superexchange interaction is probably not strong enough in these materials to induce excitonic magnetism since the IrO_6 octahedra are isolated from one another [10]. Instead, the observed moment has been ascribed to extrinsic explanations such as paramagnetic impurities [170, 171] or antisite disordered clusters [172].

The pyrochlore osmates provide more promising candidates for excitonic magnetism since the OsO_6 octahedra form a corner-sharing network, meaning the superexchange is expected to be much larger. Less work has been done on this family of materials however, with one experimental study on the R = Y and Ho pyrochlores observing non-zero moments in both cases [173].

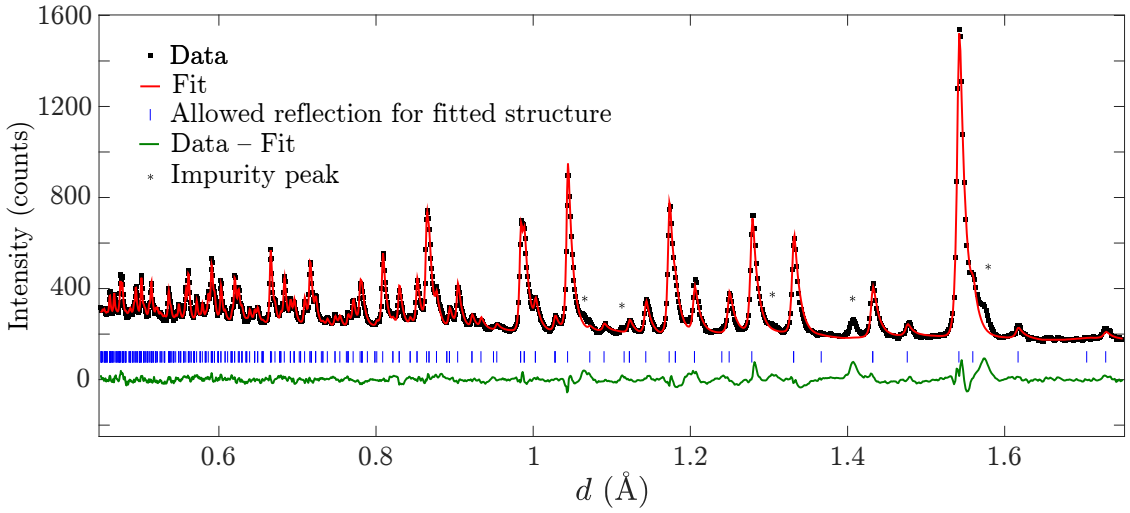

Figure 5.2: Elastic neutron scattering data from the $Y_2Os_2O_7$ sample at 200 K as a function of $d = 2\pi/Q$ where Q is the momentum transfer. Black squares are experimental data and the red line is the fitted profile after structural refinement (corresponding to the 200 K parameters in Table 5.1). The green line beneath the ticks is a difference plot between the data and the fit. Blue tick marks show the expected locations of peaks due to the main $Y_2Os_2O_7$ phase while black asterisks indicate impurity peaks. When regions in which impurity peaks are present are excluded, the Bragg R-factor for this fit is 6.54.

The aim of this work was to establish the origin of the non-zero magnetic moment in $Y_2Os_2O_7$ and study the single-ion physics of the Os site, as well as examining the dynamics of the spin-freezing transition observed previously.

5.2 Sample Characterisation

A 5.2g polycrystalline sample of nominal composition $Y_2Os_2O_7$ was synthesised through a conventional solid-state reaction. A stoichiometric mixture of Y_2O_3 and OsO_2 was ground and sealed in an evacuated quartz tube, then the tube was heated up to 773 K and left at this temperature for 24 hours. The production was reground and pressed into a pellet and sealed in a new quartz tube under vacuum. The quartz tube was heated slowly up to 1173 K and kept at this temperature for 2 days and the target $Y_2Os_2O_7$ phase obtained after shutting off the furnace.

Elastic neutron scattering measurements performed on the GEM beamline at the ISIS facility [183] allowed for a full structural refinement as shown in Fig. 5.2 and Table 5.1, yielding lattice parameter $a = 10.225(1)$ Å. Superficially, the refinement indicates

Temperature (K)	a (Å)	x_{48f}	O_{48f} Occupancy (%)
200	10.225(1)	0.3352(2)	98.7(5)
100	10.222(1)	0.3354(2)	98.5(8)
2	10.220(1)	0.3355(2)	98.5(8)

Temperature (K)	B_{iso}(Os) (Å^2)	B_{iso}(Y) (Å^2)	$B_{\text{iso}}(O_{48f})$ (Å^2)	$B_{\text{iso}}(O_{8b})$ (Å^2)
200	0.46(2)	0.84(4)	0.91(3)	0.78(7)
100	0.42(3)	0.71(5)	0.83(5)	0.70(9)
2	0.41(3)	0.68(5)	0.81(5)	0.67(9)

Table 5.1: Refined structural parameters for $Y_2Os_2O_7$ in the space group $Fd\bar{3}m$. There is only one free fractional coordinate in this structure for the O on the $48f$ site (x_{48f}), corresponding to trigonal distortion of oxgygen octahedra around the Os site. Zero trigonal distortion corresponds to $x_{48f} = 5/16 = 0.3125$.

an oxygen deficiency of approximately 1.5 %, but this result is not reliable as there is an uncertainty of around 2 % in the neutron scattering length of Os [184]. The only fractional coordinate in this structure which is not constrained by symmetry is the $48f$ oxygen site x-coordinate which we find to be $x_{48f} = 0.3352(2)$ at 200 K. For reference, zero trigonal distortion of the OsO_6 octahedra corresponds to $x_{48f} = 5/16 = 0.3125$, with $x_{48f} > 5/16$ indicating trigonal compression of the octahedra in this case. As depicted in Fig. 5.3, this structure contains a network of corner-sharing tetrahedra with OsO_6 octahedral complexes located at each each vertex of the tetrahedron. All pairs of neighbouring OsO_6 units share one oxygen site, and in our sample the octahedra are trigonally distorted as shown in Fig 5.3 (d).

The structural parameters are similar but not identical to those reported in Ref. [173], with the variation possibly related to different levels of microscopic disorder resulting from the different sample synthesis routes. A small number of low-intensity peaks from an unidentified impurity phase can also be seen. These peaks could not be indexed by Y, Os, any known oxide of Y or Os or any material expected to be close to the beam path. Based on the intensity of the strongest peaks in the neutron scattering spectrum we estimate that the impurity is on the level of $\lesssim 6\%$ and note that due to the small

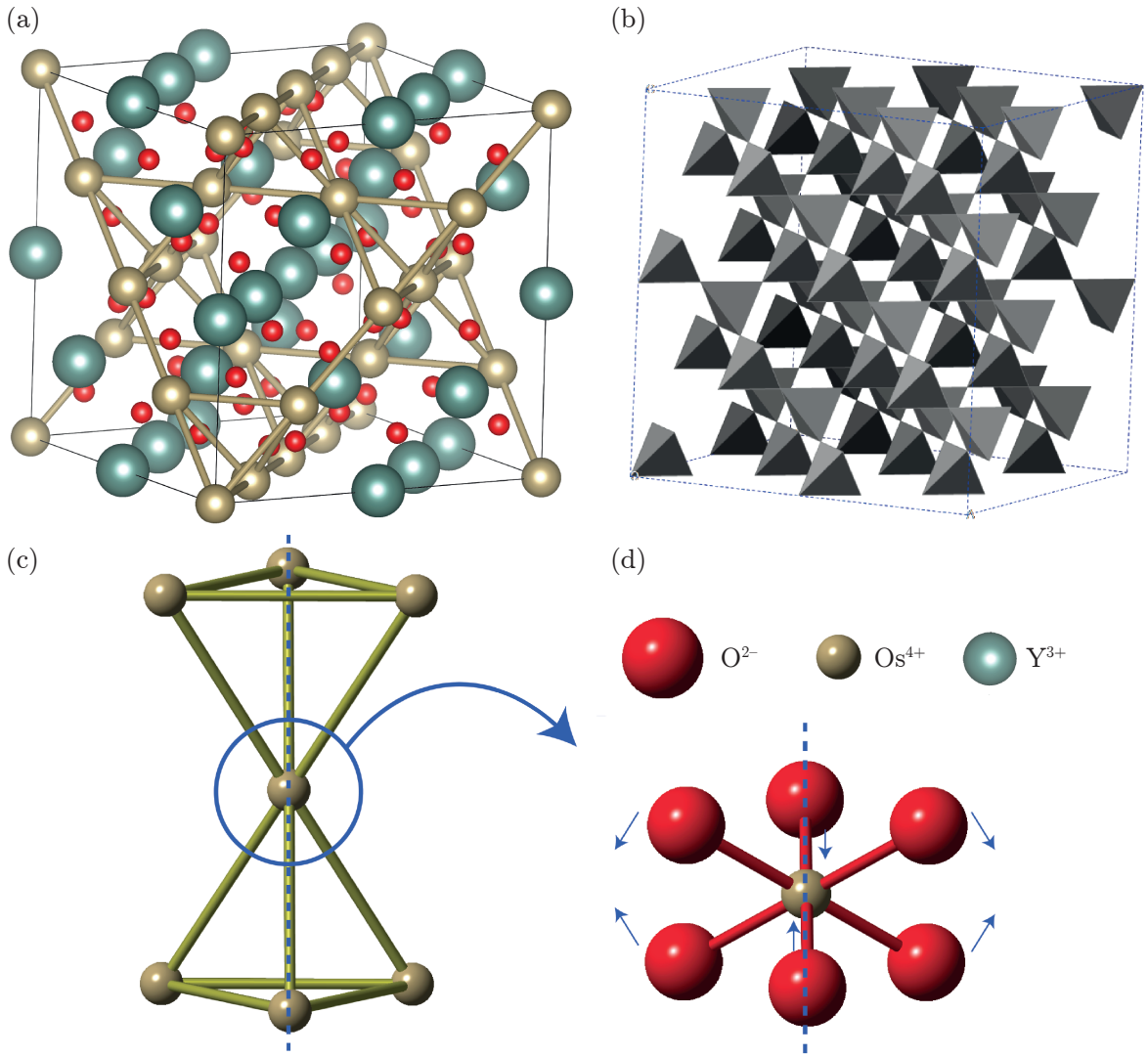

Figure 5.3: (a) The unit cell of the pyrochlore crystal structure of $Y_2Os_2O_7$. (b) Representation of the corner-sharing Os octahedra over several unit cells. (c) Two of the Os tetrahedra, showing the axis of the trigonal distortion. (d) Representation of the trigonal distortion of single OsO_6 unit.

volume fraction the μSR, RIXS and specific heat measurements discussed in this work are assumed not to be very sensitive to the impurity. The potential effects of the impurity on magnetisation will be discussed in Section 5.4.1.

5.3 Experimental Details

DC magnetisation measurements up to 16 T and specific heat measurements were performed on a Quantum Design Physical Property Measurement System (PPMS) while AC and DC magnetisation measurements up to 7 T where performed on a Quantum

Design Magnetic Property Measurement System (MPMS). Muon spin relaxation (μSR) measurements were performed in a ^{4}He cryostat (3.8–225 K) and a dilution refrigerator (92 mK to 3.8 K) on the MuSR beamline at the ISIS Pulsed Muon Facility [185] on part of the powder sample packed in a packet made from 25 μm thick silver foil mounted on a silver backing plate. An additional measurement on the same sample was performed in a ^{4}He cryostat on the GPS spectrometer at the Paul Scherrer Institute (PSI) to check the low-decay-time spectrum at 1.5 K. Resonant Inelastic X-ray Scattering (RIXS) data were taken on a pressed pellet of the sample on the beamline ID20 at the European Synchrotron Radiation Facility. Polarised neutron scattering measurements were performed using the xyz-polarisation method on the beamline D7 at the ILL neutron source [58] in a ^{4}He cryostat with the sample mounted in annular geometry inside an Al can. Data were normalised using the scattering from a standard vanadium sample and polarisation correction performed using a quartz rod of similar dimensions to the $Y_2Os_2O_7$ sample, while background subtraction was performed using measurements of a sample holder and a cadmium sample.

5.4 Results

5.4.1 DC Magnetisation

DC magnetic susceptibility data (Fig. 5.4) show Curie-Weiss-like behaviour over a large temperature range with departures below about 60 K and a significant splitting between field-cooled and zero-field-cooled data below about 5 K. A fit to the form $\chi = \chi_0 + N_\mathrm{A} n \mu_\mathrm{eff}^2 / 3 k_\mathrm{B} (T - \theta)$ for temperatures above 70 K where χ is the DC susceptibility expressed in SI units ($\mathrm{m^3\,mol^{-1}}$), n is the fraction of Os sites which exhibit a magnetic moment and μ_eff is the effective moment due to each of these Os sites yields $\sqrt{n}\mu_\mathrm{eff} = 0.417(1)\,\mu_\mathrm{B}$, a Weiss temperature of $\theta = -2.1(4)$ K and a temperature-independent background susceptibility $\chi_0 = 1.126(1) \times 10^{-5}\,\mathrm{m^{-3}\ mol^{-1}}$. The formula unit for all molar quantities here and throughout this work is $Y_2Os_2O_7$ unless otherwise stated. The origin of the significant temperature-independent component of the suscep-

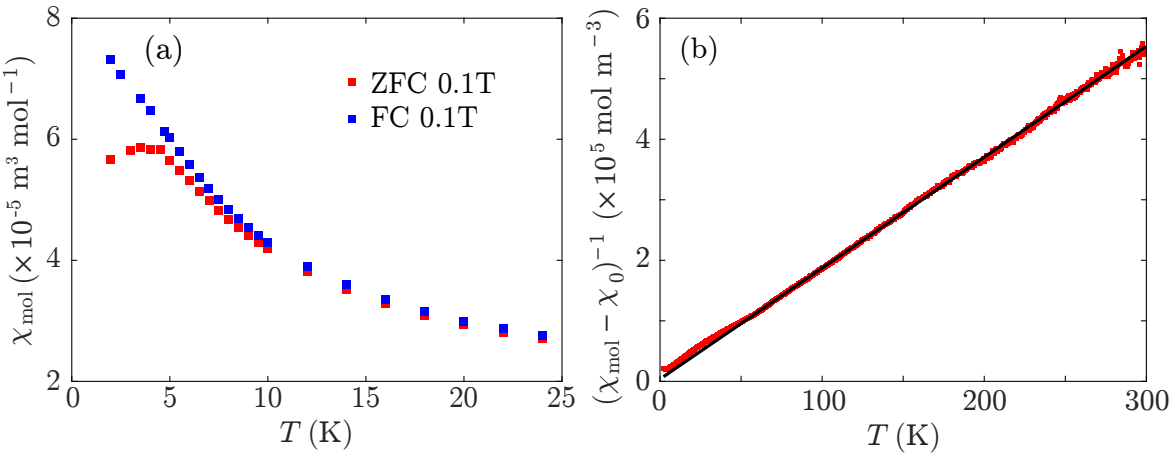

Figure 5.4: (a) DC magnetic susceptibility of polycrystalline $Y_2Os_2O_7$. Data were taken using a 0.1 T measurement field, after cooling from room temperature in the measurement field (FC, blue squares) and in zero field (ZFC, red squares). (b) $(\chi_{\text{mol}} - \chi_0)^{-1}$ as a function of temperature, where χ_0 is the background susceptibility obtained in a Curie-Weiss fit of the form $\chi = \chi_0 + N_{\text{A}} n \mu_{\text{eff}}^2 / 3k_{\text{B}}(T - \theta)$ where n is the fraction of Os sites which exhibit a spin. The black line is the result of this Curie-Weiss fit, showing good agreement with the data down to around 60 K. The resulting fit parameters are $\sqrt{n}\mu_{\text{eff}} = 0.417(1)\,\mu_{\text{B}}$, $\theta = -2.1(4)$ K and $\chi_0 = 1.126(1) \times 10^{-5}\,\text{m}^{-3}\,\text{mol}^{-1}$.

tibility will be discussed in more detail in Section 5.5.3 in light of our RIXS results.

The observed DC magnetic susceptibility appears qualitatively very similar to that measured in Ref. [173], differing only by a constant factor close to 1. The sample measured in that work contained 7% Y_2O_3 and 10% OsO_2 impurities and the authors do not mention any unknown impurity similar to the one seen here. The close similarity between the two samples from different sources and containing different secondary phases (albeit at low levels) indicates that the dominant features in the measured magnetisation are from the $Y_2Os_2O_7$ phase. We will provide further evidence that the impurity does not affect the measured magnetisation in Section 5.5 via in-depth analysis of our μSR results.

Magnetisation data taken up to 16 T at 2.5 K (Fig. 5.5 (a)) shows a small hysteresis (inset to figure). Due to the significant van-Vleck susceptibility in this material, the moment μ is expected to be linear in H at high enough fields once the Curie-Weiss-like moments have reached saturation. Looking at the raw data, the moment does not saturate up to the maximum field of 16 T, however it does appear to be approaching saturation. If we subtract off a van-Vleck contribution corresponding to $\chi_0 = 1.126(1) \times$

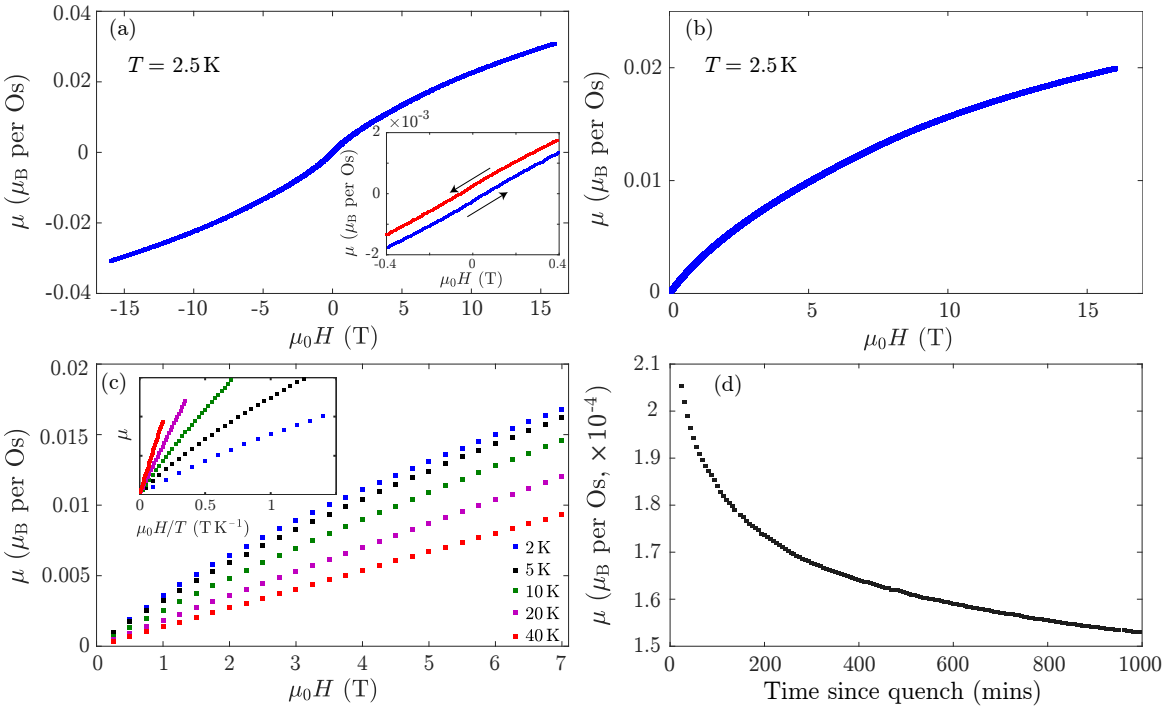

Figure 5.5: (a) Magnetisation μ of $Y_2Os_2O_7$ at 2.5 K as a function of applied field $\mu_0 H$. A small amount of hysteresis is seen between field up and down sweeps (inset). (b) The positive-field part of the dataset in (a) after subtraction of a linear van-Vleck contribution $\chi_0 = 1.126(1)\times 10^{-5}\,\mathrm{m}^{-3}\,\mathrm{mol}^{-1}$, consistent with the results of our Curie-Weiss fitting. (c) The temperature dependence of the magnetisation between 2 and 40 K. The inset shows the same data as a function of $\mu_0 H/T$ to demonstrate the lack of H/T scaling expected for a paramagnet. (d) Remanent magnetisation of $Y_2Os_2O_7$ at 2 K after quenching from a field of 7 T. In order to obtain this data the superconducting magnet was ramped down from 7 T as quickly as possible over the course of around 6 minutes with the starting time $t = 0$ being when the field began to ramp down. The magnet was then heated up above its superconducting transition temperature and the first data point taken once the magnet reached its normal state.

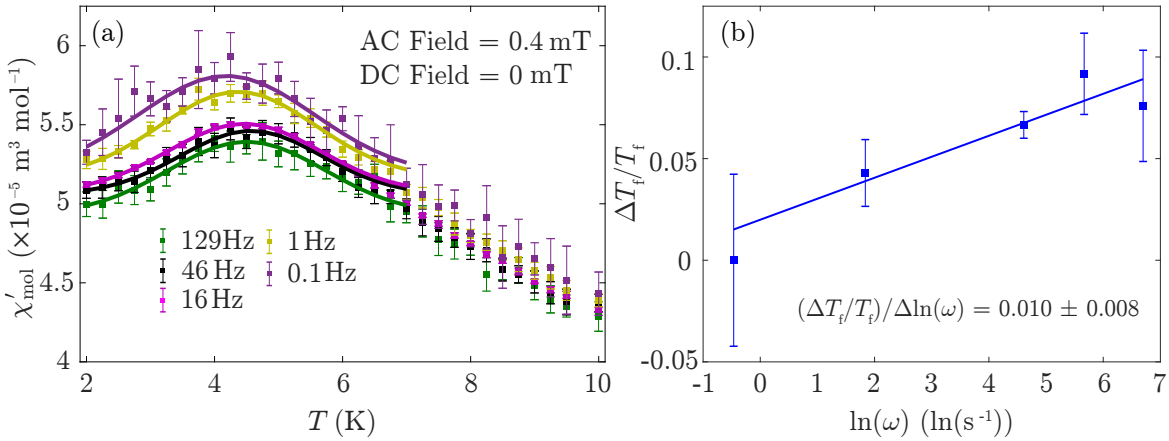

Figure 5.6: (a) AC magnetic susceptibility of $Y_2Os_2O_7$ powder. Data were taken using a 0.4 mT AC measurement field and zero DC field after cooling from room temperature in zero field. χ'_{mol} is the real part of the AC molar susceptibility. Solid lines are fits to a Gaussian peak plus a constant background in the region around 4 K to find the peak position for plotting in (b) and to emphasise its shift to lower temperature with decreasing frequency. (b) Fractional change in the peak position in the real part of the AC magnetic susceptibility $\Delta T_f/T_{f,0} = (T_f(\omega) - T_f(\omega \to 0))/T_f(\omega \to 0)$ as a function of $\ln(\omega)$, where $T_f(\omega)$ is taken from the fitted peaks in (a). The blue line is the best linear fit yielding a gradient $\Delta T_f/T_f/\Delta\ln(\omega) = 0.010 \pm 0.008$, comparable to that seen in a typical spin glass [3].

10^{-5} m^{-3} mol^{-1} from our Curie-Weiss fitting (Fig. 5.5 (b)), it appears that the saturated moment due to the paramagnetic component is unlikely to be greater than about 0.04 μ_B per Os in the whole sample.

The temperature dependence of the magnetisation curves (Fig. 5.5 (c)) shows that the moment does not show normal paramagnetic behaviour at low temperature. Instead, it is close to temperature-independent at the lowest temperatures (2–5 K) and shows a gradually increasing thermal response above this, although ideal paramagnetic behaviour according to the Brillouin function (i.e. μ being a function of B/T only) is not recovered up to 40 K.

The sample also shows a small but observable remanent magnetisation and time-dependent relaxation when quenched from 7 T (Fig. 5.5 (d)) at 2 K, with the moment not decaying fully even after many hours. The curve does not fit to a single exponential, consistent with a spread of decay times.

5.4.2 AC Magnetisation

In the real part of the AC susceptibility (Fig. 5.6 (a)) a clear peak is seen close to the previously proposed spin freezing temperature $T_f \simeq 5\,\mathrm{K}$ [173], with the peak moving to lower temperatures and having a higher maximum χ' at lower frequencies. This separation of peaks at different frequencies shows that there are slow magnetic dynamics in the 0.1–1000 Hz range. More quantitatively, we find the shift of this peak with frequency is consistent with a linear relationship

$$\Delta T_f / T_{f,0} = (T_f(\omega) - T_f(\omega \to 0))/T_f(\omega \to 0) = F\Delta(\ln \omega) \tag{5.1}$$

with constant $F = 0.010(7)\,(\ln(\mathrm{s}^{-1}))^{-1}$ (Fig. 5.6 (b)), which is within the range $F = 0.001 - 0.08$ found for typical spin glasses [3, 186].

We found that the imaginary part of the AC susceptibility was smaller than the instrumental resolution of the magnetometer used for our measurements at all frequencies and temperatures measured, i.e. $\chi'' \lesssim 10^{-6}\,\mathrm{m}^{-3}\,\mathrm{mol}^{-1}$. This weak χ'' is consistent with the behaviour of known spin glasses and indicates a wide spread of relaxation times [186].

The hysteretic and frequency-dependent effects described here, including the splitting between field-cooled and zero-field-cooled DC magnetisation, AC magnetisation and remanence are all characteristic features of canonical spin glasses and other spin-glass-like pyrochlore systems such as $Y_2Mo_2O_7$ [187, 188].

5.4.3 Heat Capacity

The zero-field specific heat of a pressed pellet made from the above sample is smooth at all temperatures down to 2 K and shows no obvious signature of the spin glass transition or any other magnetic behaviour (Fig. 5.7(a)). A plot of C/T as a function of T^2 (Fig. 5.7(b)) shows that the data do not fit a simple Debye model ($C/T = \gamma + \alpha T^2$) over any measured temperature range.

Remarkably, on applying a large (11 T) magnetic field we find no observable change in the specific heat of $Y_2Os_2O_7$ at any temperature as shown in Fig. 5.7(a). Since such

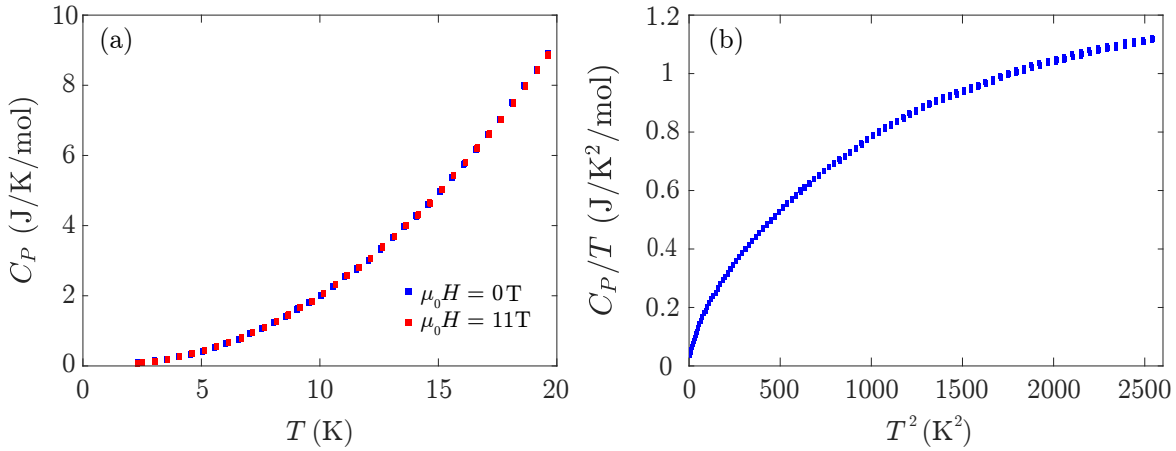

Figure 5.7: (a) Molar specific heat of $Y_2Os_2O_7$ as a function of temperature in zero and high (11T) magnetic field. (b) C/T as a function of T^2 in zero magnetic field for comparison to the Debye model.

a large magnetic field can reasonably be expected to significantly affect the magnetic state – and hence the magnetic component of the heat capacity – it is very likely that the specific heat measured experimentally is almost entirely due to phonons, and any magnetic contribution is unresolvably small at all temperatures.

Although surprising, we find that the lack of an observed magnetic specific heat signal is consistent with the results of the other measurements presented here. The effective moment per Os ($\sqrt{n}\mu_{\text{eff}}$) is quite small and the spin glass state likely has a large amount of residual disorder, so the entropy change associated with the spin-freezing transition may be quite low. Additionally, the release of entropy for typical spin glasses has been observed to be spread over a large temperature range up to around $5\,T_{\text{f}}$ [15], resulting in a very small contribution to the specific heat at any given temperature [189].

Our measurements of $Y_2Os_2O_7$ are consistent with the data presented by Zhou *et al.* in Ref. [173]. However, our conclusion that there is no observable magnetic contribution to the specific heat differs. We therefore performed further heat capacity measurements on a pellet of $Y_2Ti_2O_7$ as a non-magnetic reference sample. For $Y_2Ti_2O_7$, we obtained virtually identical data to Zhou *et al.* up to 30 K. However we find that, after applying the same scaling, the zero-field specific heats of $Y_2Ti_2O_7$ and $Y_2Os_2O_7$ are not the same above 30 K, where any magnetic signal due to spin glass behaviour should be small. The discrepancy between this finding and the conclusions of Ref. [173] indicates that

$Y_2Ti_2O_7$ is not a sufficiently accurate non-magnetic background sample to isolate the small magnetic contribution to the heat capacity.

5.4.4 Muon Spin Relaxation (μSR)

μSR data taken at ISIS shows very little relaxation of the implanted muons at high temperatures $\gtrsim 100\,\mathrm{K}$ (not shown), as expected for a paramagnet, with relaxing behaviour developing gradually on cooling below this point (Fig. 5.8 (a)). The relaxation becomes significantly greater below around 20 K as the spin freezing temperature is approached, although the spectrum does not completely stop evolving even at the lowest measured temperature of 92 mK. This indicates that the evolution of magnetic fluctuations in this system is very gradual, as is typical for spin-glasses. No oscillations are seen at any temperature confirming that there is no long-range magnetic order, and additional datasets at 1.5 and 10 K taken at PSI with much higher time resolution confirm that no oscillatory behaviour has been lost on shorter timescales down to 0.1 μs (Fig. 5.8 (b)). Overall the data is remarkably similar to that seen in canonical spin glasses such as AgMn [16], supporting the assertion that some kind of spin freezing occurs in this material.

In an applied longitudinal field at 0.12 K (Fig. 5.8 (c)), a significant proportion of the relaxation is decoupled at the smallest measured field of 0.02 T, with no observable change between 0.08 T and 0.16 T. Similar longitudinal field dependence is also seen at 2 K. For the case of a static magnetic field B_{stat} at the muon stopping site it has been shown that a longitudinal field $B_{\mathrm{LF}} \gtrsim 10 B_{\mathrm{stat}}$ will completely decouple the muon relaxation [61]. This indicates that there is a small, static component of the internal field.

5.4.5 Polarised Neutron Scattering

Polarised neutron scattering measurements performed using the XYZ-polarisation method at 1.5 and 100 K allowed separation of the cross-sections for coherent nuclear scattering, nuclear spin-incoherent scattering and magnetic scattering, with normalisation to scattering from quartz and vanadium standard samples meaning the cross-sections were

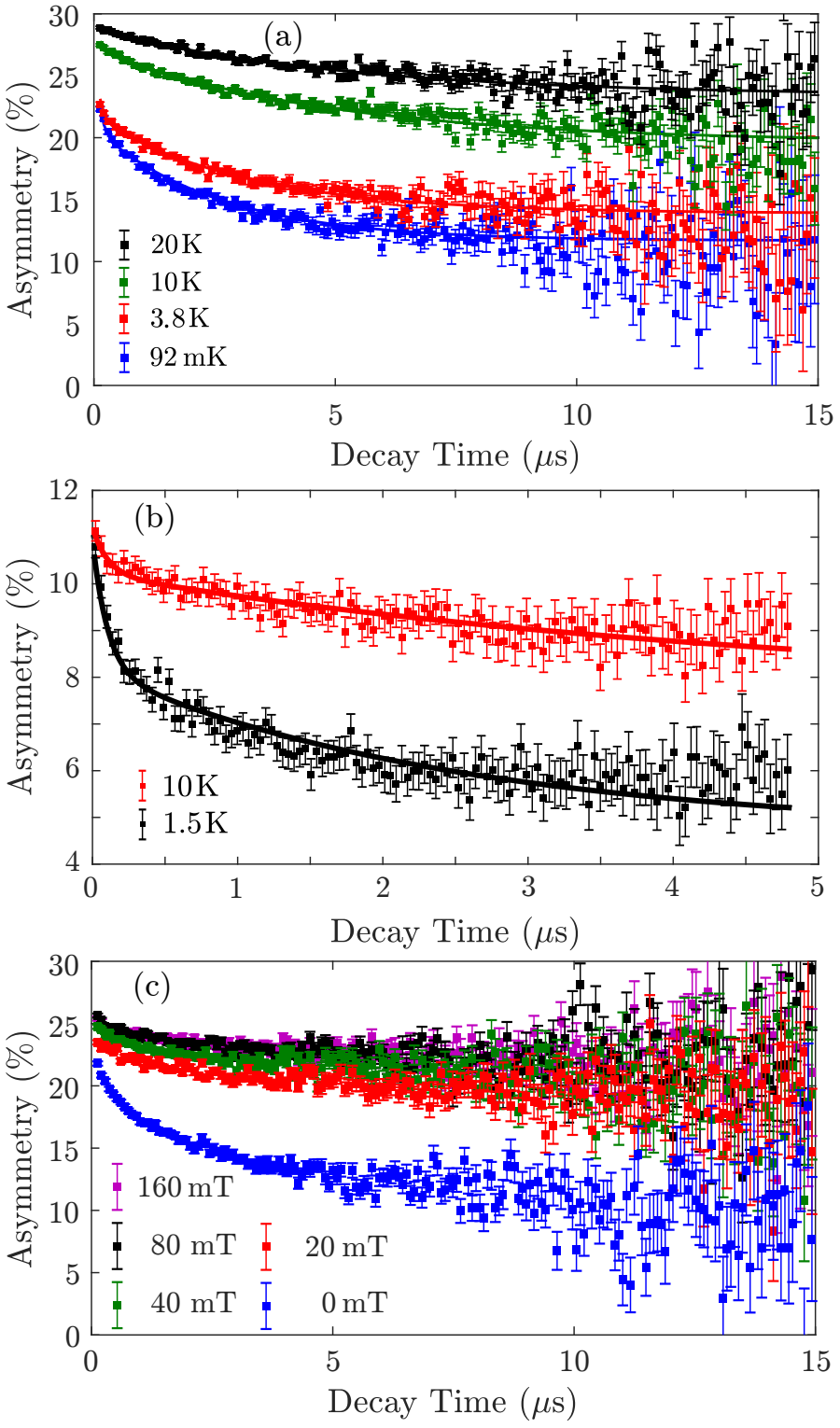

Figure 5.8: (a) Measured muon decay asymmetry as a function of decay time at selected temperatures for polycrystalline $Y_2Os_2O_7$. Datasets at temperatures greater than 3.8 K were recorded in a ^{4}He cryostat while those at 3.8 K and below were taken in a dilution refrigerator. Solid lines represent a double-exponential fit as discussed in Section 5.5.2. (b) Similar spectra to (a) but data taken at a different facility with higher time resolution to show that no structure has been missed in the low decay time region. This data was taken with the beamline's spin rotator switched on, leading to a lower absolute value of the measured asymmetry. (c) Muon decay asymmetry at 0.12 K as a function of applied longitudinal field.

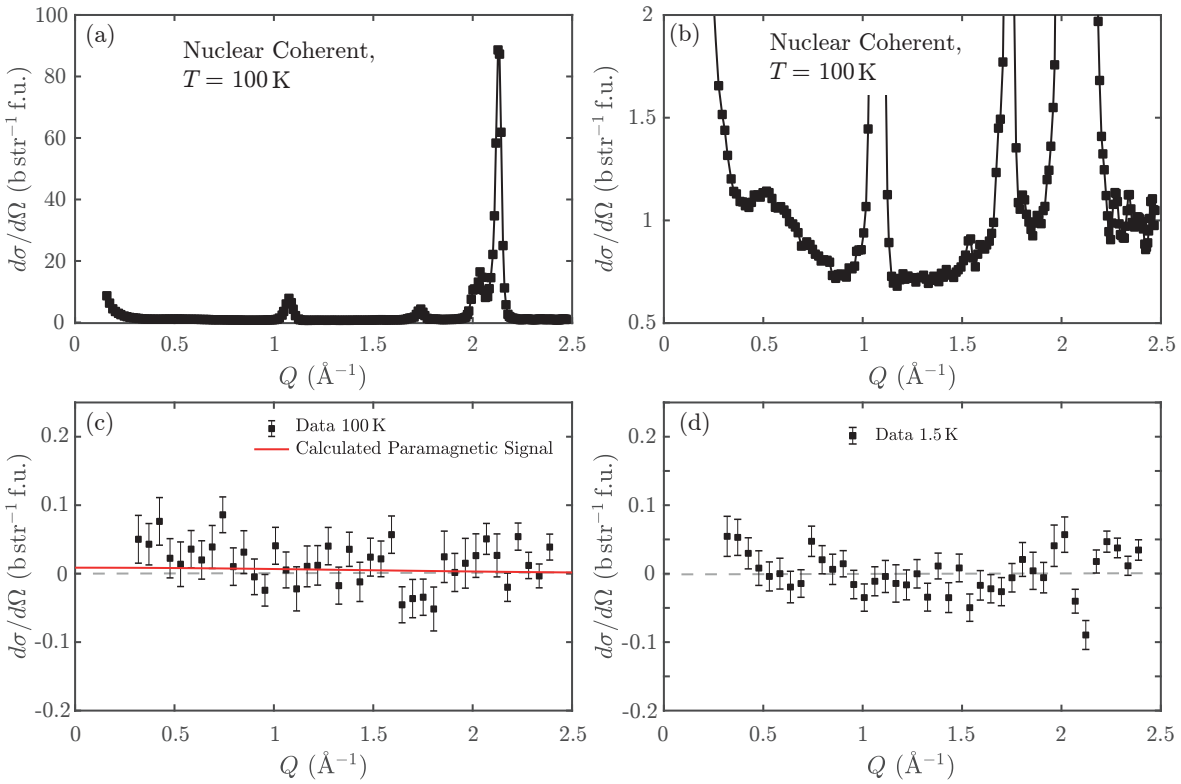

Figure 5.9: Polarised neutron scattering spectra of $Y_2Os_2O_7$ obtained using the XYZ-method. (a) Nuclear coherent cross-section at 100 K. The line is a guide to the eye. (b) Same as (a) but on a different scale to show the diffuse scattering between the Bragg peaks. (c) Magnetic cross-section at 100 K plotted with the calculated paramagnetic signal under the constraint $\sqrt{n}g\sqrt{J(J+1)} = 0.417$ obtained from our DC magnetisation measurements in Section 5.4.1. (d) Magnetic cross-section at 1.5 K.

determined on an absolute scale.

The nuclear coherent cross-section shows all expected Bragg peaks. There is also quite a strong increase in background scattering at very low Q as well as a small, broad enhancement on top of this peaked around $Q = 0.6\,\text{Å}^{-1}$ at both temperatures measured (Fig. 5.9 (a–b)). This corresponds to a correlation length around $d \simeq 10.5\,\text{Å}$ which is similar to the lattice parameter $a = 10.225(1)\,\text{Å}$. Our characterisation measurements indicated an oxygen deficiency $\sim 2\%$, corresponding to approximately one oxygen vacancy per unit cell, so it is plausible that this extra scattering is related to short-range correlations between oxygen vacancies. The general increase in background scattering at low Q has been observed before on this and similar instruments and is likely to be an artefact of the measurement technique; further discussion of this can be found in Ref. [190].

Upon changing temperature to 1.5 K the only difference is a small, approximately

constant enhancement at all Q, which likely corresponds to a temperature-dependent change in the background signal.

There is no observable signal in the magnetic scattering at any Q at either temperature apart from a small negative deviation at $Q = 2.15\,\text{Å}^{-1}$ at 1.5 K (Fig. 5.9 (c–d)). A similar deviation was also seen in the nuclear spin incoherent scattering which should be Q-independent so this is likely not a real magnetic feature.

We have also plotted in Fig. 5.9 (c) the calculated paramagnetic scattering at 100 K according to the equation

$$\frac{d\sigma}{d\Omega} = \frac{2}{3}\Big(\frac{\gamma r_0}{2}\Big)^2 \frac{N}{N_{\text{fu}}}|F(Q)|^2 n g^2 J(J+1) \tag{5.2}$$

[50] where $\frac{d\sigma}{d\Omega}$ is the differential cross-section per formula unit, $N/N_{\text{fu}} = 2$ is the number of magnetic sites per formula unit, $F(Q)$ is the magnetic form factor and $C = \big(\frac{\gamma r_0}{2}\big)^2 = 0.07265\,\text{barn}/\,\mu_{\text{B}}^2$. Applying the constraint $\sqrt{n}g\sqrt{J(J+1)} = 0.417$ from our DC magnetisation measurements (Section 5.4.1) we obtain

$$\frac{d\sigma}{d\Omega} = \frac{4}{3}C|F(Q)|^2 0.417^2. \tag{5.3}$$

Assuming the form factor $F(Q)$ can be closely approximated by the form factor of Os^{4+} as given in Ref. [191], we find that the paramagnetic scattering at 100 K would have been unobservable with the available experimental statistics.

The lack of any observable signal at 1.5 K indicates that correlations between spins at any given Q are relatively weak in the spin-frozen phase, as expected for a spin glass.

5.4.6 Resonant Inelastic X-Ray Scattering (RIXS)

In Fig. 5.10 (a–b), we show RIXS maps of the Os L_3 resonance measured on the same powder sample at 15 K. In the lower resolution map (b) the most significant feature is a high intensity excitation peaked at energy transfer $\Delta E = 4.2$ eV and $E_i = 10.876$ keV. In the higher resolution map (a) two excitations are seen clearly at energy transfers $\Delta E = 0.2$ eV and 0.7 eV, as well as a weaker, broad feature around $\Delta E = 1.00$–1.25 eV.

i	a_i	E_i (eV)	σ_i (eV)
1	474(20)	-0.003(2)	0.050(2)
2	604(23)	0.206(2)	0.073(3)
3	639(27)	0.665(4)	0.139(6)
4	410(10)	1.11(3)	0.47(2)
5	168(20)	3.23(2)	0.19(3)
6	820(40)	4.10(1)	0.41(2)
7	532(18)	5.08(6)	0.93(4)

Table 5.2: Gaussian parameters obtained from a fit of the sum four Guassians plus a linear background to Fig. 5.10 (c) and three Guassians plus a constant background to Fig. 5.10 (d) where each Gaussian is of the form intensity $= a_i \exp(-(E - E_i)^2/2\sigma_i^2)$.

Within the resolution of these data, all these lower energy excitations resonate at the same incident energy $E_i = 10.8725\,\text{keV}$. There are also some broad, weak excitations at energy transfers around 3.33 eV and above $\sim 5\,\text{eV}$. Cuts through all these features (Fig. 5.10 (c) and (d)) show that no splitting into sub-levels is resolvable in any of them.

As the incident photon energy is tuned to the Os L_3 edge we assume that the observed excitations involve Os $5d$ states. The crystal field at the Os site is close to cubic with only a small perturbing trigonal distortion, so to a first approximation we can identify the $\Delta E = 4.2\,\text{eV}$ feature with single-ion t_{2g} – e_g excitations and the low energy features with intra-t_{2g} excitations. This assumption allows us to estimate the cubic crystal field parameter $10Dq = 4.2\,\text{eV}$. This assignment is supported by the fact that the t_{2g} – e_g and intra-t_{2g} excitations resonate at energies separated by around 4 eV as expected and that this crystal field value is comparable to that found in other osmates, for example $10Dq$ = 4.3 eV in Ba_2YOsO_6 and $10Dq = 4.5\,\text{eV}$ in Ca_3LiOsO_6 [192].

To quantify the energies and widths of these RIXS excitations, we performed phenomenological fits of the spectra in Fig. 5.10, with the data in panels (c) and (d) modelled by a linear background and several Gaussian peaks. The corresponding fit parameters, numbered as indicated in the figures, are given in Table 5.2.

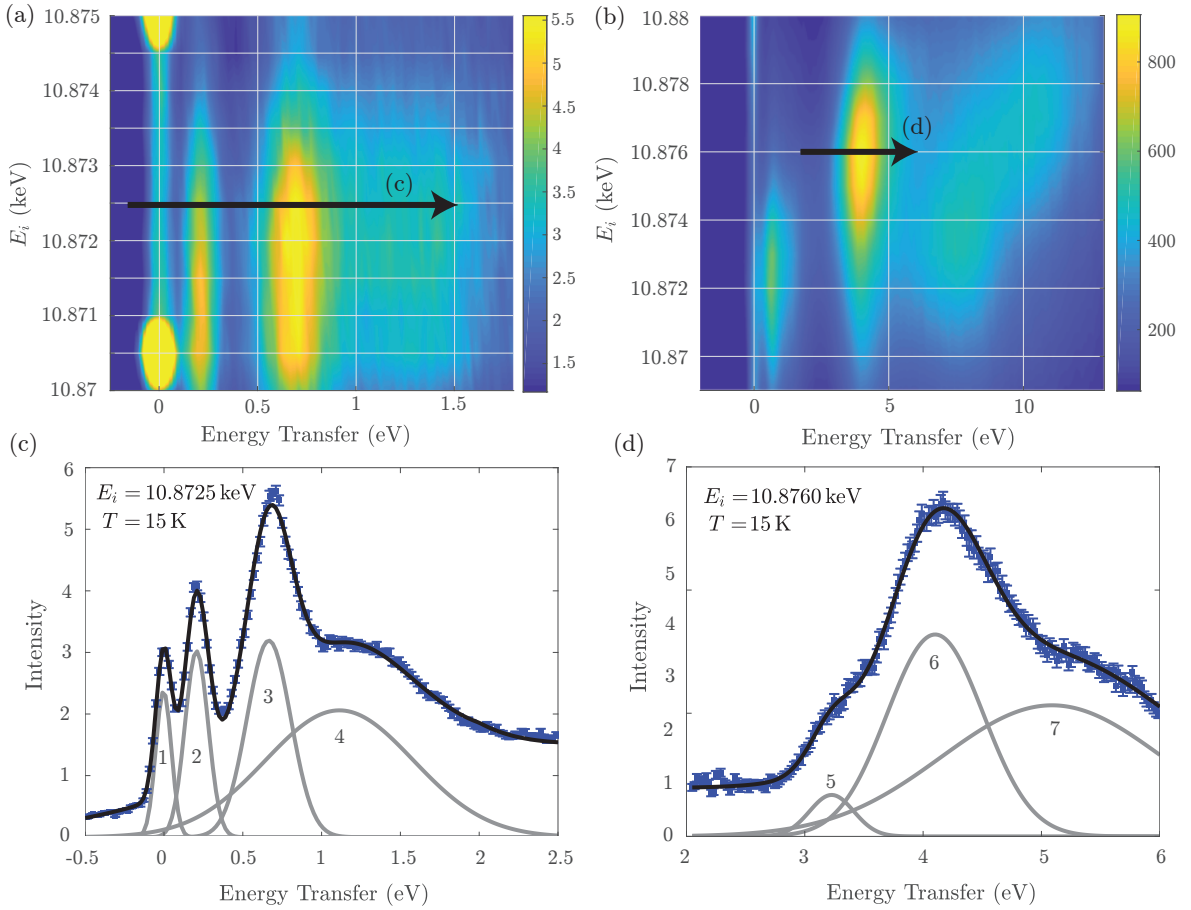

Figure 5.10: RIXS spectra of $Y_2Os_2O_7$ taken at 15 K on the Os L_3 edge. (a) High resolution map focusing on the low energy excitations, (b) low resolution map, (c) a cut through the low energy excitations as marked in (a) and (d) a cut through the higher energy excitation as marked in (b). The black lines are a fit to four Gaussian peaks plus a linear background in (c) and three Gaussians plus a constant background in (d) with parameters shown in Table 5.2. Grey lines show the fitted Gaussian components with numbers corresponding to peak numbers in the table. The very strong peaks at zero energy in the maps are $Y_2Os_2O_7$ Bragg peaks.

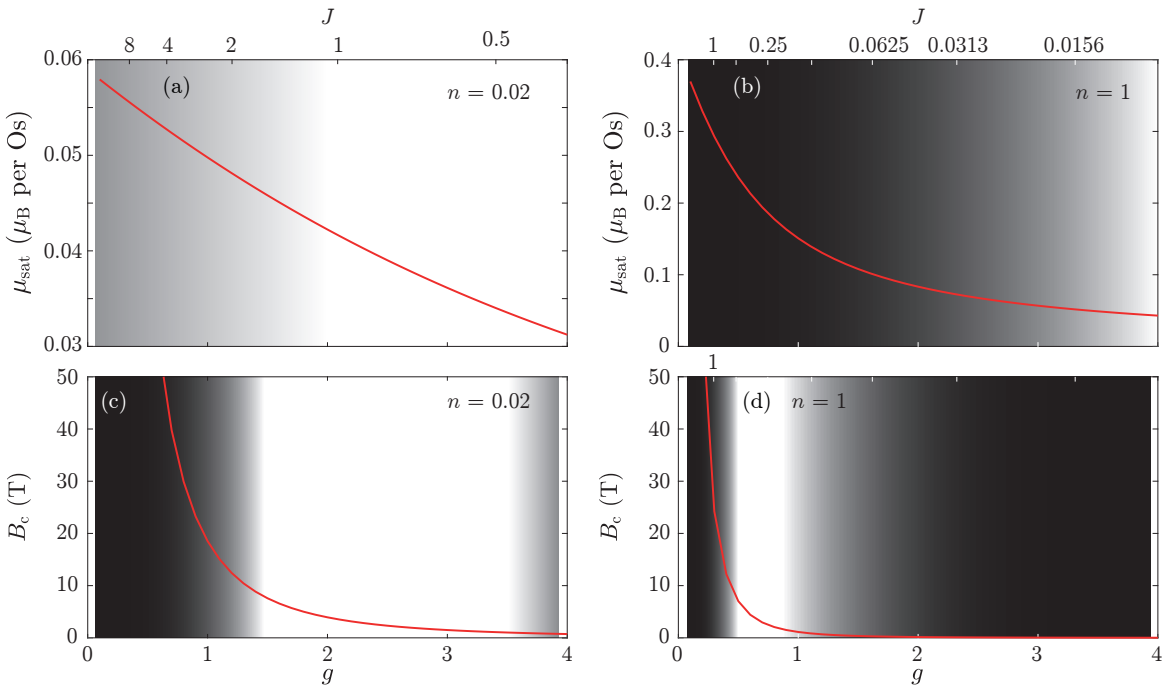

Figure 5.11: (a) and (b) the calculated saturated moment $\mu_{\mathrm{sat}} = ngJ\mu_{\mathrm{B}}$ as a function of J (top axis) and g (bottom axis) for two plausible values of n, based on our Curie-Weiss fitting as described in the main text. (c) and (d) the calculated crossover field $B_{\mathrm{c}} = 5k_{\mathrm{B}}/gJ\mu_{\mathrm{B}}$, as defined in the main text, as a function of g and J. The g and J axes are identical for plots at the same n. The grey shading indicates regimes of g which imply saturation magnetisations (top panels) or saturation fields (bottom panels) that would be in poor agreement with our measurements (see text for a detailed discussion).

5.5 Analysis

5.5.1 High Field Magnetisation

Based on Curie-Weiss fitting, we were able to establish that $\sqrt{n}g\sqrt{J(J+1)} = 0.417(1)$ but were unable to determine the spin concentration, n. Since the saturated moment in high-field magnetisation measurements $\mu_{\mathrm{sat}} = ngJ\mu_{\mathrm{B}}$ has a different dependence on n, we can constrain the possible values of n based on our high-field μ v. H data.

Given the lack of thermal effects at the lowest temperatures shown in Fig. 5.5 (c), we hypothesise that the μ v. H behaviour is instead governed by some average internal energy barrier to spin reorientation, ΔE. Based on the gradual appearance of thermal effects between 5 and 10 K, it is reasonable to assume that such an energy barrier is of

order $k_B T$ at 5 K, i.e. $\Delta E \sim 5k_B$.[1]

Considering the energetics of a single, classical spin in a magnetic field B subject to such an energy barrier, we find that the spin will align with the field (saturate) in the high-field limit for B much greater than some crossover field $B_c = \Delta E/(gJ\mu_B)$. Based on our μ v. H data, it is likely that in this material $1\,\text{T} \lesssim B_c \lesssim 10\,\text{T}$.

Using the constraint that $\sqrt{n}\mu_{\text{eff}}/\mu_B = \sqrt{n}g\sqrt{J(J+1)} = 0.417$ from our susceptibility data, we were able to solve for g as a function of J at two selected values of n (1 and 0.02) chosen to represent the concentrated and dilute cases. The value $n = 0.02$ is chosen as it comparable with the levels of intersite mixing and microscopic disorder seen in similar iridate materials [170]. However, we note that the true value of n may vary by a few % from this in the dilute case.

Given values of g and J, we can calculate the predicted saturation moment $\mu_{\text{sat}} = ngJ\mu_B$ and the crossover field assuming an energy barrier of $5k_B$, $B_c = 5k_B/(gJ\mu_B)$. Plots of these two quantities as a function of g are presented in Fig. 5.11. Applying the previously determined experimental results that $\mu_{\text{sat}} \lesssim 0.04\,\mu_B$ (from Section 5.4.1) and $1\,\text{T} \lesssim B_c \lesssim 10\,\text{T}$, we find that some values of g are very unlikely, represented by the shaded regions on three of the plots. For $n = 0.02$, there is a plausible region for $g \gtrsim 1.5$, while for $n = 1$ we find that all values of g are very unlikely under these constraints.

It is noteworthy that, since the calculated μ_{sat} and B_c are both a factor of 5–10 larger for $n = 1$ than for $n = 0.02$, the above arguments still hold for quite significant changes in n or in the experimental constraints. For example, any value of $n \lesssim 10\,\%$ still yields some plausible values of g, whereas any $n \gtrsim 50\,\%$ leads to all values of g being unlikely based on experiment. We therefore conclude that the fraction of occupied Os sites is very likely to be $\sim$ a few %, with the majority of Os sites adopting in a $J = 0$ state. Higher-field magnetisation data observing moment saturation or data from another technique

[1] The authors of Ref. [173] have extracted an energy barrier to spin reorientation of $\Delta = 204(18)\,\text{K}$ based on a fit of the Arrhenius law $f = f_0 \exp(-\Delta/T_f)$ to the peaks in the real part of the AC susceptibility. This fitting procedure has been shown to yield unphysically large energy barriers when applied to spin glasses, as discussed in Refs. [19, 186, 193, 194], with information about χ'' usually being required to obtain a physically realistic energy barrier.

which is sensitive to the magnitude of the moments independent of their concentration such as electron spin resonance (ESR) would be useful to corroborate this conclusion.

5.5.2 Muon Spin Relaxation (μSR)

Having established that the spins in the sample are very likely to be dilute, we can now perform fitting and simulations of the spin-glass-like relaxation in our μSR spectra.

Phenomenological Fitting

At all temperatures the μSR asymmetry appears to consist of a relaxing component plus a constant baseline component which does not relax even at long decay times, with the relative magnitudes of these two components varying significantly with temperature. In order to quantify this we performed fits to the sum of two exponentials plus the baseline asymmetry, $A(\tau) = A_\mathrm{b} + A_\mathrm{r}((1-a)e^{-\lambda_1\tau} + ae^{-\lambda_2\tau})$ at each temperature where A is the observed muon decay asymmetry, τ is the decay time, λ_1 and λ_2 are the two exponential decay rates, A_r is relaxing asymmetry due to muons experiencing a B field in the sample and A_b is the baseline asymmetry from muons which do not experience a magnetic field. A_b includes muons which stop in the sample holder, cryostat/dilution fridge and any non-magnetic or paramagnetic parts of the sample. Throughout this procedure the initial asymmetry $A_\mathrm{i} = A_\mathrm{r} + A_\mathrm{b}$ was held constant at $A_\mathrm{i} \simeq 30\%$ for the ^{4}He cryostat and at $A_\mathrm{i} \simeq 28\%$ for the dilution fridge. These values were found by fitting the initial asymmetry to the highest temperature dataset available for each sample environment, since A_i should only be a function of the muon beam polarisation and sample environment and is not expected to change with temperature. For datasets above 40 K we found that the spectrum fitted well to a single exponential so at these temperatures a was fixed at 0, while for lower temperatures the full double-exponential form was required. The best possible fit was obtained by fixing $\lambda_2 = 9.66\,\mu\mathrm{s}^{-1}$ to its value in the lowest-temperature dataset in each sample environment for all double-exponential fits. We note that since we have no knowledge of the muon stopping site(s) this fitting function should be treated as purely phenomenological.

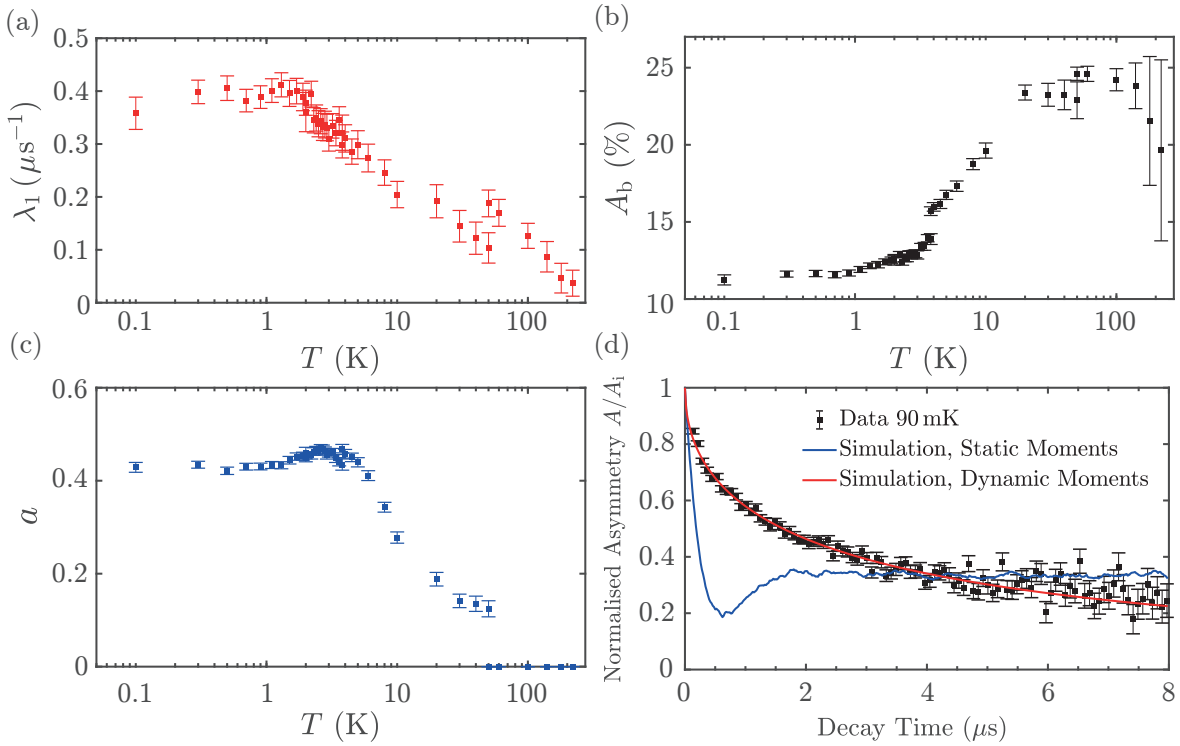

Figure 5.12: (a–c) Temperature dependence of the slower exponential relaxation rate λ_1, fraction of the faster relaxation a and the background asymmetry A_b fitted to our μSR data by the procedure outlined in the main text. (d) Simulated μSR spectrum at 90 mK for static and dynamic moments with moments of magnitude 2.95 μ_B on 2% of Os sites.

Fitted parameters are presented in Fig. 5.12. The relaxation rate λ_1 shows behaviour which is reminiscent of that seen in other spin-glasses [16, 20], with an increase on cooling up to a peak at the spin-glass temperature followed by a plateau below this point. The spin freezing temperature T_f is $\simeq 3\,\mathrm{K}$ based on this measurement, which is slightly lower than that seen in AC susceptibility. This discrepancy may be due to the different fluctuation timescales probed by the different techniques.

The baseline asymmetry shows a clear decrease on cooling before flattening out below T_f, except for a jump at 3.8 K which can be attributed to the change of sample environment from ^{4}He cryostat to dilution fridge at this temperature. This temperature dependence indicates that the volume of sample which is in a paramagnetic state decreases only gradually on cooling with no particularly sharp change at any temperature. A possible explanation for this would be if spins in different parts of the sample are freezing at slightly different temperatures, which is plausible behaviour for a spin glass. The large uncertainties in this parameter at high temperatures are due to limited statistics at very high decay times $\tau > 20\mu$s, since the relaxation is very slow (λ_1 small) at these temperatures.

Overall, it is very likely that the relaxing portion of the μSR spectrum is caused by the same part of the sample as the dilute spins which show hysteretic, spin-glass-like behaviour in magnetisation measurements. Since the muons can be assumed to stop randomly throughout the $Y_2Os_2O_7$ and impurity phases, we can therefore use the magnitude of the relaxing μSR signal relative to the background to examine which of the two phases the spins are located in.

At low temperature, the baseline asymmetry A_b is very similar in value to the relaxing asymmetry A_r (e.g. $A_\mathrm{r} = 13.442$ and $A_\mathrm{b} = 11.414$ at 92 mK). This implies that at least half of the muons are stopping in an environment which shows the relaxing asymmetry. If the relaxing behaviour were due to muons stopping in a small ($< 10\%$ by volume) impurity phase we would expect A_r to be no more than 10% of the total initial asymmetry, $A_\mathrm{r} + A_\mathrm{b}$, under the assumption that muons stopped in the $Y_2Os_2O_7$ phase do not couple

significantly to spin fluctuations in the impurity phase.

If the spins are located in the $Y_2Os_2O_7$ phase, magnetic exchange mediated by ions located between the spins and the muon stopping sites in this phase would likely cause a significant magnetic field at the muon site. For example, in the double perovskite iridates it has been shown [195] that exchange mediated by Y^{3+} and O^{2-} ions is significant even between second- and third- nearest-neighbour Ir sites. Furthermore, simulations presented in Ref. [195] show that for a double perovskite lattice populated with a few % spins on one of the octahedral sites the majority of Ir sites are no further than the third-nearest-neighbour distance from a spin. Assuming that similar results hold in $Y_2Os_2O_7$, muons stopping at most locations within the $Y_2Os_2O_7$ phase will experience a significant magnetic field even if the spin concentration is low. We therefore conclude that the relaxing behaviour is due to dilute moments in the main $Y_2Os_2O_7$ phase, and that the impurity phase shows no noticeable signal other than a constant background in μSR.

Simulations

For the lowest temperature dataset we have performed a simulation similar to that presented in Ref. [196] to try to extract information about the spin dynamics. This simulation involves randomly populating a lattice with magnetic moments μ on n % of the sites then examining the internal field at a muon test site. We applied the constraint $n\mu = 0.06\,\mu_{\text{B}}$ ($n = 2\,\%, \mu = 2.95\,\mu_{\text{B}}$) throughout in order to agree with the conclusions from our magnetisation data.

If the spins are assumed to be completely static, the simulation results in an asymmetry

$$A(\tau) = \int p(\Delta)(\frac{1}{3} + \frac{2}{3}\cos(\gamma_\mu \Delta\tau))\mathrm{d}\Delta \tag{5.4}$$

where Δ/γ_μ is the width of the field distribution at the muon site, $p(\Delta)$ is the probability of finding that field width for a randomly chosen muon site and γ_μ is the gyromagnetic ratio of the muon. The simulated spectrum assuming the most likely values of $n = 2\%$

and $\mu = 2.95\,\mu_{\mathrm{B}}$ is presented in Fig. 5.12 (d), however we find that this model cannot reproduce the data for any values (n, μ).

If the spins are allowed to fluctuate, the model asymmetry becomes

$$A(\tau) = \int p(\Delta) \mathrm{e}^{-2\Delta^2\tau/\nu} \mathrm{d}\Delta \tag{5.5}$$

where ν is the fluctuation rate. The model with fluctuations provides a much better fit to the data. For $\mu \simeq 2.95\,\mu_{\mathrm{B}}$ and $n \simeq 2\%$ the best fit is achieved with $\nu \simeq 21\,\mathrm{MHz}$, as plotted in Fig. 5.12 (d). This fit is, however, reliant on an adjustment of A_{b} from the previously fitted value of 11% to $\simeq 7\%$. If the baseline asymmetry is fixed at 11% we find that the model cannot reproduce the data even in the dynamical case. This indicates either that the data is not well-modelled by this scenario or that even at the lowest temperatures a significant fraction ($\simeq 18\%$) of muons stopping in the sample experience a non-magnetic or paramagnetic environment. Given that we have ruled out impurities on the $> 10\%$ level this latter situation would imply that the $Y_2Os_2O_7$ phase still contains some non-magnetic regions even well below T_{f}.

5.5.3 RIXS Single Ion Calculations

It is reasonable to assume RIXS is sensitive to all Os sites in the sample, the majority of which we have now established to be in a non-magnetic d^4 configuration based on the above analysis of our other datasets. We therefore performed single-ion calculations on the Os $5d^4$ electrons, including inter-electron interactions, spin-orbit interaction and trigonal crystal field terms in the Hamiltonian in order to understand the origin of the excitations seen in RIXS. This procedure is outlined in Refs. [8, 197] and involves writing each contribution to the Hamiltonian as a matrix using the properly antisymmetrised multielectron states of the d^4 configuration as a basis then numerically diagonalising the combined Hamiltonian. The inter-electron interaction is written in terms of Racah parameters [198] A, B and C which can be transformed into intra- and inter-orbital Coulomb interactions U and U' and the effective Hund's coupling J_{H} via

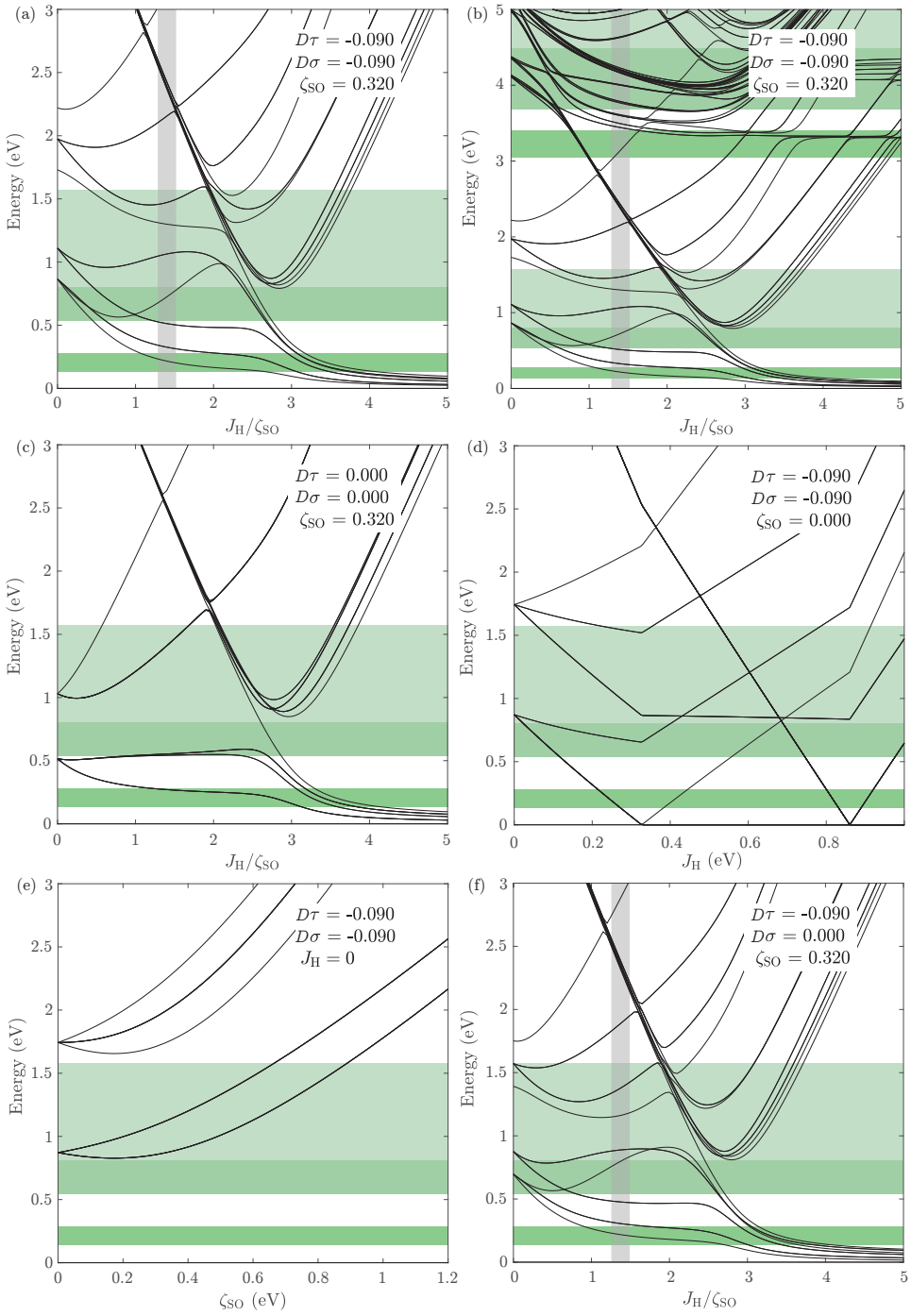

Figure 5.13: The predicted energy levels of Os $5d^4$ electrons from single-ion calculations as outlined in the main text. Green horizontal strips represent the observed energy levels in the present RIXS experiments with the position and width of the strip corresponding to the Gaussian peak position and full width at half maximum from Table 5.2. Vertical grey strips in (a) and (b) indicate a region where the calculated low energy levels appear to best match those seen in experiment as discussed in the main text, while the grey strip in (f) is in the same position as those in (a–b) to aid visual comparison. (a) Calculation with non-zero trigonal distortion, spin-orbit interaction and Hund's coupling. (b) Same as (a) but extended to high energy transfer. (c) Calculation with no trigonal distortion. (d) Calculation with no Hund's coupling. (e) Calculation with no spin-orbit interaction. (f) Calculation with the variable trigonal distortion parameter $D\sigma$ set to zero.

$$\begin{aligned} J_{\mathrm{H}} &= 3B + C \\ U &= A + 4B + 3C \\ U' &= A - 2B + C. \end{aligned} \tag{5.6}$$

Following Ref. [199] the crystal field is parametrised by Dq, $D\sigma$ and $D\tau$, where Dq represents the octahedral crystal field and $D\tau$ and $D\sigma$ small trigonal distortions away from the perfect octahedral case. [2] The spin-orbit coupling strength enters via a single parameter ζ_{SO}.

Some of the above parameters could be found from experiment before performing calculations. We have estimated from the RIXS data that $10Dq = 4.2\,\mathrm{eV}$, and there is a direct relationship between $D\tau$, the sign of $D\sigma$ and the $48f$ oxygen position $x = 0.3352(2)$ [200, 201] which yields $D\tau = -0.090\,\mathrm{eV}$ and tells us that $D\sigma$ must have the same sign (–) as $D\tau$. The Racah parameter A only appears on the diagonal elements of the Hamiltonian and causes only a constant shift of all energy levels. Since spectroscopy reveals only relative, not absolute energies, A is not determined by this measurement.

All other parameters ($B, C, \zeta_{\mathrm{SO}}$ and $|D\sigma|$) are in general free and ideally would be fitted to experimental data. Unfortunately, we do not observe enough excitations in the experiment for this to be possible in this case. Instead, we need to fix some of the parameters to values obtained from other, similar compounds.

We fixed the values of $\zeta_{\mathrm{SO}} = 0.32\,\mathrm{eV}$ and $B = 0$ to the values obtained for Ba_2YOsO_6 in Ref. [192] leaving as free parameters $D\sigma$ and $C = J_{\mathrm{H}}$. Fig. 5.13 (a–b) shows the results of this calculation, in which best agreement with experiment is obtained for $D\sigma = -0.09\,\mathrm{eV}$ and a region around $J_{\mathrm{H}}/\zeta_{\mathrm{SO}} \sim 1.4$. All of the experimental excitations are adequately explained, although notably many of the features are in fact a combination of several closely-spaced levels which are unresolved. There are several states (for example those at 0.3 and 0.5 eV) which fall close to the edges of the experimental peaks, as well

[2] The parameters Dq, $D\sigma$ and $D\tau$ used in this work correspond to the parameters with the same symbols in Ref. [199].

as one set of nearly-degenerate states at around 2.1 eV which is not close to any feature in the experiment. It is possible that these states may have a low spectral weight if a full RIXS calculation were performed, in which case they would be unresolvable above the background, especially in the case of the 0.3 eV and 0.5 eV levels which may easily be swamped by the nearby, stronger excitations or combined with them via intersite hopping terms which are not included in this model.

Changing $D\sigma$ causes small perturbations to the low-lying energy levels and makes the agreement with experiment less good. The $D\sigma = 0$ case is presented in Fig. 5.13 (f) for comparison, showing how agreement is still close but slightly worse, in particular for the two lowest-energy observed peaks.

The above results are consistent with work on other osmates which has seen $J_{\text{H}} \sim \zeta_{\text{SO}}$. We emphasise that due to the number of free parameters and the inherent uncertainty due to the unknown RIXS matrix elements we cannot conclude that the parameter values suggested here are definitely the values in this material, only that based on our current knowledge the present model is capable of explaining the data for plausible values of all parameters.

We also performed calculations by removing in turn the trigonal distortion ($D\tau = D\sigma = 0$, Fig. 5.13 (c)), spin orbit interaction ($\zeta_{\text{SO}} = 0$, Fig. 5.13 (d)) and inter-electron interactions ($B = C = 0$, Fig. 5.13 (e)). In all three cases we could not find any values of the remaining parameters which adequately reproduce the two lowest lying features at 200 and 700 meV in the RIXS spectrum. This allows us to conclude that all three effects are required to model the physics of this material.

The ground state for our likely set of parameters, as well as for *any* set of parameters calculated here as long as $J_{\text{H}}/\zeta_{\text{SO}} \lesssim 3$, is a $J_{\text{eff}} = 0$ non-magnetic singlet. This allows us to rule out any kind of single-ion physics, including the trigonal distortion, as the source of the magnetic moment, consistent with our conclusions from other techniques.

For all reasonable sets of parameters there are low-lying excitations in the 200–400 meV region, which may be either a doublet, triplet or closely-spaced singlet and

doublet. Significantly, we find that for the trigonally distorted case seen here ($D\tau = D\sigma = -0.09\,\text{eV}$) these lowest-lying excitations are a singlet at 200 meV and a degenerate doublet at 300 meV. This is in contrast to the undistorted case where the first excitation is a triplet. Quantitative theories of excitonic magnetism applied to the $A_2\text{YIrO}_6$ (A = Sr, Ba) materials such as Ref. [180] are based on a situation where the first excited state is a low-lying triplet. In the case proposed here for $\text{Y}_2\text{Os}_2\text{O}_7$ the splitting between the singlet and doublet excitations is $\sim 50\%$ of the separation between the singlet excitation and the ground state, representing quite a significant departure from the case used in the theories. The theories may therefore need modification before being directly applied to the pyrochlore osmates.

In light of these calculations, we can now also explain the temperature independent component of the magnetic susceptibility in Fig. 5.4. It was shown in Refs. [172, 180] for Ba_2YIrO_6 that, following standard second-order perturbation theory, in the single-ion case the magnetic susceptibility of a system with a singlet ground state and a low-lying triplet excited state at 350 meV is temperature-independent and on the order of $\chi_0 \sim 1 \times 10^{-5}\,\text{m}^{-3}\,\text{mol}^{-1}$. For $\text{Y}_2\text{Os}_2\text{O}_7$, the first and second excited states are a singlet and a doublet, respectively, with a similar average energy above the ground state as the triplet in Ba_2YIrO_6. The van-Vleck susceptibility for $\text{Y}_2\text{Os}_2\text{O}_7$ is therefore expected to be of similar magnitude to that of Ba_2YIrO_6, consistent with our observed value of $1.126(1) \times 10^{-5}\,\text{m}^{-3}\,\text{mol}^{-1}$.

5.6 Discussion

When all of our experimental results are considered together, a consistent picture emerges with the majority of Os sites in a non-magnetic $J_{\text{eff}} = 0$ state along with a few Os sites exhibiting a non-zero spin. These magnetic defect sites are likely caused by some kind of microscopic disorder, for example related to oxygen deficiency in the sample, site disorder involving partial interchange of Y^{3+} and Os^{4+} ions or partial static charge disproportionation ($2\,\text{Os}^{4+} \rightarrow \text{Os}^{3+} + \text{Os}^{5+}$).

This scenario is very similar to that proposed in the recent preprint Ref. [195] for the $5d^4$ iridate Ba_2YIrO_6, where the authors show via electron spin resonance (ESR) spectroscopy that the observed magnetic moment is caused by a small percentage of Ir^{6+} ($5d^3$) and Ir^{4+} ($5d^5$) magnetic defects, with the majority of Ir sites remaining in the non-magnetic Ir^{5+} ($5d^4$) configuration. A similar scenario in $Y_2Os_2O_7$ would be consistent with all of our data; for example, only 1% of Os sites in the spin-only $5d^3$ configuration ($L = 0$, $J = S = 3/2$) would lead to $\sqrt{n}\mu_{\text{eff}} = 0.3873\,\mu_{\text{B}}$, very close to our measured value of $\sqrt{n}\mu_{\text{eff}} = 0.417\,\mu_{\text{B}}$.

The authors of Ref. [195] also show that medium- and long-range interactions, possibly involving exchange mediated by Y ions, are significant in Ba_2YIrO_6 and that the magnetic defects tend to form extended correlated clusters even at low concentrations. Such long-range interactions and clustering of magnetic defects would provide a natural explanation for the spin-freezing in $Y_2Os_2O_7$, including the observation in our μSR that the proportion of the sample exhibiting non-magnetic behaviour reduces gradually with temperature, and that some regions of the sample appear non-magnetic even below T_{f}.

5.7 Summary

Our AC and DC magnetisation, heat capacity and μSR measurements all show results consistent with low temperature spin-glass behaviour as suggested in Ref. [173]. Having ruled out impurity effects, we have shown that the observed Curie-Weiss-like moment in $Y_2Os_2O_7$ is very likely due to large moments $\sim 3\,\mu_{\text{B}}$ located on a small proportion $\sim 2\%$ of Os sites, perhaps related microscopic disorder in the sample. We have also shown via RIXS measurements in conjunction with single-ion energy level calculations that the majority of Os sites in $Y_2Os_2O_7$ exhibit a $J_{\text{eff}} = 0$ ground state with a low-lying doublet excitation in the single-ion picture. Overall, a scenario similar to that recently proposed by Fuchs *et al.* [195] with a small proportion of magnetic defects in a $5d^3$ or $5d^5$ configuration along with majority non-magnetic $5d^4$ Os sites can explain all of our observations.

Chapter 6

Concluding Remarks

In this thesis I have presented studies on three systems which demonstrate the huge variety of novel and fascinating phenomena found amongst quantum materials, as well as the breadth of experimental techniques which have been developed to probe their behaviour. In each case, I have resolved a key unanswered question about the microscopic physics of the system being examined and provided information which may be useful in discovering and modelling the novel physics in these and other, related quantum materials in future.

In all of the systems I have studied, the effects of interest originate primarily from the *d*-shell electrons on a transition metal ion. In the absence of correlations, these electrons would simply form part-filled bands and the material would be a normal metal. When the electrons are allowed to interact with each other, however, a wide variety of interesting macroscopic states are realised, including the CDW, conventional and unconventional superconductivity and excitonic magnetism which have featured in my studies. This clearly demonstrates the power of the principle of emergence as discussed at the start of this thesis, where new and interesting effects can occur as a result of the cooperative physics of many interacting particles which would not be possible without interactions.

In order to reach the conclusions of each chapter I have employed a large number of different experimental techniques, with a picture of the underlying physics of the materials in question only becoming clear when results from all techniques are considered

together. In addition to showcasing some of the many experimental probes now available in the study of condensed matter systems, my analysis demonstrates the necessity of considering a range of complementary techniques together to fully understand the physics of a given material.

Research in line with these two principles has led to many exciting and important scientific discoveries in the past, and will continue to do so in future. I hope that the work presented here will prove to be a useful part of the basis for such future discoveries.

Bibliography

[1] J. Singleton, *Band Theory and Electronic Properties of Solids* (Oxford University Press, 2001).

[2] J. F. Annett, *Superconductivity, Superfluids and Condensates* (Oxford University Press, 2004).

[3] D. Gatteschi, R. Sessoli, and J. Villain, *Molecular Nanomagnets* (Oxford University Press, 2006).

[4] C.-K. Chiu, J. C. Y. Teo, A. P. Schnyder, and S. Ryu, Rev. Mod. Phys. **88**, 035005 (2016).

[5] S. Blundell, *Magnetism in Condensed Matter* (Oxford University Press, 2001).

[6] S. H. Simon, *The Oxford Solid State Basics* (Oxford University Press, 2013).

[7] S. Sugano, Y. Tanabe, and H. Kamimura, *Multiplets of transition-metal ions in crystals* (New York: Academic Press, 1970).

[8] M. Gerloch, *Magnetism and Ligand Field Analysis* (Cambridge University Press, 1983).

[9] J. Binney and D. Skinner, *The physics of quantum mechanics* (Oxford University Press, 2014).

[10] K. Pajskr, P. Novák, V. Pokorný, J. Kolorenč, R. Arita, and J. Kuneš, Phys. Rev. B **93**, 035129 (2016).

[11] A. Jain, M. Krautloher, J. Porras, G. Ryu, D.-P. Chen, D. Abernathy, J.-T. Park, A. Ivanov, J. Chaloupka, G. Khaliullin, B. Keimer, and B.-J. Kim, Nat. Phys. **13**, 633 (2017).

[12] L. Balents, Nature **464**, 199 (2010).

[13] A. A. Zvyagin, Low Temp. Phys. **39**, 901 (2013).

[14] A. P. Ramirez, Annu. Rev. Mater. Sci. **24**, 453 (1994).

[15] K. Binder and A. P. Young, Rev. Mod. Phys. **58**, 801 (1986).

[16] A. Keren, P. Mendels, I. A. Campbell, and J. Lord, Phys. Rev. Lett. **77**, 1386 (1996).

[17] A. Andreanov, J. T. Chalker, T. E. Saunders, and D. Sherrington, Phys. Rev. B **81**, 014406 (2010).

[18] S. Nagata, P. H. Keesom, and H. R. Harrison, Phys. Rev. B **19**, 1633 (1979).

[19] D. Huser, A. J. van Duyneveldt, G. J. Nieuwenhuys, and J. A. Mydosh, J. Phys. C Solid State Phys. **19**, 3697 (1986).

[20] Y. J. Uemura, T. Yamazaki, D. R. Harshman, M. Senba, and E. J. Ansaldo, Phys. Rev. B **31**, 546 (1985).

[21] P. Monceau, Adv. Phys. **61**, 325 (2012).

[22] S. K. Chan and V. Heine, J. Phys. F Metal Phys. **3**, 795 (1973).

[23] H. K. Onnes, Commun. Phys. Lab. Univ. Leiden **124** (1911).

[24] W. Meissner and R. Ochsenfeld, Naturwissenschaften **21**, 787 (1933).

[25] J. Bardeen, L. Cooper, and J. R. Schrieffer, Phys. Rev. **108**, 1175 (1957).

[26] J. G. Bednorz and K. A. Müller, Z. Phys. B Condens. Mat. **64**, 189 (1986).

[27] D. J. Scalapino, Rev. Mod. Phys. **84**, 1383 (2012).

[28] E. H. da Silva Neto, P. Aynajian, A. Frano, R. Comin, E. Schierle, E. Weschke, A. Gyenis, J. Wen, J. Schneeloch, Z. Xu, S. Ono, G. Gu, M. Le Tacon, and A. Yazdani, Science **343**, 393 (2014).

[29] A. I. Coldea and M. D. Watson, Annu. Rev. Condens. Matter Phys. **9**, 125 (2018).

[30] R. M. Fernandes and A. V. Chubukov, Rep. Prog. Phys. **80**, 014503 (2017).

[31] M. Yi, Y. Zhang, Z.-X. Shen, and D. Lu, Nat. Phys. Quant. Mat. **2**, 57 (2017).

[32] L. Zhao, A. Liang, D. Yuan, Y. Hu, D. Liu, J. Huang, S. He, B. Shen, Y. Xu, X. Liu, L. Yu, G. Liu, H. Zhou, Y. Huang, X. Dong, F. Zhou, K. Liu, Z. Lu, Z. Zhao, C. Chen, Z. Xu, and X. J. Zhou, Nat. Commun. **7**, 10608 (2016).

[33] A. Carrington and F. Manzano, Physica C: Superconductivity **385**, 205 (2003).

[34] Z. Du, X. Yang, D. Altenfeld, Q. Gu, H. Yang, I. Eremin, P. Hirschfeld, I. I. Mazin, H. Lin, X. Zhu, and H.-H. Wen, Nat. Phys. **14**, 134 (2017).

[35] Y. Gao, Y. Yu, T. Zhou, H. Huang, and Q.-H. Wang, Phys. Rev. B **96**, 220507 (2017).

[36] D. C. Johnston, Adv. Phys. **59**, 803 (2010).

[37] G. R. Stewart, Rev. Mod. Phys. **83**, 1589 (2011).

[38] M. D. Lumsden and A. D. Christianson, J. Phys.: Condens. Matter **22**, 203203 (2010).

[39] P. Dai, J. Hu, and E. Dagotto, Nat. Phys. **8**, 709 (2012).

[40] P. J. Hirschfeld, C. R. Physique **17**, 197 (2016).

[41] Y. Gao, Y. Yu, T. Zhou, H. Huang, and Q.-H. Wang, Phys. Rev. B **96**, 014515 (2017).

[42] T. A. Maier and D. J. Scalapino, Phys. Rev. B **78**, 020514 (2008).

[43] M. M. Korshunov and I. Eremin, Phys. Rev. B **78**, 140509 (2008).

[44] I. Mazin and J. Schmalian, Physica C: Superconductivity **469**, 614 (2009).

[45] *MPMS XL Hardware and Software Refernce Manuals*, Quantum Design, San Diego, USA, 2nd ed. (1990).

[46] *Vibrating Sample Magnetometer (VSM) Option Users Manual*, Quantum Design, San Diego, USA, 5th ed. (2011).

[47] *Physical Property Measurement System Heat Capacity Option User's Manual*, Quantum Design, San Diego, USA, 11th ed. (2004).

[48] R. Martin, *Electronic Structure Basic Theory and Practical Methods* (Cambridge University Press, 2004).

[49] A. M. Glazer, *Crystallography: A Very Short Introduction* (Oxford University Press, 2016).

[50] G. L. Squires, *Thermal Neutron Scattering* (Cambridge University Press, 1987).

[51] *Bragg Reflection: Determining the Lattice Constants of Monocrystals, P7.1.2.1*, Leybold Physics Leaflets, LD Didactic AG (1998).

[52] L. J. P. Ament, M. van Veenendaal, T. P. Devereaux, J. P. Hill, and J. van den Brink, Rev. Mod. Phys. **83**, 705 (2011).

[53] L. Paolasini, C. Detlefs, C. Mazzoli, S. Wilkins, P. P. Deen, A. Bombardi, N. Kernavanois, F. de Bergevin, F. Yakhou, J. P. Valade, I. Breslavetz, A. Fondacaro, G. Pepellin, and P. Bernard, J. Synchrotron Radiat. **14**, 301 (2007).

[54] A. C. Hannon, Nucl. Instrum. Methods Phys. Res. A **551**, 88 (2005).

[55] J. R. Stewart, P. P. Deen, K. H. Andersen, H. Schober, J.-F. Barthélémy, J. M. Hillier, A. P. Murani, T. Hayes, and B. Lindenau, J. Appl. Crystallogr. **42**, 69 (2009).

[56] "Thermal neutron three-axis spectrometer IN8," `https://www.ill.eu/users/instruments/instruments-list/in8/description/instrument-layout/` (2018), Accessed: 2018-05-30.

[57] R. Bewley, R. Eccleston, K. McEwen, S. Hayden, M. Dove, S. Bennington, J. Treadgold, and R. Coleman, Physica B: Condens. Mat. **385-386**, 1029 (2006).

[58] R. Ewings, A. Buts, M. Le, J. van Duijn, I. Bustinduy, and T. Perring, Nucl. Instrum. Methods Phys. Res. A **834**, 132 (2016).

[59] "Wikipedia: Angle-resolved photoemission spectroscopy," `https://en.wikipedia.org/wiki/Angle-resolved_photoemission_spectroscopy` (2018), Accessed: 2018-05-30.

[60] D. Lu, I. M. Vishik, M. Yi, Y. Chen, R. G. Moore, and Z.-X. Shen, Annu. Rev. Condens. Matter Phys. **3**, 129 (2012).

[61] R. S. Hayano, Y. J. Uemura, J. Imazato, N. Nishida, T. Yamazaki, and R. Kubo, Phys. Rev. B **20**, 850 (1979).

[62] F. R. Foronda, F. Lang, J. S. Möller, T. Lancaster, A. T. Boothroyd, F. L. Pratt, S. R. Giblin, D. Prabhakaran, and S. J. Blundell, Phys. Rev. Lett. **114**, 017602 (2015).

[63] A. Yaouanc and P. D. De Réotier, *Muon Spin Rotation, Relaxation and Resonance* (Oxford University Press, 2011).

[64] S. J. Blundell, Contemp. Phys. **40**, 175 (1999).

[65] Y. Mizuguchi and Y. Takano, J. Phys. Soc. Jpn. **79**, 102001 (2010).

[66] J. Wen, G. Xu, G. Gu, J. M. Tranquada, and R. J. Birgeneau, Rep. Prog. Phys. **74**, 124503 (2011).

[67] X. Liu, L. Zhao, S. He, J. He, D. Liu, D. Mou, B. Shen, Y. Hu, J. Huang, and X. J. Zhou, J. Phys.: Condens. Matter **27**, 183201 (2015).

[68] M. K. Wu, P. M. Wu, Y. C. Wen, M. J. Wang, P. H. Lin, W. C. Lee, T. K. Chen, and C. C. Chang, J. Phys. D: Appl. Phys **48**, 323001 (2015).

[69] Q. Si, R. Yu, and E. Abrahams, Nat. Rev. Mats. **1**, 16017 (2016).

[70] F.-C. Hsu, J.-Y. Luo, K.-W. Yeh, T.-K. Chen, T.-W. Huang, P. M. Wu, Y.-C. Lee, Y.-L. Huang, Y.-Y. Chu, D.-C. Yan, and M.-K. Wu, Proc. Natl. Acad. Sci. USA **105**, 14262 (2008).

[71] T. M. McQueen, Q. Huang, V. Ksenofontov, C. Felser, Q. Xu, H. Zandbergen, Y. S. Hor, J. Allred, A. J. Williams, D. Qu, J. Checkelsky, N. P. Ong, and R. J. Cava, Phys. Rev. B **79**, 014522 (2009).

[72] S. Medvedev, T. M. McQueen, I. A. Troyan, T. Palasyuk, M. I. Eremets, R. J. Cava, S. Naghavi, F. Casper, V. Ksenofontov, G. Wortmann, and C. Felser, Nat. Mater. **8**, 630 (2009).

[73] J. Guo, S. Jin, G. Wang, S. Wang, K. Zhu, T. Zhou, M. He, and X. Chen, Phys. Rev. B **82**, 180520(R) (2010).

[74] A. F. Wang, J. J. Ying, Y. J. Yan, R. H. Liu, X. G. Luo, Z. Y. Li, X. F. Wang, M. Zhang, G. J. Ye, P. Cheng, Z. J. Xiang, and X. H. Chen, Phys. Rev. B **83**, 060512 (2011).

[75] A. Krzton-Maziopa, Z. Shermadini, E. Pomjakushina, V. Pomjakushin, M. Bendele, A. Amato, R. Khasanov, H. Luetkens, and K. Conder, J. Phys.: Condens. Matter **23**, 052203 (2011).

[76] M.-H. Fang, H.-D. Wang, C.-H. Dong, Z.-J. Li, C.-M. Feng, J. Chen, and H. Q. Yuan, Europhys. Lett. **94**, 27009 (2011).

[77] T. P. Ying, X. L. Chen, G. Wang, S. F. Jin, T. T. Zhou, X. F. Lai, H. Zhang, and W. Y. Wang, Sci. Rep. **2**, 426 (2012).

[78] M. Burrard-Lucas, D. G. Free, S. J. Sedlmaier, J. D. Wright, S. J. Cassidy, Y. Hara, A. J. Corkett, T. Lancaster, P. J. Baker, S. J. Blundell, and S. J. Clarke, Nat. Mater. **12**, 15 (2013).

[79] A. Krzton-Maziopa, E. V. Pomjakushina, V. Y. Pomjakushin, F. von Rohr, A. Schilling, and K. Conder, J. Phys.: Condens. Matter **24**, 382202 (2012).

[80] E. W. Scheidt, V. R. Hathwar, D. Schmitz, A. Dunbar, W. Scherer, F. Mayr, V. Tsurkan, J. Deisenhofer, and A. Loidl, Eur. Phys. J. B **85**, 279 (2012).

[81] Q.-Y. Wang, Z. Li, W.-H. Zhang, Z.-C. Zhang, J.-S. Zhang, W. Li, H. Ding, Y.-B. Ou, P. Deng, K. Chang, J. Wen, C.-L. Song, K. He, J.-F. Jia, S.-H. Ji, Y.-Y. Wang, L.-L. Wang, X. Chen, X.-C. Ma, and Q.-K. Xue, Chin. Phys. Lett. **29**, 37402 (2012).

[82] J.-F. Ge, Z.-L. Liu, C. Liu, C.-L. Gao, D. Qian, Q.-K. Xue, Y. Liu, and J.-F. Jia, Nat. Mater. **14**, 285 (2015).

[83] Y. Texier, J. Deisenhofer, V. Tsurkan, A. Loidl, D. S. Inosov, G. Friemel, and J. Bobroff, Phys. Rev. Lett. **108**, 237002 (2012).

[84] S. C. Speller, T. B. Britton, G. M. Hughes, A. Krzton-Maziopa, E. Pomjakushina, K. Conder, A. T. Boothroyd, and C. R. M. Grovenor, Supercond. Sci. Technol. **25**, 084023 (2012).

[85] X. F. Lu, N. Z. Wang, H. Wu, Y. P. Wu, D. Zhao, X. Z. Zeng, X. G. Luo, T. Wu, W. Bao, G. H. Zhang, F. Q. Huang, Q. Z. Huang, and X. H. Chen, Nat. Mater. **14**, 325 (2015).

[86] U. Pachmayr, F. Nitsche, H. Luetkens, S. Kamusella, F. Brückner, R. Sarkar, H. H. Klauss, and D. Johrendt, Angew. Chem., Int. Ed. **54**, 293 (2015).

[87] X. Dong, H. Zhou, H. Yang, J. Yuan, K. Jin, F. Zhou, D. Yuan, L. Wei, J. Li, X. Wang, G. Zhang, and Z. Zhao, J. Am. Chem. Soc. **137**, 66 (2015).

[88] H. Sun, D. N. Woodruff, S. J. Cassidy, G. M. Allcroft, S. J. Sedlmaier, A. L. Thompson, P. A. Bingham, S. D. Forder, S. Cartenet, N. Mary, S. Ramos, F. R. Foronda, B. H. Williams, X. Li, S. J. Blundell, and S. J. Clarke, Inorg. Chem. **54**, 1958 (2015).

[89] X. H. Niu, R. Peng, H. C. Xu, Y. J. Yan, J. Jiang, D. F. Xu, T. L. Yu, Q. Song, Z. C. Huang, Y. X. Wang, B. P. Xie, X. F. Lu, N. Z. Wang, X. H. Chen, Z. Sun, and D. L. Feng, Phys. Rev. B **92**, 060504 (2015).

[90] Z. Du, X. Yang, H. Lin, D. Fang, G. Du, J. Xing, H. Yang, X. Zhu, and H.-H. Wen, Nat. Commun. **7**, 10565 (2016).

[91] D. Guterding, H. O. Jeschke, P. J. Hirschfeld, and R. Valentí, Phys. Rev. B **91**, 041112 (2015).

[92] F. Wang, F. Yang, M. Gao, Z.-Y. Lu, T. Xiang, and D.-H. Lee, EPL (Europhysics Letters) **93**, 57003 (2011).

[93] T. Saito, S. Onari, and H. Kontani, Phys. Rev. B **83**, 140512 (2011).

[94] N. Hao and J. Hu, Phys. Rev. B **89**, 045144 (2014).

[95] S. Pandey, A. V. Chubukov, and M. Khodas, Phys. Rev. B **88**, 224505 (2013).

[96] T. Ong, P. Coleman, and J. Schmalian, Proc. Natl. Acad. Sci. **113**, 5486 (2016).

[97] E. M. Nica, R. Yu, and Q. Si, Nat. Phys. Quant. Mat. **2**, 24 (2017).

[98] S. P. Thompson, J. E. Parker, J. Potter, T. P. Hill, A. Birt, T. M. Cobb, F. Yuan, and C. C. Tang, Rev. Sci. Instr. **80**, 075107 (2009).

[99] C. V. Topping, F. K. K. Kirschner, S. J. Blundell, P. J. Baker, D. N. Woodruff, F. Schild, H. Sun, and S. J. Clarke, Phys. Rev. B **95**, 134419 (2017).

[100] G. Ehlers, J. E. Greedan, J. R. Stewart, K. C. Rule, P. Fouquet, A. L. Cornelius, C. Adriano, P. G. Pagliuso, Y. Qiu, and J. S. Gardner, Phys. Rev. B **81**, 224405 (2010).

[101] G. Yu, Y. Li, E. M. Motoyama, and M. Greven, Nat. Phys. **5**, 873 (2009).

[102] A. E. Taylor, S. J. Sedlmaier, S. J. Cassidy, E. A. Goremychkin, R. A. Ewings, T. G. Perring, S. J. Clarke, and A. T. Boothroyd, Phys. Rev. B **87**, 220508(R) (2013).

[103] M. C. Rahn, R. A. Ewings, S. J. Sedlmaier, S. J. Clarke, and A. T. Boothroyd, Phys. Rev. B **91**, 180501(R) (2015).

[104] T. A. Maier, S. Graser, P. J. Hirschfeld, and D. J. Scalapino, Phys. Rev. B **83**, 100515 (2011).

[105] X. Zhou, C. K. H. Borg, J. W. Lynn, S. R. Saha, J. Paglione, and E. E. Rodriguez, J. Mater. Chem. C **4**, 3934 (2016).

[106] J. W. Lynn, X. Zhou, C. K. H. Borg, S. R. Saha, J. Paglione, and E. E. Rodriguez, Phys. Rev. B **92**, 060510 (2015).

[107] J. T. Park, G. Friemel, Y. Li, J.-H. Kim, V. Tsurkan, J. Deisenhofer, H.-A. Krug von Nidda, A. Loidl, A. Ivanov, B. Keimer, and D. S. Inosov, Phys. Rev. Lett. **107**, 177005 (2011).

[108] G. Friemel, J. T. Park, T. A. Maier, V. Tsurkan, Y. Li, J. Deisenhofer, H.-A. Krug von Nidda, A. Loidl, A. Ivanov, B. Keimer, and D. S. Inosov, Phys. Rev. B **85**, 140511(R) (2012).

[109] A. E. Taylor, R. A. Ewings, T. G. Perring, J. S. White, P. Babkevich, A. Krzton-Maziopa, E. Pomjakushina, K. Conder, and A. T. Boothroyd, Phys. Rev. B **86**, 094528 (2012).

[110] G. Friemel, W. P. Liu, E. A. Goremychkin, Y. Liu, J. T. Park, O. Sobolev, C. T. Lin, B. Keimer, and D. S. Inosov, EPL (Europhysics Letters) **99**, 67004 (2012).

[111] Q. Wang, J. T. Park, Y. Feng, Y. Shen, Y. Hao, B. Pan, J. W. Lynn, A. Ivanov, S. Chi, M. Matsuda, H. Cao, R. J. Birgeneau, D. V. Efremov, and J. Zhao, Phys. Rev. Lett. **116**, 197004 (2016).

[112] B. Pan, Y. Shen, D. Hu, Y. Feng, J. T. Park, A. D. Christianson, Q. Wang, Y. Hao, H. Wo, Z. Yin, T. A. Maier, and J. Zhao, Nat. Commun. **8**, 123 (2017).

[113] M. Ma, L. Wang, P. Bourges, Y. Sidis, S. Danilkin, and Y. Li, Phys. Rev. B **95**, 100504 (2017).

[114] P. Monthoux, D. Pines, and G. G. Lonzarich, Nature **450**, 1177 (2007).

[115] I. I. Mazin, D. J. Singh, M. D. Johannes, and M. H. Du, Phys. Rev. Lett. **101**, 057003 (2008).

[116] A. Chubukov, Annu. Rev. Condens. Matter Phys. **3**, 57 (2012).

[117] J. A. Wilson, F. J. Di Salvo, and S. Mahajan, Adv. Phys. **24**, 117 (1975).

[118] E. Morosan, H. W. Zandbergen, B. S. Dennis, J. W. G. Bos, Y. Onose, T. Klimczuk, A. P. Ramirez, N. P. Ong, and R. J. Cava, Nat. Phys. **2**, 544 (2006).

[119] T. Yokoya, T. Kiss, A. Chainani, S. Shin, and K. Yamaya, Phys. Rev. B **71**, 140504(R) (2005).

[120] L. F. Mattheiss and D. R. Hamann, Phys. Rev. Lett. **60**, 2681 (1988).

[121] J. M. Tranquada, B. J. Sternlieb, J. D. Axe, Y. Nakamura, and S. Uchida, Nature **375**, 561 (1995).

[122] M. Fujita, H. Goka, K. Yamada, J. M. Tranquada, and L. P. Regnault, Phys. Rev. B **70**, 104517 (2004).

[123] T. P. Croft, C. Lester, M. S. Senn, A. Bombardi, and S. M. Hayden, Phys. Rev. B **89**, 224513 (2014).

[124] T. Wu, H. Mayaffre, S. Krämer, M. Horvatić, C. Berthier, W. N. Hardy, R. Liang, D. A. Bonn, and M.-H. Julien, Nature **477**, 191 (2011).

[125] G. Ghiringhelli, M. Le Tacon, M. Minola, S. Blanco-Canosa, C. Mazzoli, N. B. Brookes, G. M. De Luca, A. Frano, D. G. Hawthorn, F. He, T. Loew, M. Moretti Sala, D. C. Peets, M. Salluzo, E. Schierle, R. Sutarto, G. A. Sawatzky, E. Weschke, B. Keimer, and L. Braicovich, Science **337**, 821 (2012).

[126] J. Chang, E. Blackburn, A. T. Holmes, N. B. Christensen, J. Larsen, J. Mesot, R. Liang, D. A. Bonn, W. N. Hardy, A. Watenphul, M. v. Zimmermann, E. M. Forgan, and S. M. Hayden, Nat. Phys. **8**, 871 (2012).

[127] Y. Wang and A. V. Chubukov, Phys. Rev. B **92**, 125108 (2015).

[128] B. Lorenz, A. M. Guloy, and P. C. W. Chu, Int. J. Mod. Phys. B **28**, 1430011 (2014).

[129] A. Adam and H.-U. Schuster, Z. Anorg. Allg. Chem. **584**, 150 (1990).

[130] E. A. Axtell, III, T. Ozawa, S. M. Kauzlarich, and R. R. P. Singh, J. Solid State Chem. **134**, 423 (1997).

[131] T. C. Ozawa, R. Pantoja, E. A. Axtell, III, S. M. Kauzlarich, J. E. Greedan, M. Bieringer, and J. W. Richardson Jr., J. Solid State Chem. **153**, 275 (2000).

[132] T. C. Ozawa, S. M. Kauzlarich, M. Bieringer, and J. E. Greedan, Chem. Mater. **13**, 1804 (2001).

[133] R. H. Liu, D. Tan, Y. A. Song, Q. J. Li, Y. J. Yan, J. J. Ying, Y. L. Xie, X. F. Wang, and X. H. Chen, Phys. Rev. B **80**, 144516 (2009).

[134] R. H. Liu, Y. A. Song, Q. J. Li, J. J. Ying, Y. J. Yan, Y. He, and X. H. Chen, Chem. Mater. **22**, 1503 (2010).

[135] X. F. Wang, Y. J. Yan, J. J. Ying, Q. J. Li, M. Zhang, N. Xu, and X. H. Chen, J. Phys.: Condens. Matter **22**, 075702 (2010).

[136] T. Yajima, K. Nakano, F. Takeiri, T. Ono, Y. Hosokoshi, Y. Matsushita, J. Hester, Y. Kobayashi, and H. Kageyama, J. Phys. Soc. of Jpn. **81**, 103706 (2012).

[137] P. Doan, M. Gooch, Z. Tang, B. Lorenz, A. Möller, J. Tapp, P. C. W. Chu, and A. M. Guloy, J. Am. Chem. Soc. **134**, 16520 (2012).

[138] T. Yajima, K. Nakano, F. Takeiri, Y. Nozaki, Y. Kobayashi, and H. Kageyama, J. Phys. Soc. Jpn. **82**, 033705 (2013).

[139] H. F. Zhai, W. H. Jiao, Y. L. Sun, J. K. Bao, H. Jiang, X. J. Yang, Z. T. Tang, Q. Tao, X. F. Xu, Y. K. Li, C. Cao, J. H. Dai, Z. A. Xu, and G. H. Cao, Phys. Rev. B **87**, 100502(R) (2013).

[140] K. Nakano, T. Yajima, F. Takeiri, M. A. Green, J. Hester, Y. Kobayashi, and H. Kageyama, J. Phys. Soc. Jpn. **82**, 074707 (2013).

[141] U. Pachmayr and D. Johrendt, Solid State Sci. **28**, 31 (2014).

[142] F. von Rohr, R. Nesper, and A. Schilling, Phys. Rev. B **89**, 094505 (2014).

[143] W. E. Pickett, Phys. Rev. B **58**, 4335 (1998).

[144] F. F. de Biani, P. Alemany, and E. Canadell, Inorg. Chem. **37**, 5807 (1998).

[145] D. J. Singh, New J. Phys. **14**, 123003 (2012).

[146] G. Wang, H. Zhang, L. Zhang, and C. Liu, J. Appl. Phys. **113**, 243904 (2013).

[147] X. W. Yan and Z. Y. Lu, J. Phys.: Condens. Matter **25**, 365501 (2013).

[148] D. V. Suetin and A. L. Ivanovskii, J. Alloys Comp. **564**, 117 (2013).

[149] X. L. Yu, D. Y. Liu, Y. M. Quan, T. Jia, and H. Q. Lin, J. Appl. Phys. **115**, 17A924 (2014).

[150] S. Y. Tan, J. Jiang, Z. R. Ye, X. H. Niu, Y. Song, C. L. Zhang, P. C. Dai, B. P. Xie, X. C. Lai, and D. L. Feng, Nat. Sci. Rep. **5**, 9515 (2015).

[151] Q. Song, Y. J. Yan, Z. R. Ye, M. Q. Ren, D. F. Xu, S. Y. Tan, X. H. Niu, B. P. Xie, T. Zhang, R. Peng, H. C. Xu, J. Jiang, and D. L. Feng, Phys. Rev. B **93**, 024508 (2016).

[152] A. Subedi, Phys. Rev. B **87**, 054506 (2013).

[153] K. Nakano, K. Hongo, and R. Maezono, Sci. Rep. **6**, 29661 (2016).

[154] Y. Nozaki, K. Nakano, T. Yajima, H. Kageyama, B. Frandsen, L. Liu, S. Cheung, T. Goko, Y. J. Uemura, T. S. J. Munsie, T. Medina, G. M. Luke, J. Munevar, D. Nishio-Hamane, and C. M. Brown, Phys. Rev. B **88**, 214506 (2013).

[155] F. von Rohr, A. Schilling, R. Nesper, C. Baines, and M. Bendele, Phys. Rev. B **88**, 140501(R) (2013).

[156] S. Kitagawa, K. Ishida, K. Nakano, T. Yajima, and H. Kageyama, Phys. Rev. B **87**, 060510 (2013).

[157] B. A. Frandsen, E. S. Bozin, H. Hu, Y. Zhu, Y. Nozaki, H. Kageyama, Y. J. Uemura, W.-G. Yin, and S. J. L. Billinge, Nat. Commun. **5**, 5761 (2014).

[158] D. Chen, T.-T. Zhang, Z.-D. Song, H. Li, W.-L. Zhang, T. Qian, J.-L. Luo, Y.-G. Shi, Z. Fang, P. Richard, and H. Ding, Phys. Rev. B **93**, 140501 (2016).

[159] H. Nakaoka, Y. Yamakawa, and H. Kontani, Phys. Rev. B **93**, 245122 (2016).

[160] H. S. Kim and H. Y. Kee, Phys. Rev. B **92**, 235121 (2015).

[161] Y. G. Shi, H. P. Wang, X. Zhang, W. D. Wang, Y. Huang, and N. L. Wang, Phys. Rev. B **88**, 144513 (2013).

[162] H. Nowell, S. A. Barnett, K. E. Christensen, S. J. Teat, and D. R. Allan, J. Synchrotron Radiat. **19**, 435 (2012).

[163] B. J. Campbell, H. T. Stokes, D. E. Tanner, and D. M. Hatch, J. Appl. Cryst. **39**, 607 (2006).

[164] S. C. Miller and W. F. Love, *Tables of Irreducible Representations of Space Groups and Co-Representations of Magnetic Space Groups* (Pruett Press, 1967).

[165] J. Rodriguez-Carvajal, Physica B: Condens. Mat. **192**, 55 (1993).

[166] M. Q. Ren, Y. J. Yan, J. Jiang, S. Y. Tan, J. Miao, C. Chen, Y. Song, C. L. Zhang, P. C. Dai, B. P. Xie, T. Zhang, and D. L. Feng, Philos. Mag. **97**, 527 (2017).

[167] H. Kim, J. H. Shim, K. Kim, and B. I. Min, Phys. Rev. B **96**, 155142 (2017).

[168] K. Nakano, K. Hongo, and R. Maezono, Inorg. Chem. **56**, 13732 (2017).

[169] G. Cao, T.-F. Qi, L. Li, J. Terzic, S.-J. Yuan, L. E. DeLong, G. Murthy, and R. K. Kaul, Phys. Rev. Lett. **112**, 056402 (2014).

[170] T. Dey, A. Maljuk, D. V. Efremov, O. Kataeva, S. Gass, C. G. F. Blum, F. Steckel, D. Gruner, T. Ritschel, A. U. B. Wolter, J. Geck, C. Hess, K. Koepernik, J. van den Brink, S. Wurmehl, and B. Büchner, Phys. Rev. B **93**, 014434 (2016).

[171] F. Hammerath, R. Sarkar, S. Kamusella, C. Baines, H.-H. Klauss, T. Dey, A. Maljuk, S. Gaß, A. U. B. Wolter, H.-J. Grafe, S. Wurmehl, and B. Büchner, Phys. Rev. B **96**, 165108 (2017).

[172] Q. Chen, C. Svoboda, Q. Zheng, B. C. Sales, D. G. Mandrus, H.-D. Zhou, J.-S. Zhou, D. McComb, M. Randeria, N. Trivedi, and J.-Q. Yan, Phys. Rev. B **96**, 144423 (2017).

[173] Z.-Y. Zhao, S. Calder, A. A. Aczel, M. A. McGuire, B. C. Sales, D. G. Mandrus, G. Chen, N. Trivedi, H.-D. Zhou, and J.-Q. Yan, Phys. Rev. B **93**, 134426 (2016).

[174] A. Earnshaw, B. N. Figgis, J. Lewis, and R. D. Peacock, J. Chem. Soc. **0**, 3132 (1961).

[175] E. Ramos, I. Alvarez, R. Sez-Puche, M. Veiga, and C. Pico, J. Alloys Compd. **225**, 212 (1995).

[176] J.-C. Wang, J. Terzic, T.-F. Qi, F. Ye, S.-J. Yuan, S. Aswartham, S. V. Streltsov, D. I. Khomskii, R. K. Kaul, and G. Cao, Phys. Rev. B **90**, 161110 (2014).

[177] L. T. Corredor, G. Aslan-Cansever, M. Sturza, K. Manna, A. Maljuk, S. Gass, T. Dey, A. U. B. Wolter, O. Kataeva, A. Zimmermann, M. Geyer, C. G. F. Blum, S. Wurmehl, and B. Büchner, Phys. Rev. B **95**, 064418 (2017).

[178] B. Ranjbar, E. Reynolds, P. Kayser, B. J. Kennedy, J. R. Hester, and J. A. Kimpton, Inorg. Chem. **54**, 10468 (2015).

[179] J. Terzic, H. Zheng, F. Ye, H.-D. Zhao, P. Schlottmann, L. E. De Long, S.-J. Yuan, and G. Cao, Phys. Rev. B **96**, 064436 (2017).

[180] G. Khaliullin, Phys. Rev. Lett. **111**, 197201 (2013).

[181] O. N. Meetei, W. S. Cole, M. Randeria, and N. Trivedi, Phys. Rev. B **91**, 054412 (2015).

[182] S. Bhowal, S. Baidya, I. Dasgupta, and T. Saha-Dasgupta, Phys. Rev. B **92**, 121113 (2015).

[183] W. Williams, R. Ibberson, P. Day, and J. Enderby, Physica B Condens. Matter **241**, 234 (1997).

[184] V. F. Sears, Neutron News **3**, 26 (1992).

[185] P. J. C. King, R. de Renzi, S. P. Cottrell, A. D. Hillier, and S. F. J. Cox, Phys. Scr. **88**, 068502 (2013).

[186] M. Bałanda, Acta Phys. Pol. A **124**, 964 (2013).

[187] N. P. Raju, E. Gmelin, and R. K. Kremer, Phys. Rev. B **46**, 5405 (1992).

[188] S. R. Dunsiger, R. F. Kiefl, K. H. Chow, B. D. Gaulin, M. J. P. Gingras, J. E. Greedan, A. Keren, K. Kojima, G. M. Luke, W. A. MacFarlane, N. P. Raju, J. E. Sonier, Y. J. Uemura, and W. D. Wu, Phys. Rev. B **54**, 9019 (1996).

[189] L. E. Wenger and P. H. Keesom, Phys. Rev. B **13**, 4053 (1976).

[190] G. Ehlers, J. R. Stewart, A. R. Wildes, P. P. Deen, and K. H. Andersen, Rev. Sci. Instr. **84**, 093901 (2013).

[191] K. Kobayashi, T. Nagao, and M. Ito, Acta Crystallogr. A **67**, 473 (2011).

[192] A. E. Taylor, S. Calder, R. Morrow, H. L. Feng, M. H. Upton, M. D. Lumsden, K. Yamaura, P. M. Woodward, and A. D. Christianson, Phys. Rev. Lett. **118**, 207202 (2017).

[193] D. Hüser, L. E. Wenger, A. J. van Duyneveldt, and J. A. Mydosh, Phys. Rev. B **27**, 3100 (1983).

[194] J. Souletie and J. L. Tholence, Phys. Rev. B **32**, 516 (1985).

[195] S. Fuchs, T. Dey, G. Aslan-Cansever, A. Maljuk, S. Wurmehl, B. Büchner, and V. Kataev, Phys. Rev. Lett. **120**, 237204 (2018).

[196] F. K. K. Kirschner, F. Lang, C. V. Topping, P. J. Baker, F. L. Pratt, S. E. Wright, D. N. Woodruff, S. J. Clarke, and S. J. Blundell, Phys. Rev. B **94**, 134509 (2016).

[197] E. König and S. Kremer, *Ligand Field Diagrams* (Plenum Press, 1977).

[198] A. Georges, L. de' Medici, and J. Mravlje, Annu. Rev. Condens. Matter Phys. **4**, 137 (2013).

[199] J. C. Hempel, J. Chem. Phys. **64**, 4307 (1976).

[200] A. B. P. Lever and B. R. Hollebone, J. Am. Chem. Soc. **94**, 1816 (1972).

[201] J. C. Hempel, R. A. Palmer, and M. C. Yang, J. Chem. Phys. **64**, 4314 (1976).